

Propagation Effects within an Extended Optical Amplifier and Their Impact on the Spatial Distribution of Squeezing:

Towards Quantum Imaging

By

Joseph Kelly

A PhD thesis submitted to
the University of Birmingham

Cold Atoms Research Group
School of Physics and Astronomy
College of Engineering and Physical Sciences
University of Birmingham
June 2023

UNIVERSITY OF
BIRMINGHAM

University of Birmingham Research Archive

e-theses repository

This unpublished thesis/dissertation is copyright of the author and/or third parties. The intellectual property rights of the author or third parties in respect of this work are as defined by The Copyright Designs and Patents Act 1988 or as modified by any successor legislation.

Any use made of information contained in this thesis/dissertation must be in accordance with that legislation and must be properly acknowledged. Further distribution or reproduction in any format is prohibited without the permission of the copyright holder.

© Copyright by JOSEPH KELLY, 2023

All Rights Reserved

ABSTRACT

A continuous laser beam can be viewed as a stream of photons travelling through space. Assuming the generation of each photon is a random and independent process, and they do not interact with each other, they display Poissonian statistics. This leads to random intensity fluctuations on the beam, often referred to as shot noise; this is a limiting factor in many light-based measurements, in particular in imaging.

A technique known as squeezing can be used to reduce this intensity noise at the expense of increasing phase noise, adhering to Heisenberg's uncertainty principle.

Recently, ways of producing squeezed light have been studied extensively. One method, four wave mixing (4WM) in an atomic vapour, has been shown to produce twin beams with a correlated intensity statistics, by acting as a multi-spatial-mode optical parametric amplifier (MSM OPA). Therefore, the intensity difference between the coupled modes is squeezed. Squeezing occurs in multiple spatial modes within the beams, so even localised regions of them are correlated in intensity.

Previously, the focus has been on determining the minimum size of these correlated regions, the coherence area. However, there have been significant challenges in deducing this, which is believed to be due to propagation effects between the coupled modes as they travel through the extended optical parametric amplifier. This leads to the correlated regions not being in an expected place in each beam. As such, the focus of this thesis largely concerns the identifying and untangling this phenomena. Further, a new scheme,

SAI, is proposed that aims to compensate for these propagation effects in a fully optical way.

DEDICATION

To my parents.

ACKNOWLEDGEMENTS

Many people contributed in many ways throughout my PhD, both academically and socially. Regardless, I could not have done this without you all. So, I would like to thank the following.

Vincent Boyer, for his incredibly diverse and in-depth knowledge on almost any topic, as well as his guidance and help throughout this PhD and the writing of my thesis. Ellie Fradgley, for teaching me the ropes of the experiment and all her help through the years. Joe Baker, for interesting discussions and hosting me a few times towards the end of my PhD. Joe Nicholson, from Kingswinford (not Birmingham), for constructive discourse on physics. Tabatha Olney, for helping with a data taking run or two. Stew Pirrie, for engaging discussions regarding chemistry. Tom $|\downarrow\rangle$ and Tom $|\uparrow\rangle$, for loaning me various equipment. Caleb Arthurs, for insightful discussion on electronics and organising a fantastic group holiday. James Pallister, for proofreading and his help solving a coupled recurrence relation problem. Hannah Vincent, for insightful discussions on statistics.

Contents

Acknowledgements **iv**

Page

Introduction 1

I Generating Squeezed Light with 4WM **5**

1 Theory **7**

1.1 The Quantum Theory of Light 7

1.1.1 The Electromagnetic Field as a Simple Harmonic Oscillator 7

1.1.2 Uncertainty and the Electric Field 11

1.1.3 The Optical Amplifier 15

1.1.4 Two-Mode Squeezing 23

1.2 Non-Linear Optics 25

1.2.1 The Polarisation of a Medium 26

1.2.2 Four Wave Mixing in Rubidium 30

1.2.3 The Phase Matching Condition 31

1.2.4 Polarisation 33

1.3 A Model of Squeezing in this System 36

1.3.1 A semi-classical model of 4WM 37

1.3.2 Relating this to the experimental system 38

1.3.3 Optimisation for Squeezing 40

1.4 Multi Mode Squeezing 44
1.4.1 Multi Spatial Mode Squeezing 44
1.4.2 The Coherence Area 46
1.4.3 Squeezing Bandwidth 47
1.5 Potential Measurements That Can Be Made With A Multi-spatial-mode Intensity Difference Squeezed Light Source 50

2 Practical Realisation and Measurement of a Two-mode Squeezed state 53
2.1 Experimental Apparatus 53
2.2 Imaging the Beams 60
2.3 Measuring Squeezing: Instrumentation 61
2.3.1 The Balanced Photodetector 61
2.3.2 The PIXIS-1024BR eXcelon Camera 61

II Camera Imaging 65

3 Localised Squeezing 67
3.1 Set Up 67
3.1.1 Simple Subtraction 69
3.1.2 Fourier Analysis 72
3.1.3 Top-hat Subtraction 74
3.2 Top Hat Searching 76
3.2.1 Results and Discussion 77

4 The Noise Eater 83
4.1 General Principles 84
4.2 AOM considerations 87
4.3 A High Power, Low Noise, and High Bandwidth Photodiode Front End . . 89

4.3.1 Photodiode Theory 90
4.3.2 Front End Design 92
4.4 The AOM, Amplifier, Mixer, and RF Chain 99
4.5 PID Lock Box 100
4.6 Final System Testing 101
4.7 Conclusion 104

III Propagation Effects in an Extended Optical Amplifier 105

5 Lateral Displacement of Bright Probe and Conjugate Beams 107

5.1 A Potential Mechanism of Action 108
5.2 A More Refined Model 112
5.3 Beam Scan Investigation 116
5.3.1 Method 117
5.3.2 Results and Discussion 119
5.4 Elliptical Beam Investigation 121
5.5 Experimental Preparations 122
5.5.1 Producing an Elliptical Seed and Taking Real-Time Seed Power Measurements. 122
5.5.2 Achieving 4WM and Measuring the Angle of Incidence Between the Pump and Probe Beams 123
5.5.3 The $2F - 2F'$ Imaging System 124
5.5.4 Measuring Pump Beam Stability 125
5.5.5 Calculating an Accurate Gain for Vertical Slices of the probe and conjugate Beams 126
5.5.6 Determining the Increments of 1-Photon Detuning Used 127
5.5.7 Method 127

5.6 Results and Discussion . . . 129
5.6.1 1 Photon Detuning Sweep . . . 129
5.6.2 Temperature Sweep . . . 137
5.6.3 Pump Power Sweep . . . 139
5.6.4 2 Photon Detuning Sweep . . . 141
5.7 Conclusion . . . 143

6 Propagation Effects on the Spatial Distribution of the Squeezing 145
6.1 Measuring the Squeezing . . . 146
6.2 Detector Calibration . . . 147
6.3 Searching for squeezed regions . . . 149
6.4 Seed Beam Shaping . . . 151
6.5 Imaging Setup . . . 152
6.6 Motorised Translation Stage . . . 154
6.7 A Demonstration of Multi-Spatial Mode Squeezing . . . 155
6.8 Demonstration of Displaced Squeezing . . . 156
6.8.1 One Photon Detuning Sweep . . . 157
6.8.2 Two-Photon Detuning and Power Sweeps . . . 160
6.9 Double sweep . . . 162

7 A Scheme for All Optical Correction of the Propagation Effects 165
7.0.1 Split Amplification with Intermediary backpropagation . . . 165

8 Closing Remarks 171

A Further Details 175
A.1 Derivations and calculations . . . 175
A.1.1 Magnetic Field Derivation . . . 175

A.2 Technical Details 176
A.2.1 Motorised Translation Stage System Design 176

List of Figures

1.1 A) A coherent state, expressed in terms of the X_1 and X_2 quadratures [21]. In reality, the uncertainty of the state is given by a Gaussian probability density function (PDF) centred on the tip of the phasor, but for clarity this distribution is represented by a red circle with a radius equal to 1σ of the PDF. B) A squeezed state, where the uncertainty on X_1 (seen by the projection of the PDF onto the horizontal axis) is reduced at the expense of increasing the uncertainty on X_2 (seen by the projection of the PDF onto the vertical axis). B) A squeezed state, where the uncertainty on X_2 (seen by the projection of the PDF onto the vertical axis) is reduced at the expense of increasing the uncertainty on X_1 (seen by the projection of the PDF onto the horizontal axis). 12

1.2 Three electric field phasor diagrams where ϕ is chosen to be 0, hence $A = X_1$. A) A coherent state. B) An intensity squeezed state. C) a phase squeezed state. 13

1.3 A representation of a two mode optical amplifier acting on two fields with the creation operators $\hat{a}$ and $\hat{b}$ respectively. 17

1.4 Two electric field phasor diagrams depicting uncertainty on the single mode $X_1^{a,b}$ and $X_2^{a,b}$ quadratures of modes a and b. Since these modes are super-Poissonian their Gaussian Wigner functions have a width larger than a minimum uncertainty coherent state (C) [33]. 25

1.5 Left: A diagram of the geometry of the 4WM within the Rb cell. The double ended arrows next to each beam refer to the orthogonal polarisations of those beams as veiwed on the x-y plane tangental to the propagation direction of the beam, z. Right: The double lambda transition on the D1 line of 85Rb. The two detunings labelled Δ_1 and δ are called the one-photon detuning and two-photon detuning respectively. 30

1.6 A geometric representation of the phase matching condition. This is shown for two cases; in the vacuum (left) and in a resonant media (right). The wave-vectors of the: probe, conjugate and pump beams are represented by: $K_{Pr} = n_{Pr}k_{Pr}$, $K_C = n_C k_C$ and $K_P = n_P k_P$ respectively. [43] 32

1.7 A simplified diagram of he 4WM process. Red arrows represent pump transitions, while black and white lines symbolize probe and conjugate transitions. It's important to note that the position probe and conjugate transitions can be effectively interchanged. 35

1.8 The Direct and Cross susceptibilities for the lower 4WM resonance, over the two-photon detuning. In this case, the one-photon detuning is normalised to the line width of the excited state ($\gamma = 2\pi \times 6MHz$) and was 80 and the pump intensity was $12MWm^{-2}$. 41

1.9 The Direct and Cross susceptibilities for the lower 4WM resonance, against the one-photon detuning. In this case, the two-photon detuning is normalised to the line width of the excited state ($\gamma = 2\pi \times 6MHz$) and was 1.39 and the pump intensity was $12MWm^{-2}$. 42

1.10 The Direct and Cross susceptibilities for the lower 4WM resonance, over various pump intensities. In this case, the one-photon detuning is normalised to the line width of the excited state and was 80, and the two-photon detuning is normalised to the line width of the excited state and is 1.39. 43

1.11 A diagram of the geometry of the localised squeezing in the near field plane (NF) and the far field plane (FF). x and y are the transverse spatial positions in the NF, and q_x and q_y are transverse positions in the FF. z is the propagation distance of the beams. In the NF ($z = 0$), photons are created pairwise in distinct locations, so small regions of the beams will be correlated. In the FF ($z = \infty$) the correlated modes have a z-axial symmetry imposed by the phase-matching condition. 45

1.12 A representation of the cross coupling process, the light regions denote two spatial modes, M_1 and M_2, whereas the dark region represents where they overlap. In the medium, this results in cross coupling between the modes (overlapping outside the medium is irrelevant, as it does not produce any interaction). The Rayleigh length is shown just for M_1. 46

1.13 A diagram of a seeded 4WM process in the frequency domain. The widths of the emissions about ω_{Pr} and ω_C are approximately $20MHz$ (shown in diagonal hatch). This is the squeezing bandwidth, which is determined by the range of frequencies that the 4WM process is efficient over. 48

1.14 A representation of the classical (C), quantum (Q), and total (T) noise of the squeezed state in frequency space. The quantum noise begins at its minimum below the quantum noise limit (QNL). However, the total noise is kept above the QNL at low frequencies by the classical noise, which has a $\frac{1}{\omega}$ dependence. 50

2.1 the predicted noise figure for 4WM with an intrinsic gain $G = 3$ and conjugate transmission T_C equal to one - Adapted from Jasperse et. al. [66]. 55

2.2 A Diagram of pre-cell beam preparation. 56

2.3 A diagram of the RF chain from the pump signal generator to the pump AOM transducer and the RF chain from the probe signal generator to the probe AOM transducer. The abbreviations AT, LIM, and AMP stand for attenuation, limiter, and amplifier respectively. 56

2.4 A diagram showing the difference between the unsaturated case, A, and the saturated case, B, for a generic amplifier. In the unsaturated case, the variance on the signal leads to significant variance on the output due to the large gradient in the transmission function, whereas, in the saturated case it does not, due to the shallow gradient in the transmission function. 58

2.5 Depiction of the vacuum assembly that holds and regulates the temperature of the Rb cell, typically used ($\sim 110°C$). 59

2.6 A diagram of the typical optical setup after the gain medium. L1, L2, H, V1, and V2 are imaging lenses used to focus the beams onto a detector for measurment. 60

2.7 A circuit diagram of the BPD internals, the photo currents generated by the two photodiodes subtract at the junction between them and are converted to a voltage, V_{diff}, by a transimpedance amplifier. Resistors on either side of the photodiodes convert the small current they produce into a small voltage drop across them. This is amplified by two instrumentation amplifiers, I, to produce V_1 and V_2. 62

3.1 A diagrammatic representation of 4F imaging. 68

3.2 A single frame of data captured on the camera CCD. 69

3.3 An image of the normalised variances on the pixels produced by the conjugate beam, averaged over 42 separate frames. 71

3.4 An image of the normalised variances on the subtracted beams ($Pr - C$). Both beams are centred at the centre of the image. 72

3.5 1D Noise Profile in frequency space. The DC noise has been removed for scaling. 73

3.6 1D Noise Profile against spatial wavelength. The DC noise has been removed for scaling. 73

3.7 A progressive series of normalised variance images on the subtracted data for different kernel sizes generated from our real data. A: The image generated for a kernel size of 16×2, with an average normalised variance of 0.37. B: The image generated for a kernel size of 32×4, with an average normalised variance of 1.15. C: The image generated for a kernel size of 48×6, with an average normalised variance of 1.19. D: The image generated for a kernel size of 64×8, with an average normalised variance of 1.27 75

3.8 The squeezing map of frame 1, with a kernel size of 48x6 at y = 18. 78

3.9 The squeezing map of frame 1, with a kernel size of 16x2 at y = 18. 78

3.10 The Variance map of the simulated data. 81

4.1 A diagram of the noise eater set up. In this case, the mixer is used as a variable current controlled attenuator for the RF driving the AOM. 85

4.2 A diagram of the input and output modes of a typical AOM, in the far field of the AOM (momentum picture). A) A perfectly Gaussian input beam. B) The $0th$ order output. C) The $1st$ order output. 88

4.3 The structure of a PIN photodiode. 91

4.4 A circuit diagram of the photodiode front end circuit. 92

4.5 A comparison of the saturation powers of each of the photodetectors, the error on both the voltage and incident power is roughly shown by the size of the plotted points. 93

4.6 A circuit diagram of the TIA based photodiode front end. 94

4.7 A circuit diagram of the capacitance multiplier filter. 96

4.8 A recording of the ripple on the positive and negative branches of the power supply both before (black) and after (coloured) the capacitance multiplier filter. 96

4.9 PSDs of both detectors, at $0mW$ and $7.25mW$ incident intensity. 98

4.10 A plot of the input current into the mixer vs. the DC voltage on the feedback photodiode. The error on both the voltage and the current is roughly shown by the size of the plotted points. 100

4.11 A simplified diagram of the lock box circuitry. 100

4.12 A simplified diagram of the optical set-up for measuring the level of noise reduction by the Noise Eater. The noise eater photodetector (NE p.d.) was the custom one previously discussed and the unlabelled photodetectors were Thorlabs PA100A-EC type. 102

4.13 PSDs of the output before and after the noise eater as well as the difference between them. 103

5.1 An idealised representation of the 4WM system within the cell. 108

5.2 A nodal representation of the 4WM system within the cell. 109

5.3 The result of a simulation produced using a seed value of $(0, 1)$, assuming negligible conjugate loss. 100 longitudinal steps were taken, where $g^{Pr} = g^C = 0.06$, $l^{Pr} = 0.95$, and $l^C = 1$. The final total probe gain was 15 and the final total conjugate gain was 22. The coloured vertical lines represent the weighted mean position of the beams. The asymmetry of the final probe and conjugate profiles comes from the fact that the probe experiences loss while the conjugate does not. 110

5.4 The resulting displacements seen in a series of simulations produced using a seed value of $(0, 1)$ in a lossless scenario. 100 longitudinal steps were taken, where $g^{Pr} = g^C$ was swept between 0 and 0.04 in equal increments, and $l^{Pr} = l^C = 1$. The coloured vertical line represents a gain of 1. 111

5.5 The resulting displacements seen in a series of simulations produced using a seed value of $(0, 1)$, in a lossy scenario. 100 longitudinal steps were taken, where $g^{Pr} = g^C$ was swept between 0 and 0.0525, and $l^{Pr} = 0.975$ and $l^C = 1$. The coloured vertical line represents a gain of 1. 111

5.6 The resulting displacements seen in a series of simulations produced using a seed value of $(0, 1)$. 100 longitudinal steps were taken, where $g^{Pr} = g^C = 0.011$ and $l^C = 1$, and l^{Pr} was swept between 0.94 and 1 in equal increments. The coloured vertical line represents a gain of 1. 112

5.7 The resulting displacements seen in a series of simulations produced using a seed value of $(0, 1)$. 100 longitudinal steps were taken, where $g^{Pr} = g^C = 0.022$ and $l^C = 1$, and l^{Pr} was swept between 0.94 and 1 in equal increments. The coloured vertical line represents a gain of 1. 112

5.8 The resulting probe intensity profiles seen in a series of simulations produced using a $\chi_{PrPr} = 0.15 + 0.0i$. 100 steps in χk were taken, over a range of 0 – 0.17 rad mm^{-1}. Darker plots represent an increasing value of χ and gain. 114

5.9 The resulting conjugate intensity probe profiles seen in a series of simulations produced using a $\chi_{PrPr} = 0.15 + 0.0i$. 100 steps in χk were taken, over a range of 0 – 0.17 rad mm^{-1}. Darker plots represent an increasing value of χ and gain. 114

5.10 The resulting displacements seen in a series of simulations produced where $\chi_{PrPr} = 0.15 + 0i$, so there was no loss on the probe. The gain was changed by altering χk over a range of 0 – 0.17 rad mm^{-1}, over 100 equal increments. The red line represents a gain of 1. 115

5.11 The resulting displacements seen in a series of simulations produced where $\chi_{PrPr} = 0.15 + 0.05i$, such that there was loss on the probe. The gain was changed by altering χk over a range of 0 – 0.20 rad mm^{-1}, over 100 equal increments. The red line represents a gain of 1. 115

5.12 The 4F imaging system used in the beam scan experiment. 117

5.13 The probe Gain vs. Seed position along the cell. 120

5.14 The conjugate Gain vs. Seed position along the cell. 120

5.15 The probe Seed intensity vs. Seed position along the cell. 120

5.16 Horizontal cross-section of the pump beam intensity. 120

5.17 Peak positions of the probe and conjugate vs. Seed position along the cell. 120

5.18 Relative displacement between peak positions of the probe and conjugate vs. Seed position along the cell. 120

5.19 The final setup of the post fibre Seed prep for the elliptical beam experiment. The focal length of the spherical lenses used are; $L1 = 100mm$, $L2 = 50mm$, $L3 = 50mm$, $L4 = 200mm$, and $L5 = 500mm$. The cylindrical lenses both have a focal length of $C1 = C2 = 25mm$ 123

5.20 The $2F - 2F'$ imaging system used in the experiment. 124

5.21 A representation of the beam profiles at various points in the experiment. A) Initially, the oppositely polarised pump and probe seed beams combine at the PBS, shown in figure 5.20. B) After, they are focused to the centre of the cell where 4WM occurs, producing gain on the probe and generating the conjugate beam. Hence, all three beams are present in the object plane. C) The beams are then transported to the Fourier plane by lens $L1$. Here, most of the pump has already been removed by the G-TP, but the rest passes between the split mirrors. The long and short axes of the probe and conjugate beams are switched due to diffraction effects. D) Finally, the probe and conjugate are projected onto the imaging plane by $L2$ with a magnification factor of 3x. 125

5.22 A diagram showing the process of cutting the beams into vertical sections, averaging each segment horizontally, and then fitting a Gaussian to each segment to find its midpoint. The beam depicted with a solid line is the probe at the exit surface of the cell, and the beam shown in the dashed line is the undisturbed probe seed beam. The vertical slices are divided with straight dashed lines and the midpoint vertical position of each beam is shown with a solid line running through their centres. The displacement in this diagram is greatly exaggerated for illustrative purposes; in reality, the displacement of the beam is tiny (~ 40 μm) as compared to its width (~ 250 μm). 129

5.23 The full array of subtracted images obtained in the 1-photon detuning sweep, each increment represents a $\sim 67MHz$ shift in 1-photon detuning. The scale represents the intensity of the beam at each pixel in arbitrary units and the x and y axis are spacial with each pixel in the images representing a pixel on the camera. 130

5.24 The profiles of the probe beam obtained in the 1-photon detuning sweep, each increment represents a $\sim 67MHz$ shift in 1-photon detuning. The 1-photon detuning was swept from a blue-detuned state towards the 4WM resonance. The line colour darkens the closer the slice is to the centre of the beam; hence, each plot represents many regions of differing gain and loss. 131

5.25 The profiles of the conjugate beam obtained in the 1-photon detuning sweep, each increment represents a $\sim 67MHz$ shift in 1-photon detuning. The 1-photon detuning was swept from a blue-detuned state towards the 4WM resonance. The line colour darkens the closer the slice is to the centre of the beam; hence, each plot represents many regions of differing gain and loss. 131

5.26 The peak position and gain profiles of the beams over the 1 photon detuning sweep. Beam position on the y axis references the position of each slice laterally across the beams. The peak position on the z axis referrers to the mean position of the vertical Gaussians fitted to each slice. The actual positions of each of the peaks are arbitrary, it is the relative positions that matter here. As such, each of the position graphs have been displaced to lie around 0. Positions closer to 0 represent the beams closer together at the cell. Positions shown here are magnification corrected, so represent the magnitude of the actual displacements at the cell. 133

5.27 The distance between probe and conjugate beam slices vs. gain for each 1 photon detuning increment. The origin in the graph is arbitrary, since the absolute distance between the beams is not known, by the nature of the experiment. 135

5.28 A parametric plot of the distance between the average positions of the 10 probe and conjugate beam slices nearest the centre of the pump profile vs. gain for each 1 photon detuning increment. The origin in the graph is arbitrary, since the absolute distance between the beams is not known, by the nature of the experiment. 135

5.29 Total absorption of the seed over the 1Pd range. 136

5.30 Spatial absorption of the seed over the 1pd range. The absorption valley is of a similar width to that of the pump beam diameter ($\sim 2000\mu m$). . . 136

5.31 The differential displacement vs. gain for each cell Temperature. 138

5.32 Total absorption of the seed over the temperature range. There is no change over the temperature range, within error. 139

5.33 Absorption of the seed over the temperature range. The absorption valley is of a similar width to that of the pump beam diameter ($\sim 2000\mu m$). The absorption is nearly very similar for each temperature, with the integrated absorption being the same for each case. 139

5.34 The differential displacement vs. gain for each overall pump power. 140

5.35 Total absorption of the seed over the power range. 141

5.36 A plot of the total absorption of the Seed beam against total pump power. The absorption valley is of a similar width to that of the pump beam diameter ($\sim 2000\mu m$). 141

5.37 The full array of subtracted images obtained in the 2 photon detuning sweep. The x and y axis are spacial, with each pixel in the images representing a pixel on the camera. 142

5.38 The differential displacement Vs. gain for each 2-photon detuning increment. 142

6.1 A circuit diagram of the BPD internals, the photo currents generated by the two photodiodes subtract at the junction between them and are converted to a voltage, V_{diff}, by a transimpedance amplifier. Resistors on either side of the photodiodes convert the small current they produce into a small voltage drop across them. This is amplified by two instrumentation amplifiers, I, to produce V_1 and V_2. 147

6.2 Diagram of the near field images of the probe and conjugate beams. The diagonal shaded regions represent two correlated areas between the probe and conjugate beams. The area is curved in the probe beam due to the influence of the varying pump intensity. The lines that extend beyond the circle represent the boundaries of two slits s_1 and s_2, that are used to select small slices of each beam for comparison. 150

6.3 Diagram of the lens arrangement that produced a seed beam of the desired shape and size focused at the centre of the Rubidium vapour cell. The focal powers of the spherical lenses were $L1 = 100mm$, $L2 = 50mm$, $L3 = 50mm$, and $L4 = 100mm$. The focal powers of the cylindrical lenses were $C1 = 50mm$, $C2 = 50mm$, and $C3 = 100mm$. 151

6.4 Diagram of the imaging setup that projects the probe and conjugate beams to the BPD 152

6.5 The squeezing recorded during a complete transit of the conjugate slit whilst the probe slit was held steady at parameters optimised for full beam squeezing. A Gaussian fit is also provided. 154

6.6 The squeezing recorded during a series of complete transits of the conjugate slit whilst the probe slit was held steady and the one photon detuning (1pd) was increased in each transit. A Gaussian fit is also provided for each of these transits too. 158

6.7 The relative mean position of each of the fits displayed in figure 6.6. Alongside is a plot of a rubidium transmission spectra, allowing an accurate frequency estimation for the 1pd at each point. The errors on these points were produced by first holding all parameters at optimal squeezing, then transiting the conjugate 10 times. The standard deviation of the mean of fits made to these transits was then used as an estimate of the error. The dashed red line represents the position at which the maximum probe gain was realised. 159

6.8 A parametric plot of the mean displacement of each peak against the gain on the probe portion. 160

6.9 The mean position of each of the fits made as 2pd was swept. 161

6.10 The mean position of each of the fits made as pump power was swept. . . 161

6.11 A plot of the mean displacement of each peak against the gain on the probe portion (2pd sweep). 161

6.12 A plot of the mean displacement of each peak against the gain on the probe portion (power sweep). 161

6.13 The results of the probe transit sweep, The probe gain is shown in red while the differential displacement shown in dashed black. A linear fit of two points at the similar gain is shown in solid black. 163

7.1 A general scheme of SAI, where an initial optical amplifier C_1 generates two beams, and a displacement effect between them. This is followed by a 4F system that inverts the k vectors of each of the beams before they enter into another optical amplifier C_2. Any displacement effect in the second amplifier is in the opposite direction to that seen in the first, so acts to mitigate the effect of the initial displacements. C_2 is displaced from the focal point of the 4F system by δd, to tune the amplifier. 166

7.2 A simulation of a SAI amplifier where C_1 and C_2 are identical. In this case, each of the cells are $10mm$ long, $\chi_{PrPr} = 0.15 + 0i$, and χ_k is swept over a range of 0 – 0.23 rad mm^{-1}. These parameters are as similar to previous simulations as possible while producing similar levels of gain. This allows for a direct comparison between them. In this case $\delta d = 0mm$. 167

7.3 A simulation of a SAI amplifier where C_1 and C_2 are identical. In this case, each of the cells are $10mm$ long, $\chi_{PrPr} = 0.15 + 0i$, and χ_k is swept over a range of 0 – 0.23 rad mm^{-1}. These parameters are as similar to previous simulations as possible while producing similar levels of gain. This allows for a direct comparison between them. In this case $\delta d = 16mm$. 167

7.4 The range of displacements seen, over a gain range of $0 - 10$, against δd. . 168

7.5 The probe intensity profiles after exiting C_2, when $\delta d = 16$. 169

7.6 The conjugate intensity profiles after exiting C_2, when $\delta d = 16$. 169

A.1 A diagram of the mechanical part of the motorised translation stage; the various parts are labelled: T, translation stage; M, micrometer; F, flexure; C, coupling; S, stepper motor. 176

List of Tables

2.1 Some of the PIXIS-1024BR eXcelon's specifications. 63

5.1 The values of each static parameter for each parameter sweep. The blue-detuning is relative to the point of maximum gain of the 4WM, which not the 1-photon detuning resonance. In actuality, the absolute 1-photon detuning is on the order of 1 GHz from the resonance. 128

6.1 Calibration parameters for the BPD 148

INTRODUCTION

IT can be argued that light has been our most valuable analysis tool, from prehistory where it was first relied on for our dominant sense to the modern day when it finds incredibly diverse applications in producing precision measurements. This is particularly true since the advent of the laser [1]. Since then, lasers have been used to great effect in metrology, where their great spatial and temporal coherence allows for the generation of strong signals when they are used to take measurements.

The signal-to-noise ratio (SNR) of the system involved is what defines the limits on these measurements, and the quality of a measurement is given by the SNR.

For a coherent state, like that generated by a laser, the noise on the beam is the photonic shot noise. This shot noise is Poissonian and can be on the intensity and on the phase of the beam, with both potentially limiting precise measurements.

Often, the SNR can be improved by simply increasing the intensity of the beam, since a signal derived from that beam will be directly proportional to a laser's intensity whereas the quantum noise on the beam will only be proportional to the root of its intensity.

However, this is sometimes not possible, due to constraints on the maximum intensity

of a system. This can be due to limits on the power practically available or the intensity that is sustainable by the sample involved. A simple example of this is present in some biological measurements, where intense light sources can damage the sample being investigated.

In these cases, the only solution is to reduce noise with quantum phenomena. This can be achieved via a process called squeezing, where the noise on one parameter of a beam can be reduced below the quantum noise limit. This is at the cost of increasing the noise on another conjugated parameter. This is such that the uncertainty relation between those parameters is not violated.

One famous application of squeezing is in ultra-precise interferometers like LIGO, where the expected detection rate for compact binary mergers has been increased up to 50% [2].

Squeezing as a process can be realised in a number of ways and it is not exclusive to just photonic states [3]. Phonon states, ion motional states, and even the spin states of neutral atoms have been squeezed [4, 5]. When it comes to light, the primary methods of squeezed state generation rely on non-linear optics. One popular method is the use of degenerate parametric down-conversion, which exploits the second-order polarisation of a material to produce squeezed states. In fact, this method has been employed recently to produce a state at an astounding 15dB below the quantum noise [6].

Some other options involve four-wave-mixing (4WM). This method was the first to ever produce squeezed states in light [7]. However, it was abandoned in favour of second order interactions due to excess noise generated by fluorescence and absorption effects that second order interactions inherently do not suffer from since they occur far from resonance. Being far from resonance does have the disadvantage that the process has low gain however and, since a gain of a few units is required for good squeezing, this necessitates that an optical cavity must be used. This tends to limit the number of spatial

modes amplified at once and thus squeezed light generated this way has limited capacity to be used in imaging applications.

Recently, though, renewed interest has been seen in 4WM methods, specifically in employing a double lambda scheme that mitigates the earlier noise problems [8, 9, 10, 11, 12]. This scheme generates twin correlated beams and is the one used in this thesis. The benefit of this scheme is that a gain of a few units can be achieved in just a single pass, without a cavity. As such, the noise reduction tends to occur on many of the spatial modes of the beams. Such states are referred to as multi-spatial-mode (MSM) squeezed states.

Many more applications can be found for sources that produce MSM squeezed light, particularly within the field of quantum imaging [13, 14, 15]. A MSM source would mean that there will be correlations at the local level - i.e. if small subsections of the source were measured those would have correlations too. In the twin correlated beam case, this means that two small regions taken at roughly the same location in each beam will have correlated photon statistics. In this case, these regions would be squeezed with respect to the intensity difference between them.

This could be used in imaging, with one beam acting as a reference and another as the imaging beam. An image could then be generated by detecting the beams separately and combining them via subtraction electronically. Individual pixels on that image would be less noisy than those generated with a coherent beam [16, 17]. As a result, optically thin structures that would usually be so faint as to not be distinguishable from the background noise would become visible and the overall contrast of the quantum image would be improved too. One place this approach would be particularly useful is in the optical imaging of fragile and optically thin matter, such as the imaging of biological cells [18, 19].

One primary issue with using the 4WM generated squeezed twin beams for imaging is

that this system will only work if the classical noise is not too big. To this end, an active noise reduction system was implemented and this process is detailed in this thesis.

Another key issue is that, although localised correlations have been seen, the use of an extended medium introduces propagation effects that cause the correlated regions on each beam to not be displaced from each other by a constant amount [20]. This could be a significant barrier to the production of a squeezed image. A detailed view of this effect is explored in this thesis as well, and suggestions are made on how best to mitigate it.

In chapter 1, the quantum theory of light and squeezed state generation is discussed both generally and specifically to the system employed here. In chapter 2, the practical realisation of two-mode squeezed states is detailed and the general experimental design is discussed.

Chapter 3 covers the initial attempt to produce squeezed images and concludes that the classical noise was a significant limitation on this. This sets up chapter 4, which details the implementation of a noise eater, to counter this noise and help to solve the first primary issue.

Chapter 5 begins the investigations into the propagation effects of the extended medium, with a focus on how this affects the intensity distribution of the output beams. It also discusses a theoretical model for the beam propagations and simulations of it too. Chapter 6 follows up on this by extending the search to the quantum correlations and squeezing itself. It indicates that these are also affected by the propagation effects in much the same way. Chapter 7 details a potential all optical way to correct for the propagation effects.

Finally, the discussion is brought to an end and suggestions made for the future in the closing remarks in chapter 8.

Part I:

Generating Squeezed Light with 4WM

CHAPTER 1

THEORY

TO understand how squeezed light can be produced, the quantum description of light must be understood generally. This chapter will deal with such a description.

1.1 The Quantum Theory of Light

1.1.1 The Electromagnetic Field as a Simple Harmonic Oscillator

These next few sections follow Fox M. "Quantum Optics an Introduction" [21]. To see how the energy of a classical light field can be expressed as a simple harmonic oscillator (SHO) an x polarised electric field, $\xi_x(z,t)$, is first defined as

$$\xi_x(z,t) = \xi_0 \sin(kz) \sin(\omega t + \phi), \tag{1.1}$$

which represents a standing wave in a cavity. Where, k is the wave-vector of the field, ω is the angular frequency of it, and ϕ is an arbitrary phase. This is a mode – or a solution of Maxwell's equations [22]. Then, using the fourth Maxwell relation, the corresponding magnetic field B_y (Appendix A), can be shown to be given by

$$B_y(z,t) = B_0 \cos(kz) \cos(\omega t + \phi), \tag{1.2}$$

where $B_0 = \frac{\xi_0}{c}$.

Now taking the energy density of the system,

$$U = \frac{1}{2}(\epsilon_0 \xi_x^2 + \frac{B_y^2}{\mu_0}), \tag{1.3}$$

and integrating it over the total volume occupied results in a total energy given by [21]

$$E_{Tot} = \frac{1}{2}(\varepsilon(t)^2 + \beta(t)^2). \tag{1.4}$$

Where $\varepsilon(t)$ and $\beta(t)$ are the original $\xi(t)$ and $B(t)$ coordinates, after they have been integrated over volume, so that

$$\varepsilon(t) = \sqrt{\frac{\epsilon_0 V}{2}} \xi_0 \sin(\omega t + \phi) \tag{1.5}$$

and [21]

$$\beta(t) = \sqrt{\frac{V}{2\mu_0}} B_0 \cos(\omega t + \phi), \tag{1.6}$$

where V is the physical volume that is integrated over. Notice for equation 1.4 that the total energy is in a quadratic form similar to that of the classical SHO. Further, ε and β are conjugate variables in the classical Hamiltonian sense, i.e. they follow Hamilton's equations. Hence, the light wave can be expressed as a simple harmonic oscillator [23].

From this point, we will only be considering the contributions of the electric field to the system, as all effects wished to be described can be treated as purely electric.

The form of $\xi_x(t)$, however, is considered unwieldy, so it is more common to account for the arbitrary phase elsewhere and to also work in a dimensionless regime. This is done with a new coordinate system $X_1(t)$ and $X_2(t)$, where [21]

$$X_1(t) = \sqrt{\frac{\epsilon_0 V}{4\hbar\omega}}\xi_0 \sin(\omega t) \tag{1.7}$$

and

$$X_2(t) = \sqrt{\frac{\epsilon_0 V}{4\hbar\omega}}\xi_0 \cos(\omega t). \tag{1.8}$$

They are called field quadratures, notice that they also vary sinusoidally with a 90 degree phase mismatch.

These new coordinates can be related to the electric field by:

$$\xi_x(z,t) = \sqrt{\frac{4\hbar\omega}{\epsilon_0 V}} \sin(kz)(X_1 \cos\phi + X_2 \sin\phi), \tag{1.9}$$

retaining the original phase information.

Now that this field mode has been revealed as a SHO it can be quantised in the same way. In the standard number state representation for a quantum simple harmonic oscillator (QSHO), the field quadratures $\hat{X}_1$ and $\hat{X}_2$ can be represented as the operators

$$\hat{X}_1 = \frac{1}{2}(\hat{a}^\dagger + \hat{a}) \tag{1.10}$$

and

$$\hat{X}_2 = \frac{1}{2}i(\hat{a}^\dagger - \hat{a}), \tag{1.11}$$

where $a^\dagger$ and a are the photon creation and annihilation operators respectively [24]. Dipping slightly more into the quantum picture of light, the equations 1.4 and 1.5 can be used to show that the electric energy of this classical state is

$$E_{classical} = \frac{V}{4}\epsilon_0\xi_0^2. \tag{1.12}$$

which can be compared to the amplitude of 1.1 using the equation 1.9 to determine that

$$E_{classical} = \hbar\omega|A|^2, \tag{1.13}$$

where A is the contribution of $X_1 \cos\phi + X_2 \sin\phi$ to the amplitude of $\varepsilon_x(z,t)$.
Finally, equating to the standard QSHO result,

$$E_{Quantum} = \hbar\omega(n + \frac{1}{2}), \tag{1.14}$$

and neglecting the $\frac{1}{2}$ term, as it is the zero-point energy from the vacuum fluctuation [25]. It can be seen that

$$|A| \approx \sqrt{n}, \tag{1.15}$$

where n is the total number of particles in the QSHO.
Hence, the number of photons the light field consists of can be determined from the magnitude of the electric field, and by extension from the magnitude of the X_1 and X_2 quadratures.
Of course, this calculation is not rigorous, this approximate method is more to show a general relationship between these variables. Equation 1.13 should be understood as a kind of semi-classical approximation, since a state with a well-defined number of photons does not have a set energy and vice versa.

1.1.2 Uncertainty and the Electric Field

With the QSHO nature of light established, our understanding can be extended by applying some quantum mechanics.

First, recall that the variance, and hence the uncertainty of a quantum operator is given by [26]

$$(\Delta\hat{Y})^2 = \langle\hat{Y}^2\rangle - \langle\hat{Y}\rangle^2 . \tag{1.16}$$

Using the quantum operators of the field quadratures, the uncertainty relation between them can be found. This is done with the standard result [27],

$$(\Delta\hat{Y})^2(\Delta\hat{Z})^2 \geq \frac{|[\hat{Y},\hat{Z}]|^2}{4}. \tag{1.17}$$

Running through the calculation, noting that $[\hat{X}_1,\hat{X}_2] = \frac{1}{2}[\hat{a},\hat{a}^\dagger] = \frac{1}{2}$, gives the uncertainty relation between the quadratures of

$$\Delta\hat{X}_1\Delta\hat{X}_2 \geq \frac{1}{4}, \tag{1.18}$$

which defines the maximum precision these two quadratures can ever be measured to simultaneously.

Now we apply this result to a coherent state, which is the closest analogue of a classical monochromatic wave in quantum mechanics [28]. A coherent state is a minimum uncertainty state with equal uncertainties on each of its quadratures, so it is safe to assume that [29]

$$\Delta\hat{X}_1 = \Delta\hat{X}_2 = \frac{1}{2}. \tag{1.19}$$

Representing this on an electric field phasor diagram (figure 1.1 A)), the uncertainties produce a symmetric haze around the classical magnitude of the state. In reality, the un-

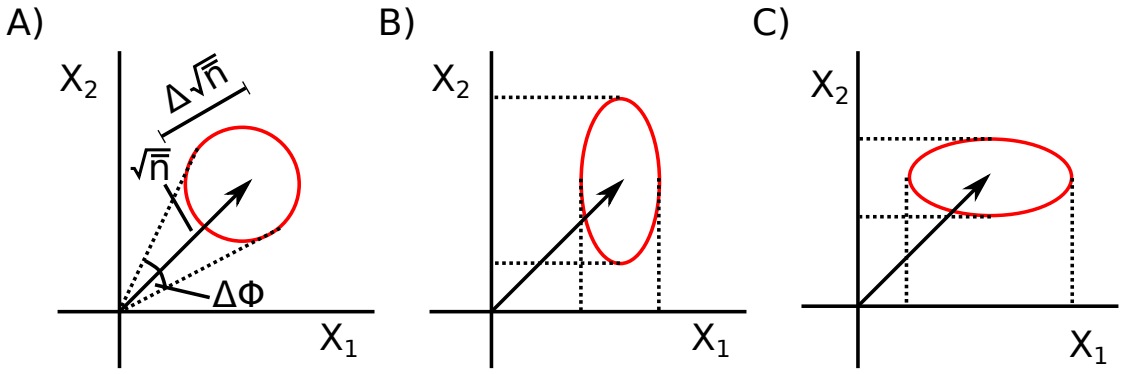


Figure 1.1: A) A coherent state, expressed in terms of the X_1 and X_2 quadratures [21]. In reality, the uncertainty of the state is given by a Gaussian probability density function (PDF) centred on the tip of the phasor, but for clarity this distribution is represented by a red circle with a radius equal to 1σ of the PDF. B) A squeezed state, where the uncertainty on X_1 (seen by the projection of the PDF onto the horizontal axis) is reduced at the expense of increasing the uncertainty on X_2 (seen by the projection of the PDF onto the vertical axis). B) A squeezed state, where the uncertainty on X_2 (seen by the projection of the PDF onto the vertical axis) is reduced at the expense of increasing the uncertainty on X_1 (seen by the projection of the PDF onto the horizontal axis).

certainty of the state is given by a Gaussian probability density function (PDF) centred on the tip of the phasor, but for clarity this distribution is represented by a red circle with a radius equal to 1σ of the PDF. Figures 1.1 B) and 1.1 C) show what squeezing the X_1 and the X_2 quadratures respectively would look like. In these cases, the uncertainty on one parameter is reduced at the expense of increasing the uncertainty on the other. As such, the circular haze around the tip of the phasor becomes elliptical, and the projection of the PDF onto one of the axis shrinks while the projection onto the other grows. The total area of the ellipse can never decrease below the area of a coherent state, but it may grow. For a minimum uncertainty state, however, the total area of the shape remains constant.

The pictorial representation in figure 1.1 A) highlights how the rather abstract uncertainties $\Delta\hat{X}_1$ and $\Delta\hat{X}_2$ relate to the more familiar uncertainties of photon number, Δn, and phase, $\Delta\phi$.

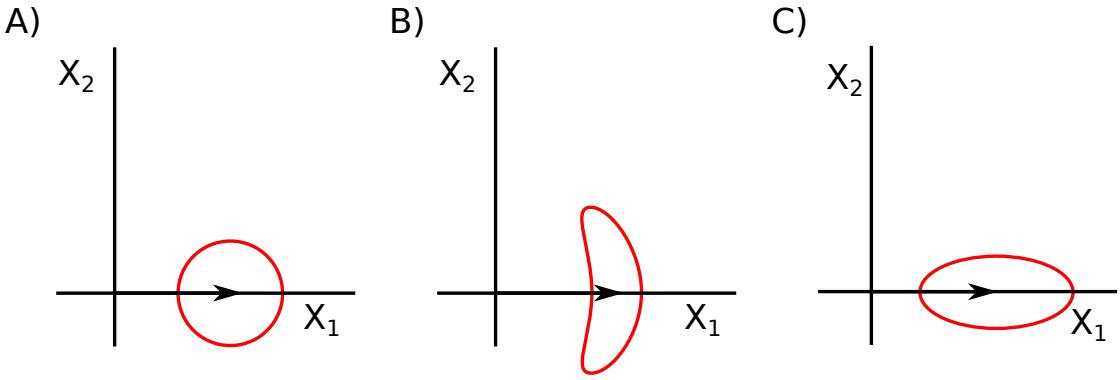


Figure 1.2: Three electric field phasor diagrams where ϕ is chosen to be 0, hence $A = X_1$. A) A coherent state. B) An intensity squeezed state. C) a phase squeezed state.

The nature of these uncertainties can be defined by first noting that because $n = A^2$ it can be shown by differentiation that

$$\Delta n = 2A\Delta A = 2\sqrt{n}\Delta A. \tag{1.20}$$

Then, setting $\phi = 0$, since phase is a relative measurement and the choice of what point to start measuring it is arbitrary, it can be seen that $\Delta A = \Delta X_1$ (figure 1.2). Therefore

$$\Delta n = 2\sqrt{n}\frac{1}{2} = \sqrt{n}. \tag{1.21}$$

This demonstrates that for a symmetric minimum uncertainty state like a coherent state, the minimum possible uncertainty on the photon number (and hence noise on the signal) is the root of the photon number [21]. The key takeaway here is that the shot noise on the state comes from the random distribution of the uncorrelated photons within it, hence the uncertainty rises as the number of photons increases. This distribution is similar to the often used Poisson distribution.

Then, again setting $\phi = 0$ and applying the small angle approximation, it can be seen

that

$$\Delta\phi = \frac{\Delta X_2}{X_1}. \tag{1.22}$$

Again, noting that $X_1 = A = \sqrt{n}$ and that for a coherent state $X_2 = \frac{1}{2}$ this becomes

$$\Delta\phi = \frac{1}{2\sqrt{n}} \tag{1.23}$$

By multiplying these results together a key uncertainty relation for a single beam,

$$\Delta n \Delta\phi \geq \frac{1}{2}, \tag{1.24}$$

is demonstrated.

From looking at relation 1.24 it can be seen that, mathematically speaking, the uncertainty on n can be reduced at the expense of increasing the uncertainty on ϕ. It is possible to produce such states, known as intensity squeezed states. In this case, only one mode would be involved. There are other forms of squeezing such as quadrature squeezing, where the uncertainty on the quadratures themselves are squeezed, and two mode squeezing which is the type employed in this thesis. In this case, the intensity difference between the beams is squeezed.

Squeezing requires that correlations are developed between photons. These correlations are induced by some form of interaction. As such, squeezing can be achieved via quantum mechanical techniques that facilitate photon-photon interactions, resulting in a smoothing of the noise.

1.1.3 The Optical Amplifier

An understanding of how squeezing can be induced can be provided by the study of the optical amplifier. Further, by studying the differences between single mode and two mode amplifiers, it can be seen that a two mode amplifier is necessary to amplify light at all. Further, it can be seen how it produces squeezed states as a consequence of its amplification. For this, we can rely on the electrical field quantisation for a wave travelling in the z direction,

$$\hat{E}(\gamma) = \hat{E}^{+}(\gamma) + \hat{E}^{-}(\gamma) = \hat{a}e^{-i\gamma} + \hat{a}^{\dagger}e^{i\gamma}, \tag{1.25}$$

made elegant by the convention that electric field is measured in units of $(\hbar\omega/2\epsilon_0 V)^{1/2}$ and where the dependences on z and time, t, are contained within the phase angle

$$\gamma = \omega t - kz - \frac{\pi}{2}. \tag{1.26}$$

Here, k refers to the wave vector of the field. It is convenient to quantise in this way, as it separates the field operator into the creation and annihilation operators. Now, a hypothetical structure can be imagined wherein the amplitude of some input field E would grow proportional to its magnitude. This is represented by

$$\frac{\partial E(z)}{\partial z} = \kappa E(z), \tag{1.27}$$

where κ is the growth constant. This would constitute a single mode optical amplifier.

The solution to this equation is just an exponential function

$$E(z) = Ee^{\kappa z} = E\sqrt{G(z)}, \tag{1.28}$$

where G is defined as $e^{2\kappa z}$. Quantisation amounts to $E \to \hat{E}^+$. We are allowed to treat only $\hat{E}^+$ since $\hat{E}^+$ and $\hat{E}^-$ are Hermite conjugates of each other, and they are combined linearly in $\hat{E}$. As such, the results will be identical for $\hat{E}$ and $\hat{E}^+$.
We consider

$$\hat{E}^+(z) = \hat{E}^+\sqrt{G(z)} \tag{1.29}$$

So, the commutation relation for the input beam is

$$[a_{in}, a_{in}^\dagger] = \hat{E}^+\hat{E}^{+\dagger} - \hat{E}^{+\dagger}\hat{E}^+ = \hat{a}_{in}\hat{a}_{in}^\dagger - \hat{a}_{in}^\dagger\hat{a}_{in} = 1 \tag{1.30}$$

and the output commutation relation is found to be

$$[\hat{a}_{out}, \hat{a}_{out}^\dagger] = G(\hat{E}^+\hat{E}^{+\dagger} - \hat{E}^{+\dagger}\hat{E}^+) = G(\hat{a}_{in}\hat{a}_{in}^\dagger - \hat{a}_{in}^\dagger\hat{a}_{in}) = G. \tag{1.31}$$

This represents a problem, since the output commutation highlights that a_{out} is not the operator that is expected and does not describe a QHO. It turns out, in fact, that at least two input modes must be considered for a tenable theory of optical amplification. To construct an example two mode system, another hypothetical structure is imagined, where two fields, E_1 and E_2, grow as

$$\frac{\partial E_1(z)}{\partial z} = \kappa E_2^*(z);\ \frac{\partial E_2^*(z)}{\partial z} = \kappa E_1(z). \tag{1.32}$$

The solution to these coupled differential equations comes by the matrix method. First,

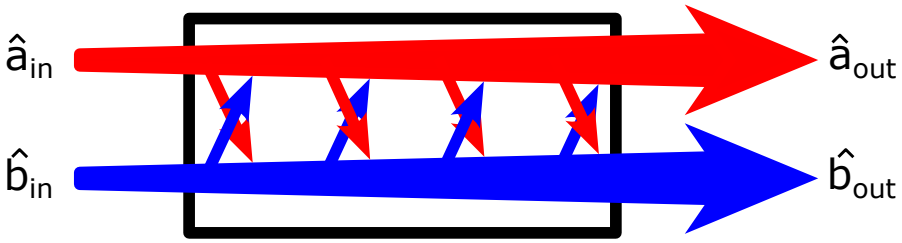


Figure 1.3: A representation of a two mode optical amplifier acting on two fields with the creation operators $\hat{a}$ and $\hat{b}$ respectively.

the system is expressed in the matrix form,

$$\frac{\partial}{\partial z}\begin{pmatrix} E_1 \\ E_2^* \end{pmatrix} = \kappa \begin{pmatrix} 0 & 1 \\ 1 & 0 \end{pmatrix} \begin{pmatrix} E_1 \\ E_2^* \end{pmatrix}. \tag{1.33}$$

Next

$$E(z) = ve^{\lambda z} \tag{1.34}$$

is taken as the ansatz. Upon substitution to equation 1.33 and cancellation, it becomes the eigenvalue problem

$$\kappa A v = \lambda v \tag{1.35}$$

where A represents the matrix and v the vector of the fields. The characteristic equation can then be found using the relation

$$det(\kappa A - \lambda I) = 0. \tag{1.36}$$

This results in the eigenvalues

$$\lambda_1 = \kappa;\ \lambda_2 = -\kappa \tag{1.37}$$

with corresponding eigenvectors

$$v_1 = \begin{pmatrix} 1 \\ 1 \end{pmatrix} ; \; v_2 = \begin{pmatrix} 1 \\ -1 \end{pmatrix}. \tag{1.38}$$

Therefore the general solution is

$$\begin{pmatrix} E_1 \\ E_2^* \end{pmatrix} = c_1 \begin{pmatrix} 1 \\ 1 \end{pmatrix} e^{\kappa z} + c_2 \begin{pmatrix} 1 \\ -1 \end{pmatrix} e^{-\kappa z} \tag{1.39}$$

which can be more neatly expressed as

$$E_1(z) = c_1 e^{\kappa z} + c_2 e^{-\kappa z} \tag{1.40}$$

$$E_2^*(z) = c_1 e^{\kappa z} - c_2 e^{-\kappa z}. \tag{1.41}$$

To find the coefficients c_1 and c_2 the system is considered at z=0, where

$$E_{1,0} = c_1 + c_2 \tag{1.42}$$

$$E_{2,0}^* = c_1 - c_2. \tag{1.43}$$

This begets

$$c_1 = \frac{E_{1,0} + E_{2,0}^*}{2} \tag{1.44}$$

$$c_2 = \frac{E_{1,0} - E_{2,0}^*}{2}, \tag{1.45}$$

so

$$E_1(z) = E_{1,0} cosh(\kappa z) + E_{2,0}^* sinh(\kappa z) \tag{1.46}$$

$$E_2^*(z) = E_{1,0} sinh(\kappa z) + E_{2,0}^* cosh(\kappa z). \tag{1.47}$$

These can be quantised with equation 1.25 also; once again only the $\hat{E}^+$ part of the expression is considered, for brevity. This is still valid for the reasons outlined in the single mode case. As before, the commutation relations for the unamplified fields come to one. Further, counter to the single mode case, the amplified fields commute as

$$[\hat{E}_1, \hat{E}_1^*] = (\hat{E}_{1,0}c + \hat{E}_{2,0}^* s)(\hat{E}_{1,0}^* c + \hat{E}_{2,0} s) - (\hat{E}_{1,0}c + \hat{E}_{2,0}^* s)(\hat{E}_{1,0}^* c + \hat{E}_{2,0} s) \tag{1.48}$$

where $c = cosh(\kappa z)$ and $s = sinh(\kappa z)$. This reduces to

$$[\hat{E}_1, \hat{E}_1^\dagger]c^2 - [\hat{E}_2, \hat{E}_2^\dagger]s^2 = [\hat{a}, \hat{a}^\dagger]c^2 - [\hat{b}, \hat{b}^\dagger]s^2 = c^2 - s^2 = 1, \tag{1.49}$$

by the standard hyperbolic identity $cosh^2(u) - sinh^2(u) \equiv 1$. A similar analysis on equation 1.47 renders

$$[\hat{E}_2, \hat{E}_2^\dagger] = 1 \tag{1.50}$$

too. Thus, the output of this two mode amplifier produces solutions of the QHO, as expected. Hence, this structure can be readily theoretically understood.

To see how such a construction would result in a squeezed state, consider a single input mode. In this case, only one mode is populated, and the other is in a vacuum state. Initially, the only noise on the system are the quantum fluctuations on that populated input mode, n_0. After amplification, with a gain of G, both modes are populated. An optical amplifier in practice works by exposing the modes to a gain media, which will undergo stimulated emission to feed the growth of the modes. As such, due to the random nature of stimulated emission, the populated modes are noisy. However, photons in each of the modes must be created pairwise and are thus perfectly correlated. If the output modes were measured with photodetectors and the output signals of those detectors subtracted from each other, the only noise remaining would be that of the initial input mode. This is because the shot noise on each of the beams is identicle and is cancelled

by the subtraction. Yet, the output modes are of a total intensity larger than before. Overall, the ratio of the actual noise on the subtracted modes against the expected noise for a coherent state of the same magnitude is

$$\frac{n_0}{(2G-1)n_0} = \frac{1}{2G-1} \tag{1.51}$$

hence, the subtracted two-mode state is squeezed.

A more rigorous argument can be made by interrogating the uncertainty of the subtracted two mode state, before and after amplification, using the standard uncertainty relation

$$\langle \Delta \hat{S}^2 \rangle = \langle \hat{S}^2 \rangle - \langle \hat{S} \rangle^2 \tag{1.52}$$

for the subtracted field operator, S, with the initial two-mode coherent state $|\alpha, 0\rangle$.

In the case of the initial beams, this is $S_{in} = \hat{a}_{in}^\dagger \hat{a}_{in} - \hat{b}_{in}^\dagger \hat{b}_{in}$. So, the first term in equation 1.52 is given by

$$\langle \hat{S}_{in}^2 \rangle = \langle \alpha, 0 | \, (\hat{a}_{in}^\dagger \hat{a}_{in} - \hat{b}_{in}^\dagger \hat{b}_{in})(\hat{a}_{in}^\dagger \hat{a}_{in} - \hat{b}_{in}^\dagger \hat{b}_{in}) \, | \alpha, 0 \rangle = \langle \alpha | \, \hat{a}_{in}^\dagger \hat{a}_{in} \hat{a}_{in}^\dagger \hat{a}_{in} \, | \alpha \rangle \, . \tag{1.53}$$

This can be simplified by the standard result

$$\hat{a}\hat{a}^\dagger = 1 + \hat{a}^\dagger \hat{a}. \tag{1.54}$$

So $\langle \hat{S}_{in}^2 \rangle$ becomes

$$\langle \hat{S}_{in}^2 \rangle = \langle \alpha | \, \hat{a}_{in}^\dagger \hat{a}_{in} + \hat{a}_{in}^\dagger \hat{a}_{in}^\dagger \hat{a}_{in} \hat{a}_{in} \, | \alpha \rangle = (|\alpha|^2 + |\alpha|^4). \tag{1.55}$$

The second part of equation 1.52 is simply

$$\langle \hat{S}_{in} \rangle^2 = \langle \alpha, 0 | \, \hat{a}_{in}^\dagger \hat{a}_{in} - \hat{b}_{in}^\dagger \hat{b}_{in} \, | \alpha, 0 \rangle = \langle \alpha | \, \hat{a}_{in}^\dagger \hat{a}_{in} \, | \alpha \rangle = |\alpha|^4 \tag{1.56}$$

with the result that

$$\langle \Delta \hat{S}_{in}^2 \rangle = (|\alpha|^2 + |\alpha|^4) - |\alpha|^4. \tag{1.57}$$

So

$$\langle \Delta \hat{S}_{in} \rangle = |\alpha| \tag{1.58}$$

in the pre-amplified case.

In the amplified case the operator becomes

$$\hat{S}_{out} = (\hat{a}_{in}^\dagger c + \hat{b}_{in} s)(\hat{a}_{in} c + \hat{b}_{in}^\dagger s) - (\hat{a}_{in} s + \hat{b}_{in}^\dagger c)(\hat{a}_{in}^\dagger s + \hat{b}_{in} c), \tag{1.59}$$

since $\hat{a}_{out} = \hat{a}_{in} c + \hat{b}_{in}^\dagger s$ and $\hat{b}_{out} = \hat{a}_{in}^\dagger s + \hat{b}_{in} c$ as according to equations 1.46 and 1.47. Applying this to equation 1.52 with the initial state $|\alpha, 0\rangle$ the first part of the expression becomes

$$\langle \hat{S}_{out}^2 \rangle = |\alpha|^4 + |\alpha|^2, \tag{1.60}$$

The second part of equation 1.52 becomes

$$\langle \hat{S}_{out}^2 \rangle = (c^2 |\alpha|^2 - s^2 |\alpha|^2)^2 = |\alpha|^4 \tag{1.61}$$

once again applying the standard identity $c^2 - s^2 \equiv 1$ and so the final result is

$$\langle \Delta \hat{S}_{out}^2 \rangle = (|\alpha|^2 + |\alpha|^4) - |\alpha|^4 = |\alpha|^2, \tag{1.62}$$

or

$$\langle \Delta \hat{S}_{out} \rangle = |\alpha| \tag{1.63}$$

which is identical to the unamplified case.

As a result, the noise on the subtracted modes remains at the level of the initial seed despite amplification, and is squeezed. This is lower than the noise that would be present on subtracted uncorrelated modes of the same magnitudes. This is because the noise on each mode would depend on the amplitude of those modes and would be added together when the modes were combined by subtraction, as there would be no correlations to cancel the noise.

It is worth comparing this to the amplitude of the amplified modes. These can be found by finding $\langle N_a^{out} \rangle$ and $\langle N_b^{out} \rangle$ where $N_a^{out} = \hat{a}_{out}^\dagger \hat{a}_{out}$ and $N_b^{out} = \hat{b}_{out}^\dagger \hat{b}_{out}$. This gives

$$\langle N_a^{out} \rangle = |\alpha|^2 c^2 + s^2 \tag{1.64}$$

and

$$\langle N_b^{out} \rangle = (|\alpha|^2 + 1) s^2. \tag{1.65}$$

This also gives what would be the variance on coherent states of the same magnitudes, which is be given by their number state amplitudes.

The actual amplitude noise on each individual mode can be found by finding $\langle (\Delta N_a^{out})^2 \rangle$ and $\langle (\Delta N_b^{out})^2 \rangle$ using the standard uncertainty relation. This results in

$$\langle (\Delta N_a^{out})^2 \rangle = |\alpha|^2 c^4 + (|\alpha|^2 + 1) c^2 s^2 \tag{1.66}$$

and

$$\langle (\Delta N_b^{out})^2 \rangle = (|\alpha|^2 + 1) c^2 s^2. \tag{1.67}$$

Since $c > 1$ and $s > 1$ is always true, the variance of the number state on each beam is larger than the variance on coherent states of the same intensities (equations 1.64 and 1.65), in both cases. Therefore, the individual modes are anti-squeezed by the amplification process.

1.1.4 Two-Mode Squeezing

A more in-depth understanding of the two mode squeezed state can be obtained by considering the mode squeezing operator [30]. This is given by

$$\hat{S}_2(\xi) = e^{(\xi^* \hat{a}\hat{b} - \xi \hat{a}^\dagger \hat{b}^\dagger)}, \tag{1.68}$$

where

$$\xi = re^{i\theta}, \tag{1.69}$$

where r is referred to the squeezing parameter, θ is an arbitrary phase and r and θ are restricted to $0 \leq r < \infty$ and $0 \leq \theta \leq 2\pi$. θ determines the angle of the quadrature that is being squeezed and r determines the magnitude of the squeezing.
$\hat{a}$, $\hat{a}^\dagger$, $\hat{b}$, and $\hat{b}^\dagger$ are defined as the annihilation and creation operators of the different modes respectively [31].
It can be seen from the form of this operator that photons are created and destroyed pairwise in each beam in this interaction, leading to the aforementioned entanglement.

The Action of these operators on a vacuum state

First, note that the squeezing in this case actually occurs on the superpositions of the beams. As such, it is convenient to redefine X_1 and X_2 as the superimposed quadrature

operators

$$\hat{X}_1 = \frac{1}{2^{\frac{3}{2}}}(\hat{a}^\dagger + \hat{a} + \hat{b}^\dagger + \hat{b}), \tag{1.70}$$

and

$$\hat{X}_2 = \frac{1}{2^{\frac{3}{2}}}(\hat{a}^\dagger - \hat{a} + \hat{b}^\dagger - \hat{b}). \tag{1.71}$$

The effect that $\hat{S}_2$ will produce on the variance of the superimposed quadratures, given by

$$\langle \Delta \hat{X}_1^2 \rangle = \langle 0,0| \hat{S}_2^\dagger(\xi) \hat{X}_1^2 \hat{S}_2(\xi) |0,0\rangle - \langle 0,0| \hat{S}_2^\dagger(\xi) \hat{X}_1 \hat{S}_2(\xi) |0,0\rangle^2 \tag{1.72}$$

and

$$\langle \Delta \hat{X}_2^2 \rangle = \langle 0,0| \hat{S}_2^\dagger(\xi) X_2^2 \hat{S}_2(\xi) |0,0\rangle - \langle 0,0| \hat{S}_2^\dagger(\xi) X_2 \hat{S}_2(\xi) |0,0\rangle^2 \tag{1.73}$$

can be shown to be

$$\langle \Delta \hat{X}_1^2 \rangle = \langle \hat{X}_1^2 \rangle = \frac{1}{4}(\cosh^2 r + \sinh^2 r + 2 \sinh r \cosh r \cos\theta), \tag{1.74}$$

and

$$\langle \Delta \hat{X}_2^2 \rangle = \langle \hat{X}_2^2 \rangle = \frac{1}{4}(\cosh^2 r + \sinh^2 r - 2 \sinh r \cosh r \cos\theta)[31]. \tag{1.75}$$

Noting that

$$\langle 0,0| \hat{S}_2^\dagger(\xi) X_1 \hat{S}_2(\xi) |0,0\rangle^2 = \langle 0,0| \hat{S}_2^\dagger(\xi) X_2 \hat{S}_2(\xi) |0,0\rangle^2 = \langle \hat{X}_1 \rangle = \langle \hat{X}_2 \rangle = 0. \tag{1.76}$$

Now, taking the case where $\theta = 0$, produces

$$\langle \hat{X}_1^2 \rangle = \frac{1}{4} e^{-2r} \tag{1.77}$$

and

$$\langle \hat{X}_2^2 \rangle = \frac{1}{4} e^{2r}. \tag{1.78}$$

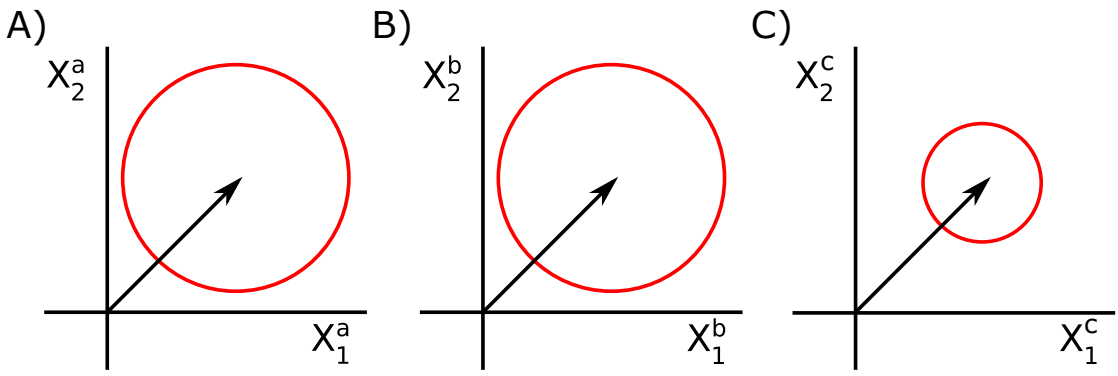


Figure 1.4: Two electric field phasor diagrams depicting uncertainty on the single mode $X_1^{a,b}$ and $X_2^{a,b}$ quadratures of modes a and b. Since these modes are super-Poissonian their Gaussian Wigner functions have a width larger than a minimum uncertainty coherent state (C) [33].

By changing the squeezing parameter, it is possible to squeeze one superposition of the modes and reduce its uncertainty, at the expense of the other.

Hence, a system can be tailored such that subtracted modes will produce sub-Poissonian number state variance, even if each individual mode is super-Poissonian. As previously discussed, the individual modes generated are actually noisier than coherent states of the same amplitudes. In fact, they are thermal-like and anti-squeezed in their individual quadratures, as depicted in figure 1.4 [32].

1.2 Non-Linear Optics

Following on from the previous section, it seems that if photons could be caused to interact, and hence entangle and squeeze, the shot noise on measurements made using them could be reduced. Thus, some way is needed to facilitate the interaction between photons. This is where non-linear optics comes in. This section will outline how non-linear media can be used to this effect.

1.2.1 The Polarisation of a Medium

The polarisation of a medium is usually defined as the electric dipole moment per unit volume in a material, and is a vector quantity [34, 35]. Many materials can be represented as dielectrics, which are substances that become polarised when subjected to an electric field. Typically, this is a feature of non-conductive media, since all dielectric materials are insulators. However, a good dielectric is also easily polarisable. Assuming the incident light is of relatively low intensity (linear regime), the polarisation of a dielectric material can be modelled by

$$P(t) = \epsilon_0 \chi^{(1)} E(t), \tag{1.79}$$

where $P(t)$ is the polarisation at any given time, ϵ_0 is the electric permittivity of free space, $\chi^{(1)}$ is the first order electric susceptibility and $E(t)$ is the electric field at a given time [36].

The first order susceptibility is given as a complex scalar, this accounts for the two physical responses of the media to incident light: refraction and absorption. This complex susceptibility leads to a complex refractive index, n, given by the relation

$$n(f) = \sqrt{1 + \chi^{(1)}(f)} \tag{1.80}$$

at frequency, f.

For higher intensities, the polarizability of a material can start to saturate, entering a non-linear regime. This trend can be approximated via a Taylor's expansion. Thus, a more complete version of equation 1.79 would be

$$P(t) = \epsilon_0 \sum_{n}^{\infty} \chi^{(n)} E(t)^n, \tag{1.81}$$

$\chi^{(n)}$ is the nth-order susceptibility tensor [37].

Now consider the wave equation in a nonlinear optical medium, which is given by [38]

$$\nabla^2 E(r,t) - \frac{1}{c^2}\frac{\mathrm{d}^2 E(r,t)}{\mathrm{d}t^2} = \frac{1}{\epsilon_0 c^2}\frac{\mathrm{d}^2 P(r,t)}{\mathrm{d}t^2}. \tag{1.82}$$

For two fields of different frequencies, ω_1 and ω_2, interacting in a medium with a significant second order susceptibility, $\chi^{(2)}$, from equation 1.81 the polarisation is given by

$$P(t)^{(2)} = \epsilon_0 \chi^{(2)}(E_1 e^{-i\omega_1 t} + E_2 e^{-i\omega_2 t} + c.c)^2, \tag{1.83}$$

where E_1 and E_2 are the complex amplitudes of the fields in question and *c.c.* is representative of the complex conjugate of the rest of the expression.

This results in a polarisation response given by [30]

$$\begin{aligned} P(t)^{(2)} = \epsilon_0 \chi^{(2)}[&E_1^2 e^{-2i\omega_1 t} + E_2^2 e^{-2i\omega_2 t} + 2E_1 E_2 e^{-(\omega_1+\omega_2)t} + 2E_1 E_2^* e^{-(\omega_1-\omega_2)t} + c.c.] \\ &+[E_1 E_1^* + E_2 E_2^*]. \end{aligned} \tag{1.84}$$

When these terms are substituted into equation 1.82, it can be seen that new fields are generated at the frequencies $2\omega_1$, $2\omega_2$, $(\omega_1 - \omega_2)$, and $(\omega_1 + \omega_2)$. A non-fluctuating component given by $[E_1 E_1^* + E_2 E_2^*]$ is also seen, which is often referred to as optical rectification [39]. This is simply means that the polarisation has a non-zero average value.

To take this step further, it can be shown that the full formal way of representing the polarisation response of a material subjected to a number of monochromatic fields, $E_i(\omega_i)$,

can be given by

$$P_i^n(\omega_{total} = \omega_a + \omega_b + ...) = \epsilon_0 \sum_{jk...} \sum_{(ab...)} \chi^{(n)}_{ijk...}(\omega_{total} = \omega_a + \omega_b + ...; \omega_a, \omega_b, ...) E_j(\omega_a) E_k(\omega_b) ... \,, \tag{1.85}$$

where P_i is the polarisation in a given axis ($i = x, y, z$); $\omega_{a,b,...}$ are the incident frequencies; The summation $\sum_{(ab...)}$ iterates over all the possible combinations of the frequencies $\omega_{a,b,..}$ and the parentheses indicate that their total sum ($\omega_{total} = \omega_a + \omega_b + ...$) does not change; $E_{j,k,..}(\omega_{a,b,..})$ represents the electric field oscillations, in each of the orthogonal axes; $\chi^{(n)}_{ijk...}(\omega_a + \omega_b + ...; \omega_a, \omega_b, ...)$ is a rank n tensor. The summation $\sum_{jk...}$ sums over all combinations of $j = x, y, z$; $k = x, y, z$; etc. It should also be noted that the time domain order the frequencies interact in is given by their order in the latter half of $\chi^{(n)}_{ijk...}$. These fields, like those of free space EM waves, can be quantised too. The only difference in this case is that the interaction terms between the fields must be included too, since this process operates in a dielectric medium. As a result, positive frequencies would indicate that photons were being added to a field, whereas negative frequencies would indicate that photons were being annihilated from a field. This leads to the interpretation that the negative frequencies correspond to energy being released by the medium and positive frequencies would indicate energy being absorbed [21, 30].

Therefore, the susceptibility of a material may depend on the direction it is viewed in, the different frequencies being dealt with, the order in which the interaction occurs, and that the incident fields may be oscillating in any of the spatial axes.

Usually, the magnitude of the susceptibility tensor elements decreases rapidly at higher orders [30]. However, in some specific circumstances, like atomic resonances, these elements can have much larger values, allowing their effects to be competitive with linear processes [40].

In certain systems, all the even indexed susceptibilities are zero. This is due to the system

having inversion symmetry, i.e. it can be modelled as a point group where every point, $\vec{r}$, has a corresponding identical point at $-\vec{r}$. This is true for system covered in this thesis, a Rb vapour, since the atoms of the vapour are randomly distributed in the medium - making it isotropic and homogeneous. We call such systems centrosymmetric [41]. In these systems, the third order susceptibility reigns, as it is the lowest order non-zero nonlinear term. Following from equation 1.85, the third order polarisation response to three input fields can be represented as

$$P_i(\omega_a + \omega_b + \omega_c) = \epsilon_0 \sum_{jkl} \sum_{(abc)} \chi^{(3)}_{ijkl}(\omega_a + \omega_b + \omega_c; \omega_a, \omega_b, \omega_c) E_j(\omega_a) E_k(\omega_b) E_l(\omega_c) \ , \tag{1.86}$$

This equation expands to 210 tensor terms (17,010 individual elements). This is an impractically large equation to deal with analytically, but it does show the great range of effects third order nonlinearity can lead to.

The complexities of equation 1.86 can often be reduced further using certain symmetries. For example, in an isotropic system, such as the atomic vapour being studied, the susceptibility tensor will be invariant over any rotation. As a result, equation 1.86 can be rewritten as

$$P_i(\omega_a + \omega_b + \omega_c) = \epsilon_0 \sum_{jkl} \sum_{(abc)} T_{ijkl} \chi^{(3)}(\omega_a + \omega_b + \omega_c; \omega_a, \omega_b, \omega_c)' E_j(\omega_a) E_k(\omega_b) E_l(\omega_c), \tag{1.87}$$

where $\chi^{(3)\prime}$ is a complex scalar, that depends solely on the input field frequencies and their order of interaction, and T_{ijkl} is a fourth order tensor that is invariant to arbitrary rotation given by

$$T_{ijkl} = (\delta_{ij}\delta_{kl} + \delta_{ik}\delta_{jl} + \delta_{il}\delta_{jk}) \ , \tag{1.88}$$

as this tensor is identical over all orthogonal transformations [42].

It can now be seen that a large part of the complexity of the system has origins in the

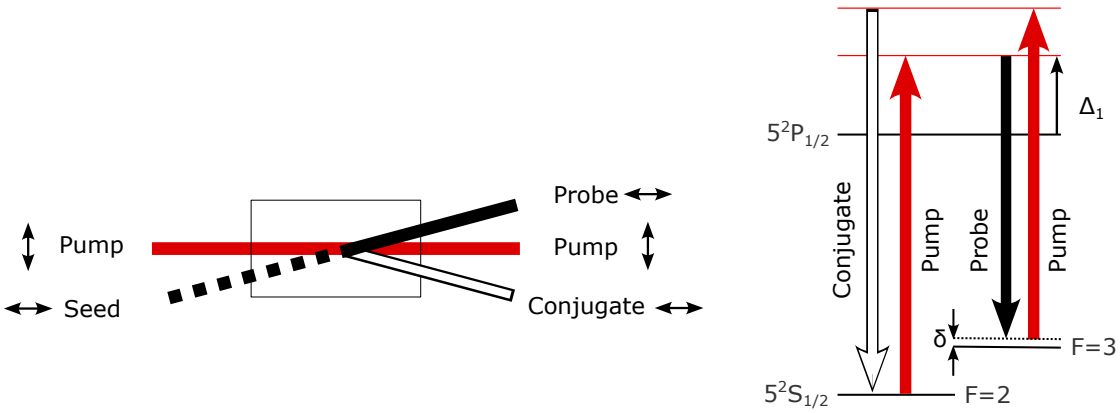


Figure 1.5: Left: A diagram of the geometry of the 4WM within the Rb cell. The double ended arrows next to each beam refer to the orthogonal polarisations of those beams as veiwed on the x-y plane tangental to the propagation direction of the beam, z. Right: The double lambda transition on the D1 line of 85Rb. The two detunings labelled Δ_1 and δ are called the one-photon detuning and two-photon detuning respectively.

number of possible combinations of the input fields (i.e. $\omega_d = \pm\,\omega_a \pm\, \omega_b \pm\, \omega_c$), the order in which they interact and also the polarisation states of the input fields. This still results in a huge number of possible interactions.

At this point, simplifying this equation further, requires more in-depth knowledge of the process being interrogated, which is 4WM in a rubidium vapour.

1.2.2 Four Wave Mixing in Rubidium

Figure 1.5 (right) shows a diagram of the 4WM process used to produce the correlated beams. This is a third order nonlinear process that uses hot Rubidium vapour as the medium.

The system is limited to three different frequencies, with the pump counting for two of the four mixed waves. In practice, this is done by stimulating our vapour with a powerful pump beam and then seeding the process with a weak probe seed beam, injected at an angle into the cell (figure 1.5 left). This is necessary to ensure that phase mismatch does

not occur.

1.2.3 The Phase Matching Condition

The issue of phase mismatch can be thought of as an extension of the energy and momentum conservation of the probe and conjugate beams. 4WM is a parametric process, which is to say the cycle starts and ends on the same energy level. This is because there are no other mechanisms acting to 'recycle' the atoms involved in the interactions, neglecting those atoms that enter and exit the laser beam during the process. Considering this, the relations

$$2n_p\vec{k_p} = n_{pr}\vec{k_{pr}} + n_c\vec{k_c} \tag{1.89}$$

and

$$2\omega_p = \omega_{pr} + \omega_c, \tag{1.90}$$

hold true, where $n_{p,pr,c}$ is the refractive index in the medium for each of the beams, $k_{p,pr,c}$ is the wave vector of each of the beams in a vacuum, and $\omega_{p,pr,c}$ is the angular frequency of each of the beams. Where the P, Pr, and C subscript represents the pump, probe, and conjugate beams.

Although these can be interpreted as the result of conservation relations, they originate in the 4WM propagation equations within the nonlinear medium. If these relations are not fulfilled then quickly oscillating terms in the polarisation prevent the growth of the probe and conjugate fields [43]. The presence of the n_i terms is necessary to account for the index of refraction within the media.

As shown in figure 1.6, the phase matching in free space (left) can be achieved when all the beams are parallel to each other. This is because the magnitude of $|2k_p|$ is equal to $|k_{Pr} + k_c|$, due to conservation of energy. However, in Rubidium-85, the beams may have

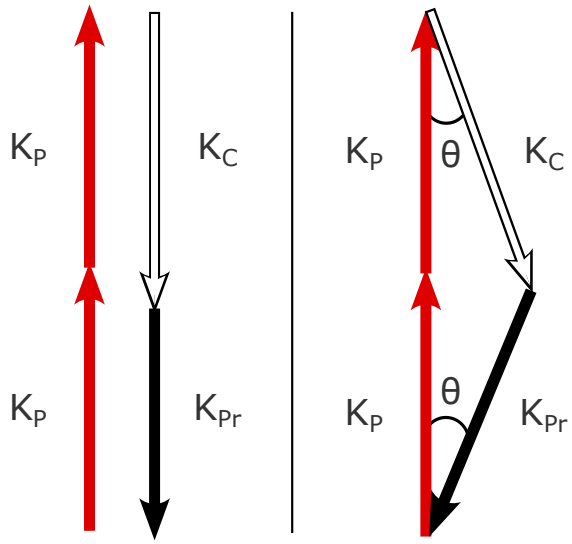


Figure 1.6: A geometric representation of the phase matching condition. This is shown for two cases; in the vacuum (left) and in a resonant media (right). The wave-vectors of the: probe, conjugate and pump beams are represented by: $K_{Pr} = n_{Pr}k_{Pr}$, $K_C = n_C k_C$ and $K_P = n_P k_P$ respectively. [43]

a refractive index significantly far from 1. This is because they're close to the resonant frequency of an atomic transition. [44, 43]

In this specific system, this is true for the probe beam only, as each beam is at a different frequency and thus experiences a different n. Here $n_{Pr} \approx 1+(5\times10^{-7})$, so $K_{Pr} = n_{Pr}k_{Pr}$ is somewhat larger than it otherwise would be. The result of this is that the beams must now be at an angle to each other, θ (typically 0.7 mrad), to satisfy the phase matching condition. Further, the angle of both the probe and conjugate beams is almost the same, due to the conservation of momentum as projected along the transverse direction. This is shown on the right-hand side of figure 1.6. Additionally, this allows spatial separation of the beams in practice.

1.2.4 Polarisation

One method for isolating the probe and conjugate beams from the pump comes from exploiting the nature of polarisation, and its capacity to affect how momentum is exchanged between the light fields and the atoms being influenced by them.

Introduction to the Polarisation Vector

In free space the electric field of an EM wave may oscillate in the two orthogonal directions perpendicular to waves direction of travel, $\overline{x}$ and $\overline{y}$. Further, within a medium, it may oscillate in the direction of travel too, $\overline{z}$. At a fixed frequency, these orthogonal oscillations may be out of phase with each other and have different magnitudes, so the easiest way to track them is to express each of them as a complex number which forms a complex amplitude vector (a polarisation vector). For convenience, the basis for this is typically chosen to be spherical, in accordance with the spin projections of the photon in our chosen quantisation axis. In this case, $\overline{x}$ is chosen as the quantisation axis so the spherical basis is defined as

$$\sigma^{\pm} = \frac{1}{\sqrt{2}}(\overline{y} \pm i\overline{z}), \tag{1.91}$$

and

$$\pi = \overline{x}. \tag{1.92}$$

It is important to note that, in this quantization axis, the component of angular momentum along $\overline{x}$ carried by π, σ^+ and σ^- light is 0, $\hbar$ and $-\hbar$ respectively. Though, from this point, we will disregard their units and simply call them 0, +1 and -1.

Probe and Conjugate Isolation

The probe and conjugate beams are isolated from the pump beam by restricting the three input fields to one of two orthogonal linear polarisations. In this case, all the fields are propagating in the positive $\overline{z}$ direction, and the degenerate pump fields are made to be linearly polarised in the $\overline{y}$ direction. Whilst the probe seed field is linearly polarised in the $\overline{x}$ direction. We can use equation 1.91 to show that $\overline{y}$ polarisation of the pump can be expressed as

$$\overline{y} = \frac{1}{\sqrt{2}}(\sigma^+ + \sigma^-), \tag{1.93}$$

from the point of view of the atoms. As such, the π polarised probe will have no impact on the m_f state of the atom it is interacting with; whereas the $\overline{y}$ polarised pump will move the electron to a superposition of the $m'_f = m_f \mp 1$ states. This is according to standard selection rules that reflect the conservation of angular momentum.

Taking the momentum exchanges allowed, a simplified version of the 4WM process can be drawn in the $\overline{x}$ quantization axis. This is shown in figure 1.7. Each level represents an orthogonal magnetic state that may be made of a superposition of m_f levels, where the standard selection rules still hold. Figure 1.7 highlights how these orthogonal polarised pump and probe beams lead to a conjugate polarised in the same direction as the probe. Assuming the electron starts in the middle magnetic state of the lower energy level it will be excited by the pump field into a superposition of the outer two magnetic states in the upper energy level. From here, the π polarised probe causes the electron to drop into a superposition of the outer two magnetic states in the lower energy level. The pump then excites the electron into the middle magnetic state of the upper energy level. In order for this process to be both four levelled and parametric, the electron must return to its initial state, the middle magnetic state of the lower energy level. In doing so, it will generate a conjugate photon and only a π transition is possible. Hence, the conjugate

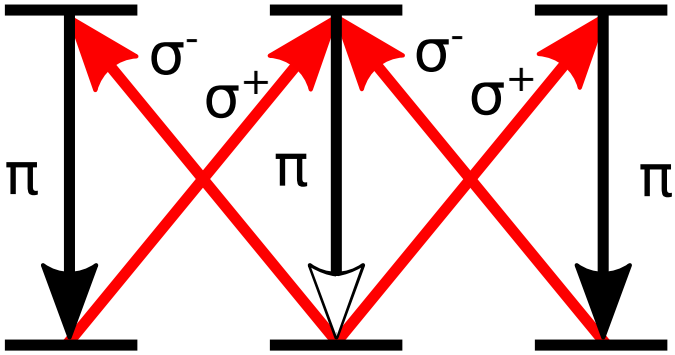


Figure 1.7: A simplified diagram of he 4WM process. Red arrows represent pump transitions, while black and white lines symbolize probe and conjugate transitions. It's important to note that the position probe and conjugate transitions can be effectively interchanged.

photons are generated π polarised.

The implication of these limited input polarisations on the output field can be further shown by analysing equation 1.87. If it is assumed that the three input fields are prepared such that there are two $\overline{y}$ polarised pumps (P) and one $\overline{x}$ polarised probe (Pr) that are perfectly linearly polarised and orthogonal in their polarisation to one another and assuming that they interact in the order $P \rightarrow -Pr \rightarrow P$ to produce a conjugate field. It can be seen that

$$\mathrm{P}_i(\omega_C) = \epsilon_0 \sum_{jkl} T_{ijkl} \chi^{(3)}(\omega_C; \omega_P, -\omega_{Pr}, \omega_P)' E_y(\omega_P) E_x(-\omega_{Pr}) E_y(\omega_P). \tag{1.94}$$

The limitations on T_{ijkl} shown in equation 1.88 then reduce this further to

$$P_x(\omega_C) = \epsilon_0 \chi^{(3)}(\omega_C; \omega_P, -\omega_{Pr}, \omega_P)' E_y(\omega_P) E_x(-\omega_{Pr}) E_y(\omega_P) \ , \tag{1.95}$$

$$P_y(\omega_C) = 0 \ , \tag{1.96}$$

and

$$P_z(\omega_C) = 0. \tag{1.97}$$

This indicates that the outgoing conjugate beam will be polarised in the same direction as the probe. By a similar argument, it can be shown that the reverse process (where the order of interaction is $P \rightarrow -C \rightarrow P$) will produce a probe field of the same polarisation too. Thus, it can be seen that if these two process act alone, they will feed each other, producing a gain in both the probe and conjugate beams. The fact they share the same polarisation, that is orthogonal to the pump, allows for their isolation for imaging. This is usually done using a Glan Taylor polariser.

Another benefit of limiting the polarisations of the input fields and thus output fields is that it overall reduces the complexity of the system. Despite this, however, a great deal of complexity still lies in the possible combinations of the input terms.

Some cases, for example $\omega_{3P} = \omega_P + \omega_P + \omega_P$ (frequency tripling), are made extremely unlikely due to the accessible energy levels of the system not accommodating the transitions necessary. This reduces the number of possible interactions even further. Thus, usually, only the 4WM interaction present in figure 1.2.2 has a high efficiency.

1.3 A Model of Squeezing in this System

To expand on this and see how the probe and conjugate beams grow and propagate in a real system, such as the double lambda scheme previously discussed, a semi-classical model of the beam propagation can be constructed. Further, this motivates the construction of a squeezing operator for this specific 4WM system, explaining how it leads to squeezed state generation. After, the dynamics of the model are explored to determine the optimum experimental parameters to form a squeezed state.

1.3.1 A semi-classical model of 4WM

First, it is assumed that both pump photons in a 4WM cycle come from the same field, the coupling strengths of the pump to both transitions are equal, and the probe and conjugate fields are comparatively weak.

Next, we consider the wave equation for a nonlinear optical medium, given previously as equation 1.82 under the assumption that the beams primarily propagate in the z direction and x dependence is brought into the envelope by setting $E_i(r,t) = \varepsilon_i(x,z)$. This results in

$$\frac{\partial^2 \varepsilon_i(x,z)}{\partial x^2} + 2ik_i \frac{\partial \varepsilon_i(x,z)}{\partial z} = \frac{1}{\epsilon_0 c^2} \frac{\partial^2 P(r,t)}{^2} e^{-ik_i z} e^{-i\omega_i t}. \tag{1.98}$$

The y direction is ignored because it is assumed that the beams are only angled in the x direction and the symmetry in the y direction will preclude any significant effects on the propagation.

Now we consider, from [45], that the polarisation for the probe and conjugate beams are

$$P_{Pr}(r,t) = (\epsilon_0 \chi_{PrPr} \varepsilon_{Pr}(x,z) e^{ik_{Pr}z} + \epsilon_0 \chi_{PrC} \varepsilon_C^*(x,z) e^{ik_{Pr}z}) e^{i\omega_{Pr}t} \tag{1.99}$$

and

$$P_C(r,t) = (\epsilon_0 \chi_{CC} \varepsilon_C(x,z) e^{ik_C z} + \epsilon_0 \chi_{CPr} \varepsilon_{Pr}^*(x,z) e^{ik_C z}) e^{i\omega_C t}, \tag{1.100}$$

when the electric field is expressed as it is in equation 1.98 and $2k_0 - k_{Pr} = k_C$ has been used to simplify. χ_{PrPr}, χ_{CC}, χ_{PrC} and χ_{CPr} are atomic susceptibilities where χ_{PrPr} and χ_{CC} are direct susceptibilities and χ_{PrC} and χ_{CPr} are cross susceptibilities.

These can be substituted into equation 1.98. This will produce

$$\frac{\partial^2 \varepsilon_{Pr}(x,z)}{\partial z^2} + 2ik_{Pr} \frac{\partial \varepsilon_{Pr}(x,z)}{\partial z} = -k_p^2 \chi_{PrPr} \varepsilon_{Pr}(x,z) - k_{Pr}^2 \chi_{PrC} \varepsilon_C^*(x,z) \tag{1.101}$$

and

$$\frac{\partial^2 \varepsilon_C^*(x,z)}{\partial z^2} - 2ik_C \frac{\partial \varepsilon_C^*(x,z)}{\partial z} = -k_C^2 \chi_{CC}^* \varepsilon_C^*(x,z) - k_C^2 \chi_{CPr} \varepsilon_{Pr}(x,z) \tag{1.102}$$

These can be solved to find the nature of the probe and conjugate propagation through the cell, as they are in chapter 5.

The dynamics of solutions to these depend on the values of the susceptibilities at the chosen tuning. However, the cross terms are generally responsible for the gain and level of squeezing of the two mode state, while the direct terms are responsible for the absorption of the fields.

The susceptibility terms are calculated by solving the density matrix for the 4WM process [45].

1.3.2 Relating this to the experimental system

Inspiration from the semi-classical model can be used to construct a more relevant squeezing operator, rather than relying on a more arbitrary mathematical construction.

This is done by interrogating the Hamiltonian of the 4WM process. This is given by

$$\hat{H}_{4WM} = \hbar\omega_P \hat{P}^\dagger \hat{P} + \hbar\omega_{Pr} \hat{Pr}^\dagger \hat{Pr} + \hbar\omega_C \hat{C}^\dagger \hat{C} + i\hbar\chi^{(3)}[\hat{P}^\dagger \hat{Pr} \hat{P}^\dagger \hat{C} - \hat{Pr}^\dagger \hat{P} \hat{C}^\dagger \hat{P}], \tag{1.103}$$

where $\hat{P}^\dagger$, $\hat{Pr}^\dagger$ and $\hat{C}^\dagger$ are the creation operators of the pump, probe, and conjugate beams respectively, and $\chi^{(3)}$ is the third order nonlinear electrical susceptibility of the system. This Hamiltonian expresses the energy of each of the fields involved in the interaction, as well as the cross coupling between them, as presented in the semi-classical model above. As such, the first three terms of this expression come from the energy of each of the beams, where they are modelled as QSHOs, and the last term is the energy

due to the conversion of the pump into the probe and conjugate beams.

This expression is simplified by using the low pump depletion approximation, wherein a large coherent state is assumed to behave like a classical field of constant amplitude. That is to say that we consider the pump field to have a constant number of photons and thus its energy is constant and can be disregarded [46, 30]. The pump is also assumed to be in the coherent state and thus approximate its creation and annihilation operators as

$$\hat{P}^\dagger = \rho^* e^{i\omega_P t} \tag{1.104}$$

and

$$\hat{P} = \rho e^{i\omega_P t}. \tag{1.105}$$

Where ρ is the classical amplitude of the pump field. This results in a more manageable expression, given by

$$\hat{H} = E_P + \hbar\omega_{Pr}\hat{Pr}^\dagger\hat{Pr} + \hbar\omega_C\hat{C}^\dagger\hat{C} + i\hbar\chi^{(3)}[\hat{Pr}\hat{C}\rho^{*2}e^{2i\omega_P t} - \hat{Pr}^\dagger\hat{C}^\dagger\rho^2 e^{-2i\omega_P t}]. \tag{1.106}$$

Where E_P is the energy of the pump.

Assuming the probe and conjugate frequencies are roughly equal this can now be converted to its interaction picture form, where the hamiltonian is considered in a rotating frame at this shared frequency. This produces [30, 47]

$$\hat{H}_1(t) = i\hbar\chi^{(3)}[\hat{Pr}\hat{C}\rho^{*2}e^{i(2\omega_P-\omega_{Pr}-\omega_C)t} - \hat{Pr}^\dagger\hat{C}^\dagger\rho^2 e^{-i(2\omega_P-\omega_{Pr}-\omega_C)t}]. \tag{1.107}$$

When $2\omega_P \neq \omega_{Pr}+\omega_C$ this expression is time-dependent, due to the oscillating exponential terms. These terms render the interaction Hamiltonian ineffective at producing twin photons, as the interaction will oscillate between producing and absorbing the photons. As such, effective probe and conjugate production occurs only when the exponent is al-

ways equal to zero. This can be interpreted as the result of the conservation of energy such that the frequencies are confined to $2\omega_P = \omega_{Pr} + \omega_C$. This produces a constant Hamiltonian given by

$$\hat{H}_1 = i\hbar\chi^{(3)}[\hat{P}r\hat{C}\rho^{*2} - \hat{P}r^{\dagger}\hat{C}^{\dagger}\rho^2]. \tag{1.108}$$

The time evolution of the system can be found, using the standard result for the time-evolution operator

$$\hat{U}(t) = e^{-(\frac{i\hat{H}}{\hbar})t}. \tag{1.109}$$

This produces

$$\hat{U}(t) = e^{i(\eta^*\hat{P}r\hat{C} - \eta\hat{P}r^{\dagger}\hat{C}^{\dagger})t}, \tag{1.110}$$

where $\eta = \rho^2\chi^{(3)}$.

$\hat{U}(t)$ is of the same form as the two mode squeezing operator shown in equation 1.68, where $\xi = \eta t$ and the general creation operators $\hat{a}^{\dagger}$ and $\hat{b}^{\dagger}$ are replaced with the more specific $\hat{P}r^{\dagger}$ and $\hat{C}^{\dagger}$.

Thus, a rigorous mathematical framework has been developed to describe the squeezing of 4WM.

1.3.3 Optimisation for Squeezing

Using the semi-classical model of 4WM, the susceptibility terms can be explored regarding changing system parameters. From this regions optimal for squeezing can be found. Ideally, the system would behave as similarly to the two mode optical amplifier as possible, since this would be the pinnacle of squeezed state generation. As such, the direct terms (χ_{PrPr} and χ_{CC}) would ideally be reduced as much as possible, allowing the cross terms (χ_{PrC} and χ_{CPr}) to reign.

A series of plots were produced using Python code adapted from that used to produce

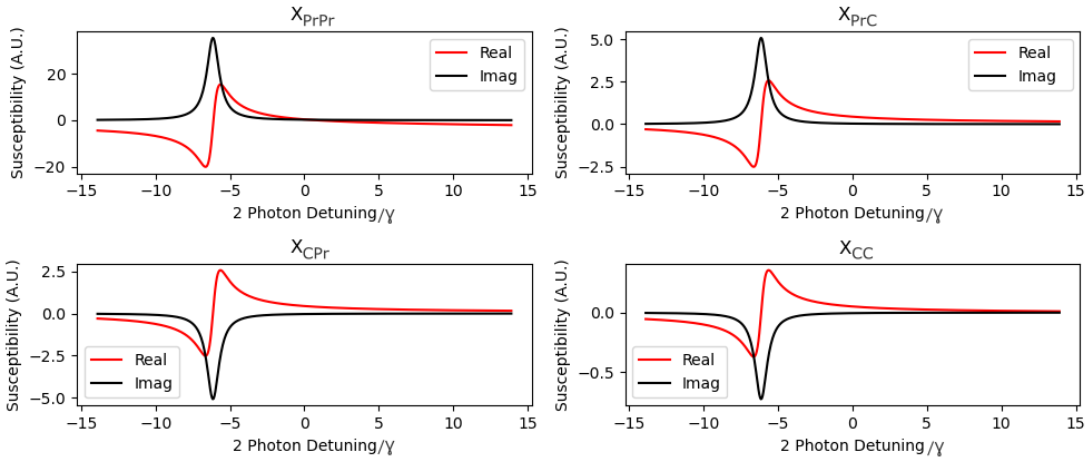


Figure 1.8: The Direct and Cross susceptibilities for the lower 4WM resonance, over the two-photon detuning. In this case, the one-photon detuning is normalised to the line width of the excited state ($\gamma = 2\pi \times 6MHz$) and was 80 and the pump intensity was $12MWm^{-2}$.

the graphs in Turnbull et.al. [45].

The two photon detuning is varied in the experiment by altering the probe frequency. Each component of the complex susceptibility is plotted in figure 1.8 as a function of the two photon detuning at typical experimental parameters.

The direct susceptibilities can be interpreted as effective linear susceptibilities for the probe and conjugate fields, such that the real part acts as a refractive index whilst the imaginary acts as an absorption term. It can be seen that the imaginary parts of the direct terms are at their maximum at the 4WM resonance, this is due to Raman absorption. However it is the largest for χ_{PrPr}, which would lead to significant absorption of the probe beam. Thus, this is not a good place to produce squeezed beams, as the majority of the effect will be lost.

However, the absorption term of χ_{PrPr} falls much faster than the magnitude of χ_{PrC} so there are regions on either side of the resonance that are optimal to observe squeezing. This is because, at these points, the cross terms are large enough to produce a large gain in the probe and conjugate fields and strong squeezing between them whilst the

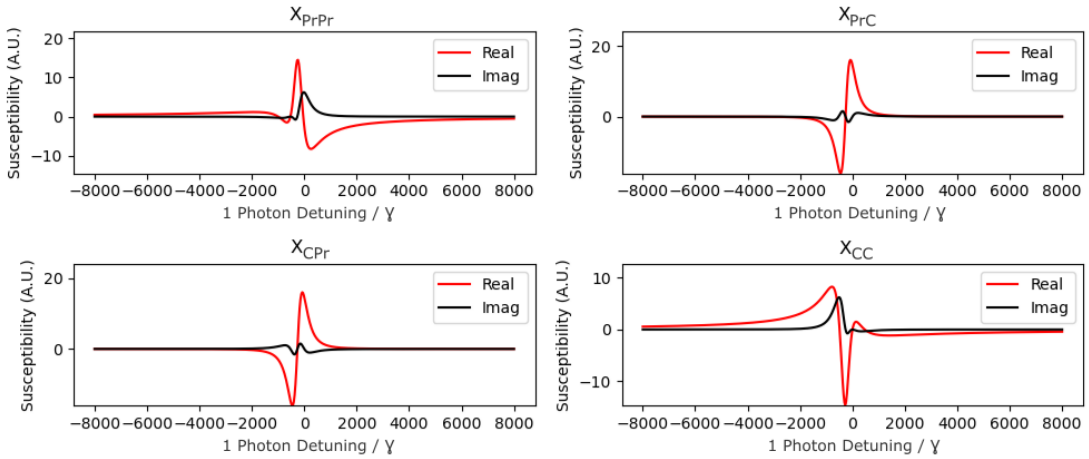


Figure 1.9: The Direct and Cross susceptibilities for the lower 4WM resonance, against the one-photon detuning. In this case, the two-photon detuning is normalised to the line width of the excited state ($\gamma = 2\pi \times 6MHz$) and was 1.39 and the pump intensity was $12MWm^{-2}$.

imaginary part of the direct term, χ_{PrC}, is small enough that little squeezing is lost by absorption of the probe field. This is where the majority of the experiments in this thesis are done usually at approximately a $3044MHz$ detuning, which was an optimal point found empirically for the specific experimental set up in this thesis.

These considerations do not need to be made for the conjugate beam as it is much further detuned from resonance from the probe and the absorption can, like the refractive index, be neglected.

Next, the susceptibilities can be plotted as a function of the one-photon detuning, this is shown in figure 1.9. There are actually two 4WM resonances for this parameter, but only the one present at a lower one-photon detuning is pictured here. The lower resonance is almost exclusively used in experiments as there is a large fluorescence at the one at larger one-photon detuning which can add excess noise to squeezing experiments.

Here it can be seen that although the cross terms are roughly symmetric about their zero crossings, with regions of large magnitude on either side, the direct terms are not. In particular, the χ_{PrPr} has a large imaginary (absorption) component on the higher detuned

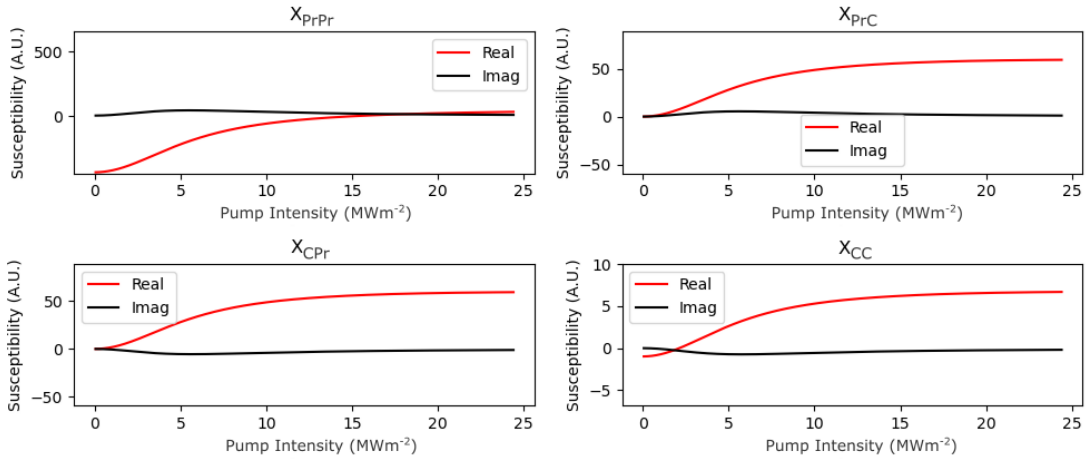


Figure 1.10: The Direct and Cross susceptibilities for the lower 4WM resonance, over various pump intensities. In this case, the one-photon detuning is normalised to the line width of the excited state and was 80, and the two-photon detuning is normalised to the line width of the excited state and is 1.39.

side. This is inconveniently overlaps the center of the region of the greatest probe gain and would greatly diminish squeezing for detuinings in this range. As such, in squeezing experiments, the detuning is usually placed just below the resonance in order to avoid the high absorption region whilst still retaining a large probe gain. This also aligns with an area of minimal conjugate absorption and maximal gain.

Finally, the susceptibilities can be plotted for various pump intensities. This is once again done for values of the other detunings typical of the experiment and shown in figure 1.10.

Here it can be seen that all the terms rapidly settle to a point where the absorption terms of χ_{PrPr} and χ_{CC} are minimal whilst the magnitudes of the cross terms saturate. In general, the experiment aims to be as close to this saturation point as possible, as it helps mitigate the effect of any noise inherent to the pump beam. Typically, the pump beam operates at power $1.5W$ and a beam waist of $1mm$, so the pump on average induces χ in the linear region with an intensity of $\sim 0.5MWmm^{-2}$. However, the Gaussian spatial profile of the pump means that the intensity is much higher near the centre of the beam

and the intensity does reach into the saturated region here. As such, the seed beam is typically focused at the pump centre to take advantage of this fact.

1.4 Multi Mode Squeezing

1.4.1 Multi Spatial Mode Squeezing

Until now, the 4WM process and squeezed state generation have only been considered in the single spatial mode case, where no attention has been paid to the transverse profile of the beams involved.

However, many of the applications of squeezed light require a multi spatial mode squeezed beam. Fields such as quantum enhanced imaging, nonlinear interferometry, and quantum plasmonic sensing particularly benefit from such light sources. [48, 49, 50, 51, 52]

In fact, strongly squeezed multi spatial mode beams can be generated by the process investigated in this thesis, 4WM in Rb vapour. This has been demonstrated previously, via homodyne detection techniques [53]. This is possible because atomic vapours are such high gain media, they do not require the use of a cavity for sufficient gain. The use of some types of cavity would preclude multi spatial mode squeezed state generation, since they would select only certain transverse modes to be amplified [54, 55]. However, multi spatial mode squeezing has been predicted and shown using confocal cavities, but at the expense of severely reducing the nonlinear coupling and gain of the system [56, 57].

An intuitive understanding of this in the near field can be found by considering a series of spatially separated 4WM interactions on a large pump beam, as outlined in the near field plane (NF) in figure 1.11. In this case, the pump is assumed to be so broad that all transverse points are exposed to the same pump intensity. It is also assumed that the

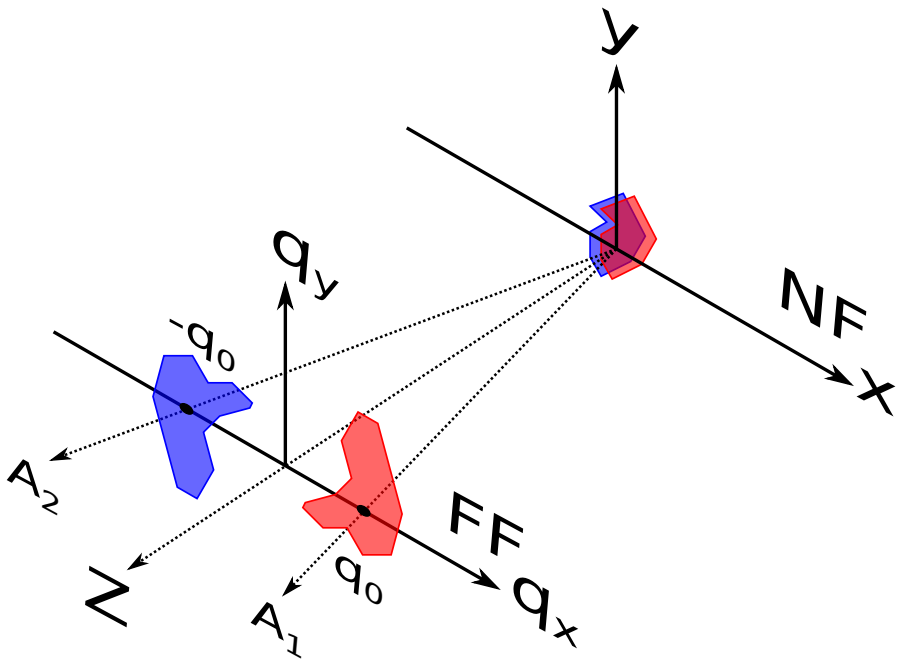


Figure 1.11: A diagram of the geometry of the localised squeezing in the near field plane (NF) and the far field plane (FF). x and y are the transverse spatial positions in the NF, and q_x and q_y are transverse positions in the FF. z is the propagation distance of the beams. In the NF ($z = 0$), photons are created pairwise in distinct locations, so small regions of the beams will be correlated. In the FF ($z = \infty$) the correlated modes have a z-axial symmetry imposed by the phase-matching condition.

cell is infinitesimally thin such that all interactions occur on a single transverse plane – the plane of interaction. At the plane of interaction, which is considered the near field, the generated photons have no time to propagate. Correlated photons will be generated pair wise in distinct locations. Therefore, small regions of the near field beams will have correlated photon statistics and not just the whole beam. Hence, the squeezing is multi spacial mode. However, this story changes when considering the far field (FF), where photons now have time to propagate beyond the plane of interaction and their diffraction must be considered.

In the Fraunhofer diffraction limit, when the beams are propagated infinitely far, the transverse distribution of the electric fields will be the Fourier transform of the transverse

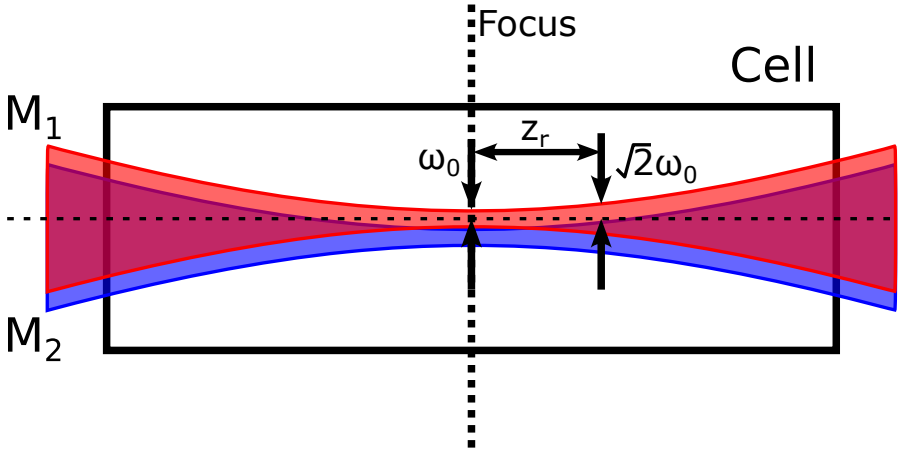


Figure 1.12: A representation of the cross coupling process, the light regions denote two spatial modes, M_1 and M_2, whereas the dark region represents where they overlap. In the medium, this results in cross coupling between the modes (overlapping outside the medium is irrelevant, as it does not produce any interaction). The Rayleigh length is shown just for M_1.

distribution of the NF electric fields. This property results in the quantum correlations now being axially symmetric about the pump propagation axis z, instead of being in the same position in each beam as in the NF case. This is further detailed in Embrey et al. and shown in the FF plane of figure 1.11 [20].

1.4.2 The Coherence Area

Earlier, it was assumed that all 4WM interactions occur on an infinitely thin plane. In practise, this is not the case. The squeezing process actually happens longitudinally over an extended medium, not just a single plane.

The beams will diverge as they travel through the cell. This will lead to the beams increasing in size, but can also lead to overlapping of the squeezed modes within them. The reasoning of this can be seen by imagining each of the beams to be made of many smaller Gaussian modes. These small Gaussians will also diffract, producing wider Gaussians

that will overlap with one another. This is shown for two modes, M_1 and M_2, of just one of the beams in figure 1.12. Here it can be seen that, in the centre of the cell (dashed line), the modes are completely separate, but they overlap elsewhere in the cell. 4WM interactions will still happen when they are overlapped, resulting in the modes being cross coupled and effectively expanding the size of the area of the localised squeezing.
The coherence area is defined as the area below which squeezing can no longer be measured, due to the aforementioned diffraction effects [58]. A general way to estimate this can be derived by considering the packing of Gaussian modes within the gain medium. The coherence width can be defined as the size of a mode waist, situated in the centre of the gain medium, which will expand to be $\sqrt{2}$ times larger at the ends of the medium. Modes this size and smaller are cross-coupled by the gain medium to the point that they do not support squeezing. This is the same expansion as seen in the Rayleigh range, $Z_r = \frac{\pi\omega_0^2 n}{\lambda}$ where ω_0 is the waist of the Gaussian mode and n is the refractive index at the wavelength λ of the mode. [59] As such, the coherence width, W, can be seen as the waist size of a Gaussian mode with a Rayleigh range equal to the length of the gain medium, l_c. This results in

$$W = \sqrt{\frac{\lambda l_c}{\pi n}}. \tag{1.111}$$

This gives an estimate of the minimum size of the regions where sub shot noise would be expected, caused by squeezing.

1.4.3 Squeezing Bandwidth

Beyond just spatial considerations, it is important to note the temporally multimode nature of this source too. The two-mode state is squeezed over a range of frequencies and importantly, a portion of the intensity difference squeezing occurs in a regime accessible by current electronics, making it useful for many applications.

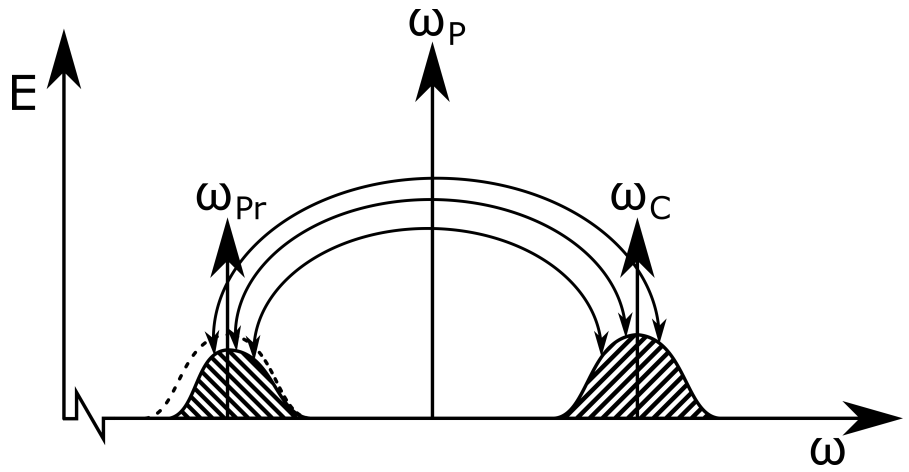


Figure 1.13: A diagram of a seeded 4WM process in the frequency domain. The widths of the emissions about ω_{Pr} and ω_C are approximately $20MHz$ (shown in diagonal hatch). This is the squeezing bandwidth, which is determined by the range of frequencies that the 4WM process is efficient over.

Figure 1.13 displays the form of a typical emission spectrum for a probe seeded 4WM amplifier. The initial seed is at a frequency ω_{Pr} and is amplified, causing the production of a strong conjugate at frequency ω_C, which is amplified from an initial vacuum state. However, vacuum modes around these frequencies are also amplified due to the amplification of spontaneously emitted probe and conjugate photons, shown as diagonal hatch in the figure. This is often referred to as 4WM fluorescence. These modes are populated by a random process and can be seen as the source of noise on the probe and conjugate beams. Due to the nature of the 4WM process, these distributions are correlated, as denoted on the diagram with curved arrows. Notice also that the distribution around the probe is not the same as the distribution about the conjugate. This is due to absorption effects on the probe.

To see why this emission distribution results in low frequency high-bandwidth squeezing, consider that the probe distribution can be expressed as

$$E_{Pr} = E(\omega_{Pr}) + \int_{-\infty}^{\infty} \varepsilon_{Pr}(\omega) d\omega, \tag{1.112}$$

where $E(\omega_{Pr}) = E_{Pr}(e^{i\omega_{Pr}t} + e^{-i\omega_{Pr}t})$ is the electric field at the seeded frequency and $\varepsilon(\omega) = E_s(\omega)(e^{i\omega t} + e^{-i\omega t})$ is the field at all other frequencies ($\varepsilon_{Pr}(\omega = \omega_{Pr}) = 0$) and E_{Pr} and $E_s(\omega)$ are the complex amplitudes of the fields in question.
This is squared to determine the intensity of the probe resulting in

$$I_{Pr} = E^2(\omega_{Pr}) + 2\int_{-\infty}^{\infty} E(\omega_{Pr})\varepsilon_{Pr}(\omega)d\omega, \tag{1.113}$$

where what would have been the final term has been neglected since it is minuscule relative to the others. Thus, it is omitted from equation 1.113.
The result of the multiplication in the second term will be

$$I_{Pr} = E_{Pr}E_s(\omega)(e^{i(\omega_{Pr}-\omega)t} + e^{i(\omega_{Pr}-\omega)t} + c.c), \tag{1.114}$$

which represents two noise distributions, one centred at $\omega_{Pr} + \omega$ and another at $\omega_{Pr} - \omega$. The former oscillates too quickly for modern electronics to measure and will be disregarded from hereon. The latter represents a distribution from DC to around $10Mhz$.
By the same argument, the conjugate intensity is found to be

$$I_C = E^2(\omega_C) + 2\int_{-\infty}^{\infty} E(\omega_C)\varepsilon_C(\omega)d\omega \tag{1.115}$$

and the resulting noise distributions will be similar too. The intensity difference between the beams is simply

$$I_{Pr} - I_C = E^2(\omega_{Pr}) - E^2(\omega_C) + 2\int_{-\infty}^{\infty} E(\omega_{Pr})\varepsilon_{Pr}(\omega)d\omega - 2\int_{-\infty}^{\infty} E(\omega_C)\varepsilon_C(\omega)d\omega. \tag{1.116}$$

As iterated, the final terms, which represent the noise on the state, in equation 1.116 will be correlated. Therefore, the intensity noise they represent will be reduced by their subtraction. Since these are distributed over a range of frequencies close to 0 there is

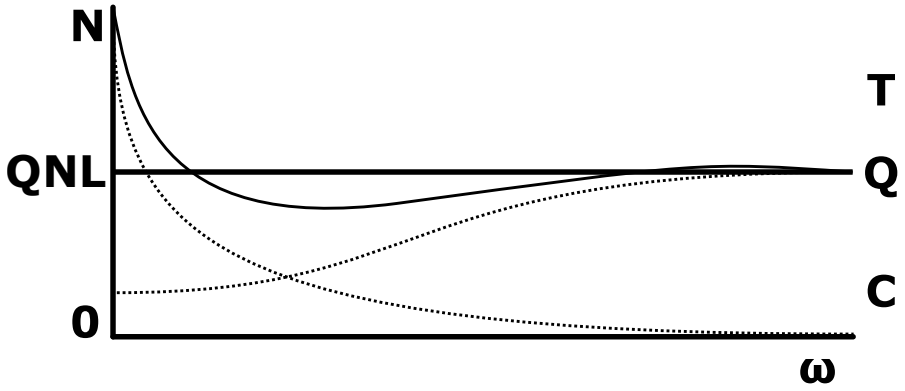


Figure 1.14: A representation of the classical (C), quantum (Q), and total (T) noise of the squeezed state in frequency space. The quantum noise begins at its minimum below the quantum noise limit (QNL). However, the total noise is kept above the QNL at low frequencies by the classical noise, which has a $\frac{1}{\omega}$ dependence.

squeezing over their bandwidth. This is represented as line Q in figure 1.14. The upper limit on this squeezing bandwidth comes from the frequency range over which the 4WM process is efficient [20]. Practically, however, the total noise, T, is kept above the quantum noise limit at low frequencies due to classical noise, C, which has a $\frac{1}{\omega}$ dependence.

1.5 Potential Measurements That Can Be Made With A Multi-spatial-mode Intensity Difference Squeezed Light Source

Now a theoretical understanding of this intensity difference squeezed light source has been developed, some useful applications of these states can be discussed.

Considering intensity difference squeezing between the total beam intensity, the SNR can be enhanced for a variety of measurements. In fact, the demodulation of a signal on the probe field amplitude that was of a magnitude lower than the quantum noise limit has already been realised [60]. Such technology could be employed in many applications,

with a notable example being the improving of the sensitivity of microcantilever position measurements in atomic force microscopy, thus increasing the overall sensitivity of the instrument [61]. Another exciting application is in improving membrane position sensing for use in other sensors, such as in gravitational wave detectors or micro-electromechanical systems based force microscopes. One group has achieved a sensitivity of $200am/\sqrt{Hz}$. [62]

Further applications can be found that take advantage of the multi-spatial mode nature of this squeezed light source. Specifically, applications of the near field beams are considered here, since investigating these are the type employed in this thesis. The pinnacle of these would be the realisation of quantum imaging using this MSM squeezed state. Here intensity difference imaging can be achieved by passing the probe beam through a weekly absorbing sample and projecting it onto an image sensor while the conjugate is projected onto an image sensor as well. Regions of the beams, larger than the coherence area, could then be subtracted from each other and an intensity squeezed image would be formed. Such a development would pave the way to the development of a true 'quantum microscope' allowing the imaging of features that would otherwise be lost in the noise in other systems. Such a system would be particularly useful in cases where the SNR cannot be increased by simply increasing the power of the sampling light, such as when the sample being measured would be damaged by too high of a photon flux. These conditions are common in the field of biomedical imaging. Taking the first steps to overcome the barriers in the way of generating these quantum images will be the focus of the rest of this thesis.

CHAPTER 2

PRACTICAL REALISATION AND MEASUREMENT OF A TWO-MODE SQUEEZED STATE

THE theory of 4WM and how it is used to generate squeezed states has now been thoroughly covered. This coming chapter deals with the apparatus and engineering required to practically generate these squeezed states and measure them.

2.1 Experimental Apparatus

The pump and probe seed beams that power the 4WM originally start as a single coherent beam, generated by an M^2 SolsTiS ultra-narrow line width Ti:sapphire laser – with a typical output power of $3W$ [63, 64, 65]. This laser generates a beam with an absolute line-width $\leq 50kHz$. Such frequency precision is required as the resonance point for the 4WM being explored is very narrow, whilst significantly overlapping with a region

of high probe absorption. Any absorption in the 4WM process will greatly diminish the squeezing attainable.

To understand this properly, we turn to the model provided by Jasperse et. al. [66]. In this paper, the loss is modelled as a series of beam splitters with an empty port interleaved with squeezing gain stages. The splitters' output state is a combination of the input and vacuum modes, which couples the vacuum fluctuations onto the transmitted beam. They provide an equation for the noise figure, NF, or the ratio of the measured noise to the corresponding shot noise level for equal optical power for subtracted probe and conjugate beams generated by 4WM. This is

$$NF = 1 - \frac{2Ssinh^2\xi}{\xi cosh(2\xi + \Upsilon)} + \sqrt{T_{Pr}}\frac{S\log^2 T_{Pr} sinh^4\xi}{2\xi^3 cosh(2\xi + \Upsilon)}, \tag{2.1}$$

when the detection efficiency of the beams and the transmission of the conjugate are 100% [66]. These are valid approximations in the experiments undertaken in this thesis. The parameters ξ and Υ are given by $\xi = \frac{1}{4}\sqrt{16S^2 + \log^2 T_{Pr}}$ and $\tanh\Upsilon = \frac{\log T_{Pr}}{4\xi}$ respectively, where T_{Pr} is the probe transmission and $G = \cosh^2 S$ with G being the intrinsic gain of the 4WM process.

Any loss in a squeezed system can significantly affect the apparent squeezing, as is demonstrated in figure 2.1 which is a plot of equation 2.1 against T_{Pr} at $G = 3$ and conjugate transmission, T_c, equal to one. Although a small amount of probe absorption is predicted to improve the noise reduction slightly, this trend quickly reverses, with greater absorption quickly leading to significantly reduced squeezing. As such, a region of high absorption means there is only a very narrow parameter space where 4WM is significant enough to produce strongly squeezed beams without the probe absorption compromising them.

Furthermore, it is beneficial that both beams are sourced from the same laser, as any frequency drift will be identical for both of them. Thus, the detuning of one beam rel-

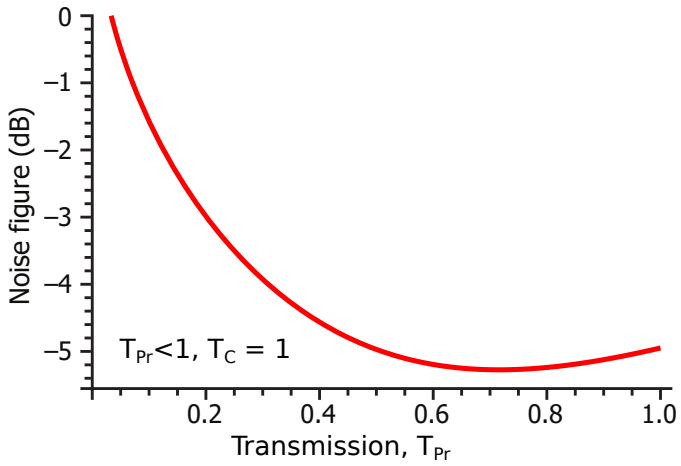


Figure 2.1: the predicted noise figure for 4WM with an intrinsic gain $G = 3$ and conjugate transmission T_C equal to one - Adapted from Jasperse et. al. [66].

ative to the other will remain constant. Classical intensity noise is also the same for both beams, making it easier to account for with just a single filtering stage [67]. This is common mode noise suppression.

Figure 2.2 shows that the source first passes through an $80MHz$ AOM. This component acts with a system discussed later to form a 'noise eater' active filter. This stage has a transmission efficiency of around 50%. As such, roughly $1.5W$ of power makes it to the rest of the system, aside from the $50mW$ of power used as the feedback signal. This is represented as the beam exiting at the bottom left of the diagram.

Next, the beams are split by a 50:50 beam splitter and one is passed through another 80MHz AOM then fed directly into the cell. This is the high-powered pump beam. Only the 1^{st} output order is propagated to the cell, so frequency shift of $80MHz$ occurs on the beam. The main function of this stage is to allow easy tuning of the pump power.

The various lenses along the pump beam's path, absent from figure 2.2, are used to adjust the size of the pump appropriately. The lenses before the AOM are used to focus the beam into the element for optimal efficiency. The lenses after are used to bring the pump to a wide focus ($2mm$ beam waist) in the centre of the Rubidium vapour cell, such

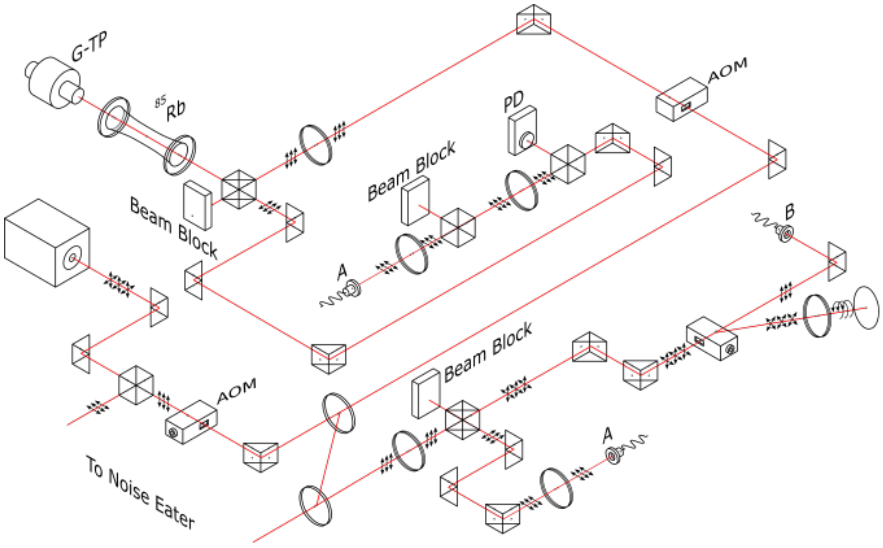


Figure 2.2: A Diagram of pre-cell beam preparation.

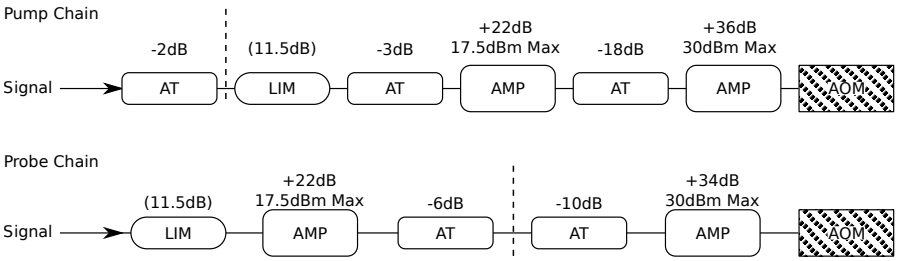


Figure 2.3: A diagram of the RF chain from the pump signal generator to the pump AOM transducer and the RF chain from the probe signal generator to the probe AOM transducer. The abbreviations AT, LIM, and AMP stand for attenuation, limiter, and amplifier respectively.

that it is much bigger than any incident seed beam. As such, the Gaussian profile of the pump is so wide that, from the perspective of the probe seed, it approximately resembles a plane wave. The validity of this approximation does not always hold, however.

The pump AOM itself is driven by an $80MHz$ RF wave, generated by a signal generator, that passes though the pump RF chain displayed in figure 2.3 before arriving at the AOM transducer.

The pump chain itself consists of two amplifiers ($+22dB$ and $+35dB$) that both typically

act in saturation to bring the output power up to $1W$, which will also bring the AOM to close to its peak transmission. This is of the form

$$\frac{I_1}{I_0} = aP_{RF}\text{sinc}^2(aP_{RF} + b)^{\frac{1}{2}}, \tag{2.2}$$

where I_1 and I_0 represent the diffracted and input light intensity, a and b are constants, and P_{RF} is the incident RF power on the AOM [68].

Saturation is useful for noise reduction as, when an amplifier operates in saturation, any variance on the power of the incoming RF wave has a minimal impact on the variance of the output of the amplifier. This is because the derivative of the amplification function would be small at this point. This is counter to an unsaturated amplifier, in which variance on the input would lead to significant variance on the output as the derivative of the amplification function is large. The difference between the unsaturated case, A, and the saturated case, B, is demonstrated in figure 2.4 [69].

In the case of the AOM, noise is also reduced. This is because, even though it does not saturate, the derivative of the transmission function, equation 2.2, is minimised at the point we operate at, its maximum transmission. This means the variance on the input leads to little variance on the output, for the same reasons outlined for the amplifiers.

Amplifier saturation is achieved by providing a $13dBm$ signal from the signal generator and is done to minimise the noise that is added onto the laser travelling through the AOM. In some experiments, the power from the signal generator was adjusted to change the pump intensity in the cell. The limiter is a protective element to prevent damage to the amplifiers and the dotted line behind it represents the point an RF switch was added when using the PIXIS camera, as discussed later.

The other beam is the probe seed, which is first sent through a 1.5GHz AOM in a double pass configuration and then injected into the cell at an angle, to meet the phase matching condition. This is done using a pair of mirrors before the cell. The frequency of this

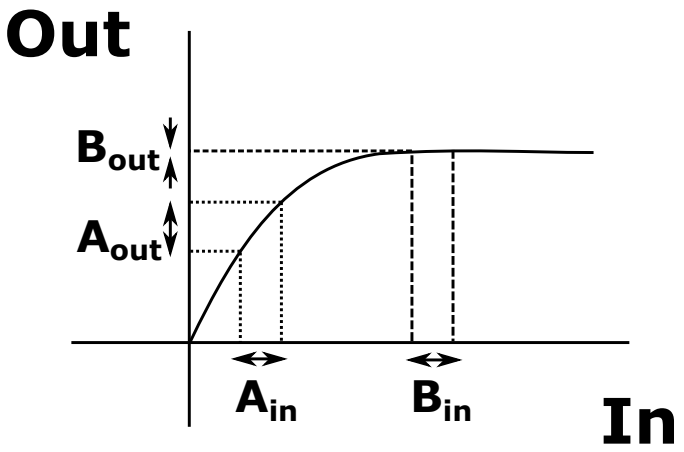


Figure 2.4: A diagram showing the difference between the unsaturated case, A, and the saturated case, B, for a generic amplifier. In the unsaturated case, the variance on the signal leads to significant variance on the output due to the large gradient in the transmission function, whereas, in the saturated case it does not, due to the shallow gradient in the transmission function.

beam can be adjusted using the AOM, as the 1^{st} order output mode is steered into the cell. The power of the probe seed is adjusted using a half-wave plate and a polarising beam splitter.

The 1.5GHz AOM is driven by a HP 8642M signal generator, typically at $1.48GHz$ to produce a double pass frequency shift of $2.96GHz$. The signal is generated at $20dBm$ and passed through the probe RF chain, shown in figure 2.3. The line between the attenuators represents the point an RF switch was added for use with the camera.

After the $1.5GHz$ AOM, the beam is passed through a polarisation maintaining fibre in order to clean the beam profile [70]. It then passes through a set of lenses that are used to shape the beam waist independently in the horizontal and vertical direction during the experiments.

The squeezed beams are generated inside the rubidium vapour cell via the 4WM process explained in the previous chapter. The cell itself is held in an assembly, as depicted in figure 2.5.

The cell assembly consists of an external vacuum chamber that the cell is held in the

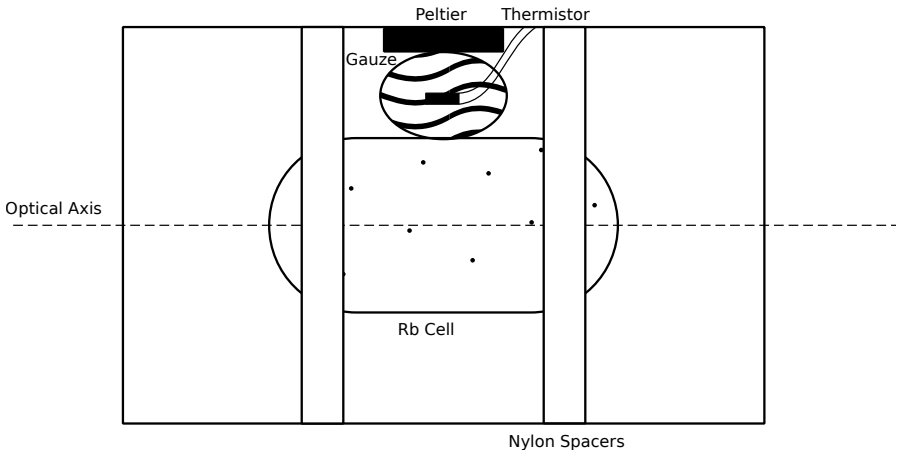


Figure 2.5: Depiction of the vacuum assembly that holds and regulates the temperature of the Rb cell, typically used ($\sim 110°C$).

middle of via the use of nylon spacers. A low vacuum is held to mitigate any beam disturbances due to air convection, as the cell is continuously heated. The heating itself is provided by a nichrome coil (not shown) and it is stabilised by a Peltier heater with a thermistor in a PID feedback loop. A metal gauze is used to conduct heat to or from a cold spot on the cell and for hosting the thermistor in good thermal contact with the cell.

The beams are then allowed to propagate out of the cell along with the pump before entering a Glan-Taylor Polariser. Since the pump beam is at an orthogonal polarisation to the probe and conjugate it can be removed and dumped on a beam block. However, a significant amount of fluorescence is generated in the cell at around the pump frequency. Since it is fluorescence, it is unpolarised and cannot be removed with the G-TP. Instead, a large portion of it is typically spatially filtered by the imaging system that comes afterwards, by a beam block placed in the centre of the focus of L1 shown in figure 2.6. However, not all of it can be removed, as some of it is emitted in the same direction as the probe and conjugate beams and indiscernible from them.

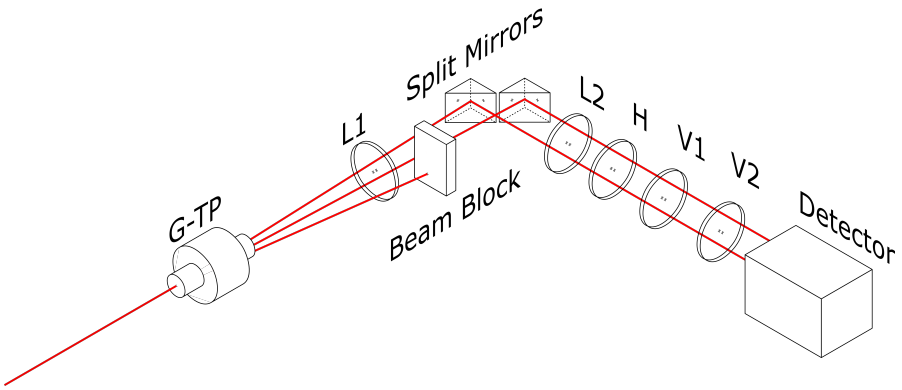


Figure 2.6: A diagram of the typical optical setup after the gain medium. L1, L2, H, V1, and V2 are imaging lenses used to focus the beams onto a detector for measurment.

2.2 Imaging the Beams

After the G-TP and spatial filtering stage, the apparatus consists of various optical elements for separating and imaging the correlated beams onto a detector, shown in figure 2.6.

After the beams pass through L1, the probe and conjugate are separated using split mirrors placed as close to the focal plane as possible, as the ratio of beam separation over beam size is maximised at this point. The beams are then imaged by another lens placed one focal length away (L2) – completing a 4F system. Angling of the split mirrors can be used to avoid the final beams being superimposed, as they are in the cell. In some imaging setups, another set of cylindrical lenses is used to further shape and expand the beams horizontally, H, and vertically, V1 and V2, for optimal imaging.

After this, the beams are separately focused onto the detector required in a given experiment using mirrors.

2.3 Measuring Squeezing: Instrumentation

After transport, the squeezing on the beams must be measured. This is achieved mainly by two instruments: the balanced photodetector and the PIXIS camera.

2.3.1 The Balanced Photodetector

The balanced photodetector used in this thesis is a homemade detector. It is constructed of two photodiodes connected such that the probe and conjugate can be shone onto them to generate opposing photocurrents. This subtracts the outputs from the two photodiodes, and the remaining current is amplified and converted to an output voltage by a transimpedance amplifier circuit [71].
This voltage output can then be connected to an oscilloscope and a spectrum analyser to evaluate the noise output as compared to two beams of coherent light of the same intensity.

2.3.2 The PIXIS-1024BR eXcelon Camera

The other way squeezing is measured is via the use of a high speed PIXIS-1024BR eXcelon Camera, running in kinetic mode. In this way, many images of the correlated beams can be taken in quick sequence for analysis.
A high rate of image acquisition is required, since low speed acquisition is susceptible to technical noise [72, 73, 74]. Noiseless digitisation is slow, however, so the CCD itself is used as a buffer whilst producing a rapid succession of images of the beams [75]. This is done by defining an imaging 'slice' of the CCD (in our case, a region 64x1024 pixels in size). Between shots, data in the imaging slice is shifted to the slice below it, so that a

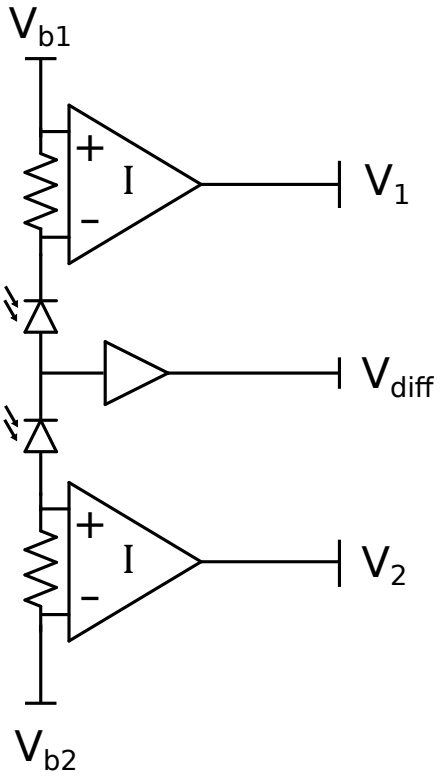


Figure 2.7: A circuit diagram of the BPD internals, the photo currents generated by the two photodiodes subtract at the junction between them and are converted to a voltage, V_{diff}, by a transimpedance amplifier. Resistors on either side of the photodiodes convert the small current they produce into a small voltage drop across them. This is amplified by two instrumentation amplifiers, I, to produce V_1 and V_2.

new image can be generated without superimposing with the previous one. The results of this process produce an entire 'frame' of data made of a series of sequential 'slices'. Digitally, this data is then split halfway along the x-axis, so we can obtain two sets of slices, one for the probe and one for the conjugate. An important point to note is that each pixel will be continuously receiving photons and building up charge, even while the data is being shifted. This would be a problem if the camera were continuously exposed to the beam, as it would lead to blurred images. This can be mitigated by redirecting the beams between shots, by pulsing RF power to the pump $80MHz$ and the probe $1.5GHz$ AOM only when taking an image of the beams. This was conveniently done by tying

both the camera and AOM frequency generator to the same trigger.

Some of the camera's specifications are included in the table 2.1 for reference. [76]

Table 2.1: Some of the PIXIS-1024BR eXcelon's specifications.

Imaging area	13.3 x 13.3 mm (optically centred)
CCD format	1024 x 1024 imaging pixels 100% fill
Vertical shift speed	3.2 to 18 $\mu sec/row(programmable)$
Dark current @ $-70°C$ (e-/p/sec)	0.02 (typical), 0.07 (max)
Quantum Efficiency @=$795nm$	99%
System Read Noise @ $100KHz$	3 e- rms (typical, 5 e- rms (max))
System Read Noise @ $2MHz$	9 e- rms (typical), 15 e- rms (max)

Most of the features of this camera make it very suitable for low noise imaging applications, as its exceptional quantum efficiency means very little squeezing is lost in the imaging process and the rapid maximum shift speed, $3.2\mu s$, allows for an entire frame of data to be taken in just $3.28ms$. This is especially true when it is run in kinetic mode, which allows sequential imaging at an even faster rate. The system read noise at $100KHz$ is about 3 electrons per pixel, which means it will be lower than the photon shot noise as long as more than 10 photons are detected per pixel. The actual readout frequency is closer to $300KHz$ but the noise level should be comparable at this point.

However, this method is not without its drawbacks. The main one being that the number of slices that can be taken is limited by the size of the CCD and the minimum slice size desired, this is usually around 64 pixels on the y-axis. As such, the maximum number of 64x1024 slices that can be achieved for is 16. The first 2 and last 2 slices are often overexposed and have to be removed from the analysis, reducing this to 12 per readout.

Part II:

Camera Imaging

CHAPTER 3

LOCALISED SQUEEZING

MULTI-spatial mode squeezed states were generated using the methods described in the previous chapter, and sampled using the PIXIS-1024BR eXcelon camera. Data obtained in this way was then analysed with a variety of algorithms, with the hopes of showing the multi-spatial mode character of the squeezing. The results of these algorithms are the focus of this chapter.

3.1 Set Up

Initially, the parameters of the system were set to the values that produced optimal squeezing over the power difference of the whole beams. Then, a post cell 4F imaging system was used to generate an image of the cell. A diagram of a 4F imaging system is shown in figure 3.1. It consists of two lenses separated by their focal lengths. The first lens (left) takes the input image from the object plane and forms an intermediate

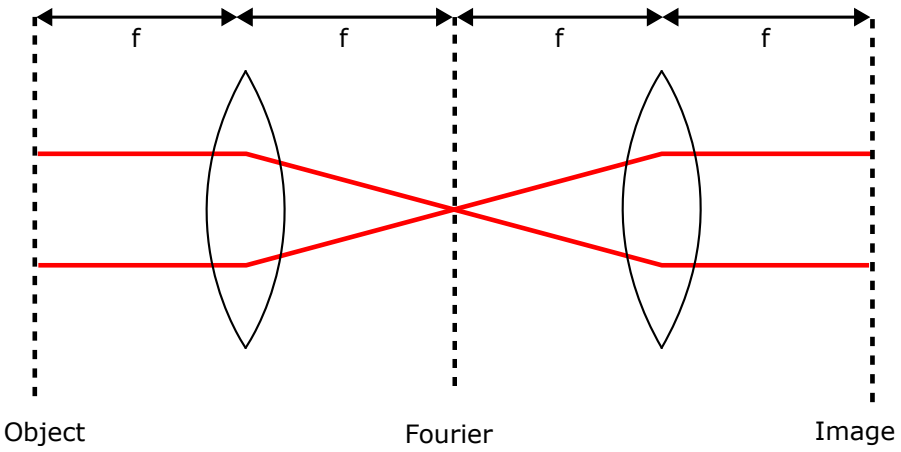


Figure 3.1: A diagrammatic representation of 4F imaging.

image at the Fourier plane. The Fourier plane represents spatial frequencies from the input image. The second lens (right) re-images the spatial frequencies from the first focal plane and forms a new image at the image plane.

The focal point of the 4F system was adjusted by moving the entire 4F system along the propagation axis and, in this case, placed in the centre of the cell. within the 4F system, a split mirror was used to separate the probe and conjugate beams.

The beams passed through the first lens, bringing them into the Fourier plane. Here, they were spatially separated, due to their different k vectors. This led to them having an approximate point symmetry about the pump axis. Thus, they could be individually steered using the split mirror. This resulted in them being separated in the imaging plane. This process is represented in 2.6. This allowed each beam to be individually imaged.

The beams were then magnified anisotropically, with an 8:1 horizontal to vertical ratio in the magnification factor, and imaged in the image plane by a PIXIS-1024BR eXcelon camera running in kinetic mode.

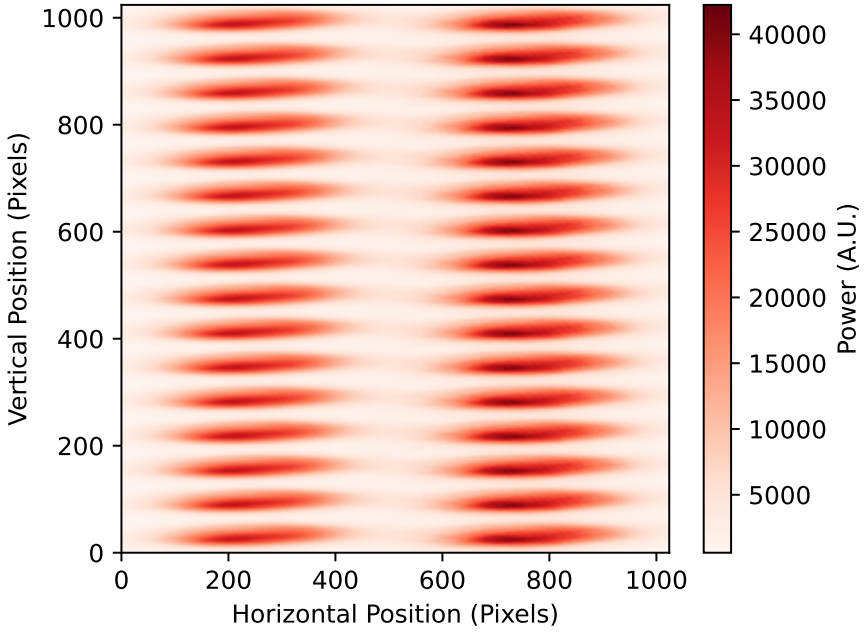


Figure 3.2: A single frame of data captured on the camera CCD.

3.1.1 Simple Subtraction

An example 'frame' of data collected by the camera is shown in figure 3.2. First, the data was split halfway along the x axis, and then a series of splits were taken on the y axis. This overall produced a set of 16 probe images and 16 corresponding conjugate ones too, the image index is given by s.

The corresponding images (same s) were added and subtracted from each other to combine them. In this analysis, the probe and conjugate images were subtracted assuming that the beams were already at optimum relative position, since their intensity distributions were most overlapped here. The mean intensity values of each pixel over the s axis, hence in the time domain, were then taken for both combinations of the beams. From here, the variance of the subtracted beams, σ_{-}^{2}, was calculated and divided by the mean

of the added beams, μ_+, producing the final result,

$$\sigma_N^2 = \frac{\sigma_-^2}{\mu_+}. \tag{3.1}$$

It is normalised in this way to allow a direct comparison with the Poisson noise on the system which would now have a value of 1 [77, 78]. This is because the variance on combined uncorrelated coherent beams can be given by μ_+^2, since the variance of is given by the mean intensity [79, 80, 81]. Thus, dividing by the mean of the added beams, should normalise to the shot noise and allow direct comparisons between regions of the beam of different intensities.

Intensity difference squeezing would be expected to reduce σ_N^2 below 1. This can be shown by considering that if two beams, Pr and C, are combined by subtraction then the output beam will have a noise corresponding to

$$\sigma_-^2 = \sigma_{Pr}^2 + \sigma_C^2 - 2Cov(Pr, C), \tag{3.2}$$

where σ_{Pr}^2 and σ_C^2 are the variances of the probe and conjugate beams and $Cov(Pr, C)$ is the covariance between them.

They will have a positive non-zero covariance if they are intensity difference squeezed, which will reduce the variance below that of the combined uncorrelated beams. Thus, the normalised value will be below unity.

It is important to note that, in this analysis, the sample size per each frame of data is statistically small as the number of consecutive images is limited to 16. It can be seen from [82] that the standard error on the sample variance is given by $\sigma'_{\sigma^2} = \sigma^2\sqrt{\frac{2}{n-1}}$ where σ^2 is the sample variance and n is the number of samples. Hence, for 16 images, the standard percentage error is still around 35%. However, this can be improved by averaging the results of several frames of data, as is done for some cases.

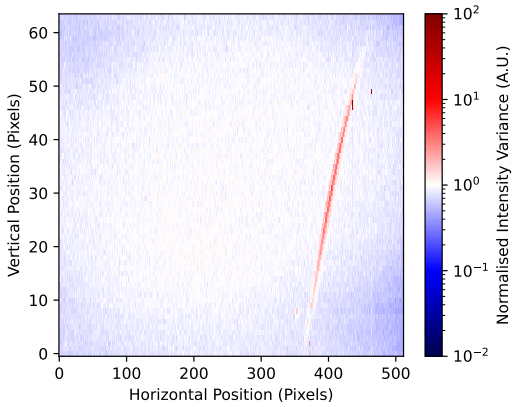


Figure 3.3: An image of the normalised variances on the pixels produced by the conjugate beam, averaged over 42 separate frames.

A plot of the normalised variance of the conjugate, averaged over all 42 slices, was then produced. This is shown in figure 3.3. The normalised variances are also represented in a logarithmic scale.

The normalised variances are mostly near 1. However, there is also a region of exceptionally high variance on the right side of the image. The fact that the high variance region was not removed by the averaging process indicates that the feature is highly variable in intensity but consistent in position. The cause of this systematic error has been localised to the camera's CCD. It is believed that it may be an artefact of how the CCD is attached to the frame of the camera. As it always maintains its position, and it produces high variance areas, it is unlikely to yield false positives in the search for intensity squeezing. As such, it is noted, but there was no need to explicitly compensate for it in the code or measurements.

After this baseline was established, the difference of the beams was taken. If the squeezed regions are in the same place in each beam, a general reduction of the normalised variance below 1 should be seen, hence, squeezing. Looking at figure 3.4 the results of can be seen.

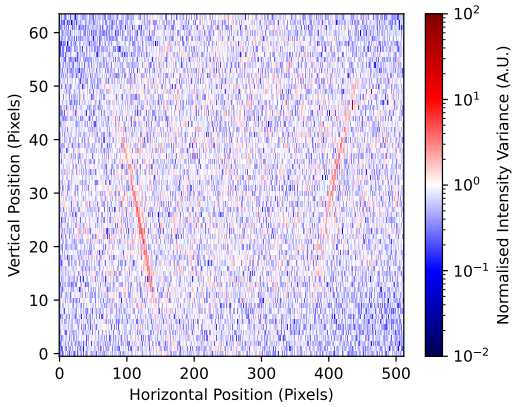


Figure 3.4: An image of the normalised variances on the subtracted beams ($Pr - C$). Both beams are centred at the centre of the image.

High variance features make an expected appearance again, the left line being caused by the probe image and the right one being caused by the conjugate image. The rest of the picture, however, is where the problem lies. Most of the picture shows normalised variances around 1. This can, in part, be explained by the fact that there are other sources of noise in the system keeping us above the shot floor. However, there are no large patches of intensity difference squeezing at all.

3.1.2 Fourier Analysis

To determine why squeezing was not visible, the data was analysed in the spatial frequency domain. As such, a frame of data was taken and the left side was subtracted from the right in the same way it was done during the previous section. This generated a series of potentially intensity squeezed images. A 2D Fourier transform was then taken from the result and the variance over time (s) for each frequency was calculated. Finally, the entire image was normalised, by dividing it by the average value of the left side added to the right side.

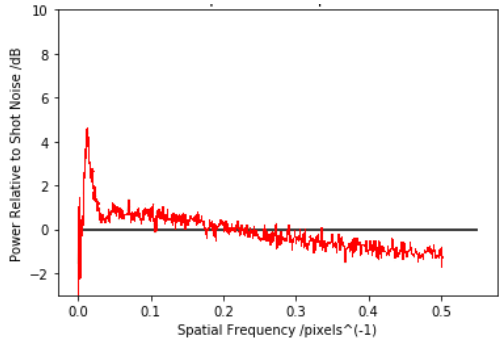


Figure 3.5: 1D Noise Profile in frequency space. The DC noise has been removed for scaling.

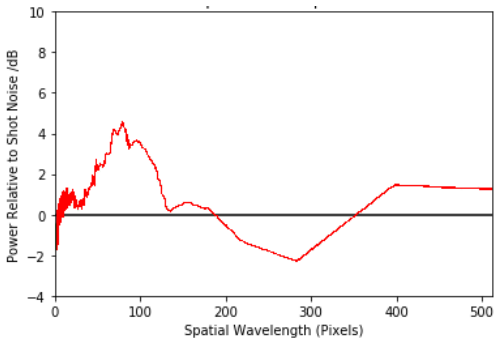


Figure 3.6: 1D Noise Profile against spatial wavelength. The DC noise has been removed for scaling.

An isotropic noise spectrum would be expected. Since, without any other effects, there should be no difference in the noise distributions along the horizontal and vertical axes. As such, the statistics on the measurements of this noise can be improved by averaging the points that share the same spatial frequency, $|k| = \sqrt{k_x^2 + k_y^2}$. This is effectively just averaging the results over a series of ellipses. This produced a $1D$ plot of noise versus spatial frequency or spatial wavelength (figures 3.5 and 3.6). The lengths of the semi-minor and semi-major axes of the ellipses were always in a 1 to 8 ratio to account for the anisotropy of magnification of the beams.

Looking at figure 3.5 a number of interesting features can be determined. First, a minimal squeezed region is seen at very low spatial frequencies. This is exciting, as it shows that the current set-up is capable of producing some level of squeezed image. This is quickly interrupted by a large peak in the noise. This analysis alone is not enough to determine the cause, however. After, the noise settles at a baseline slightly above shot noise.

Finally, the noise starts to drop into the sub-shot region. This effect is not caused by squeezing, though, rather by a 'pixel bleeding' effect where some voltage produced in one element bleeds into those around it. This produces some covariance between them and

artificially lowers the noise at high spatial frequency. However, the spatial wavelengths at which this becomes significant are much smaller than the coherence area of the 4WM process and we would never expect to see squeezing below this size anyway.

Figure 3.6 displays the same information, but against spatial wavelength as opposed to spatial frequency. Looking at both the noisy peak and the squeezed region, the noisy peak extends from around 20 to 100 pixels, whereas the squeezed region goes on from 100 to around 350. Beyond this, classical noise takes over, rendering any squeezing at higher wavelengths invisible. The range of the noise peak is similar to the predicted size of the coherence area, so it was thought that accounting for the coherence area before subtracting the beams would help to reveal the multi-spatial-mode squeezing.

3.1.3 Top-hat Subtraction

The simplest way to account for the coherence area would be to average the signals from neighbouring pixels, to effectively expand their collecting area to that of the coherence area. This does limit resolution of course, but the size of the coherence area already does this for the squeezing anyway.

This averaging was done by convolving the image data arrays, $Pr_{s,x,y}$ and $C_{s,x,y}$, with a square top hat kernel [83]. This can be represented for the probe or the conjugate as

$$Pr^{Cv}_{s,x,y}, C^{Cv}_{s,x,y} = \sum_{-\frac{m}{2}}^{\frac{m}{2}} \sum_{-\frac{n}{2}}^{\frac{n}{2}} Pr_{s,x+m,y+n}, C_{s,x+m,y+n}, \tag{3.3}$$

where m and n are the horizontal and vertical size of the top hat, in pixels. The method then proceeds as in section 3.1.1. Applying the method for the top-hat kernel sizes: 16 x 2 pixels, 32 x 4 pixels, 48 x 6, and 64 x 8 pixels is shown in figure 3.7.

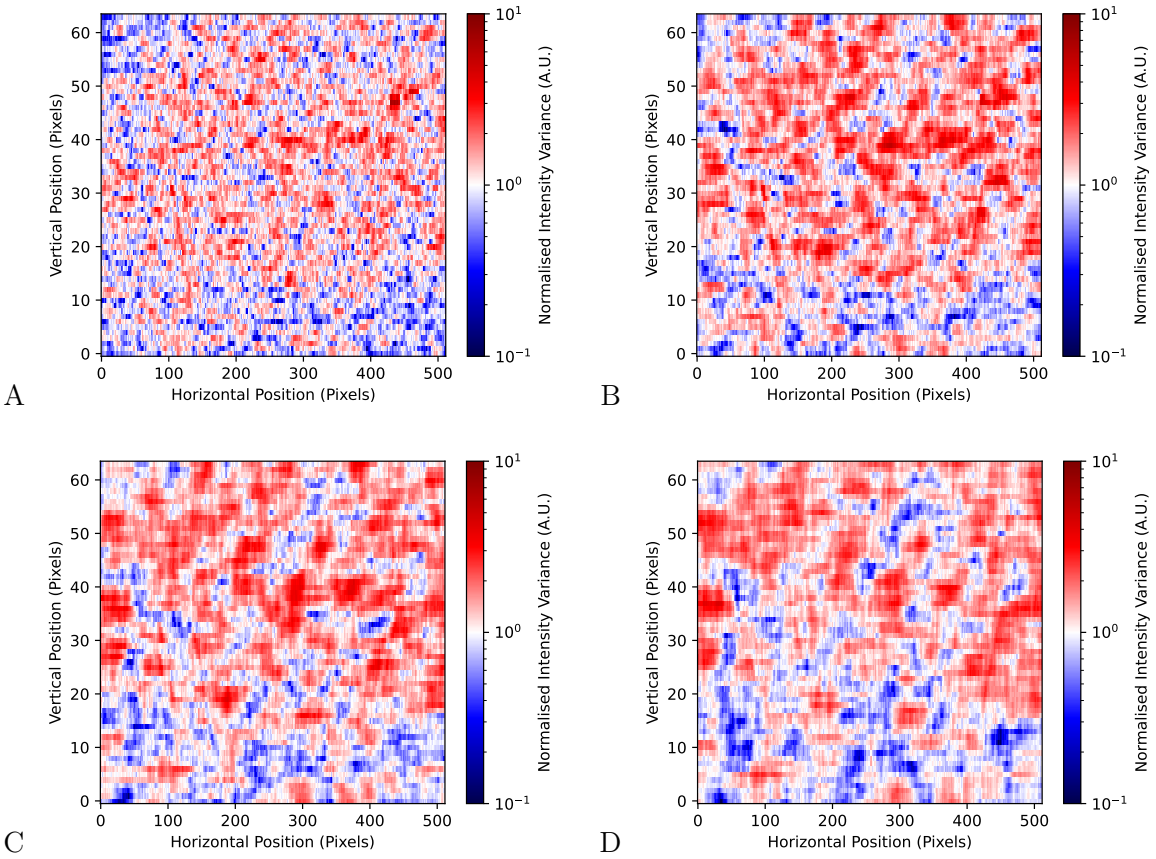


Figure 3.7: A progressive series of normalised variance images on the subtracted data for different kernel sizes generated from our real data. A: The image generated for a kernel size of 16×2, with an average normalised variance of 0.37. B: The image generated for a kernel size of 32×4, with an average normalised variance of 1.15. C: The image generated for a kernel size of 48×6, with an average normalised variance of 1.19. D: The image generated for a kernel size of 64×8, with an average normalised variance of 1.27

Looking at these images, it is obvious that the method produces a blur on the data. This blur is more significant for larger kernel sizes, an expected trend. There are no significant patches of squeezing (sub 0 values) anywhere in the normalised variance images. In fact, no significant increase in squeezing is seen at all, and the variance increases with larger kernel size.

Thus, this simple solution is not fully correct, as there is no evidence of the intensity

squeezing that has previously been demonstrated. Clearly there is something more intricate going on here that is leading to the squeezed regions in each beam not being aligned as expected. Thusly, their subtraction does not lead to a multi spatial mode squeezed state.

One explanation is that there could be other effects that are influencing the beams as they travel through the cell, distorting them. This would explain the peak shown in figures 3.5 and 3.6, since a translation somewhere in the 20 to 100 pixel range would produce a sharp rise in noise in that spatial wavelength range.

3.2 Top Hat Searching

To attempt to map the distortion on the squeezing between the beams a correlation function was produced from the data. This was done by scanning the beams past each other digitally, while the squeezing between them was computed.

Firstly, the Top-hat convolution kernel was applied to the data to account for the coherence area. From here, fourth order 'scanning' arrays were constructed by adding, P, or subtracting, N, each of the beams from each other for every possible x displacement between the beams. These are given by

$$P_{s,x,x',y} = Pr^{Cv}_{s,x,y} + C^{Cv}_{s,x',y}, \tag{3.4}$$

and

$$N_{s,x,x',y} = Pr^{Cv}_{s,x,y} - C^{Cv}_{s,x',y}, \tag{3.5}$$

where x and x' are two independently varying values that extract the x index of the $Pr^{Cv}_{s,x,y}$ and $C^{Cv}_{s,x,y}$ arrays.

It was decided to scan the x-axis only. This is where the displacement effect is expected

to be, by virtue of the fact that the beam is only angled in this axis; it also saves on processing time. The rest of the method then continues as it does in the simple subtraction method, only that now the normalised variance array is three-dimensional ($V^N_{x,x',y}$). Thus, the produced data is four-dimensional. This is something of a problem for representing the data graphically, as it would be impossible to render all of it at once. Thus, a single y value is chosen for which the normalised variance in intensity is represented as a heat map on the x and x' axis. This single value still contains information from a chunk of y values in the original images, however, by virtue of the convolution process.

3.2.1 Results and Discussion

Now, the process is applied to real data. This time, the kernel size is set to be 48x6, as this is larger than the predicted coherence area for the system. Also note, this time normalised variances are plotted at $y = 18$, which is where the clearest squeezing has been found.

To see any detailed patterns, frames with a good coverage of the visible squeezing over the entire x domain were needed. These were found by plotting the data at $y = 18$ for all 42 frames then visually inspecting them, to determine the general quality of the squeezing present. Later, it was determined that these frames were the ones with the lowest spatial DC noise from the data set. Such post selection was acceptable, as this data is intended to guide future experimentation rather than to be used as proof of an underlying effect. At this point, the main focus was to use frames that show good coverage of squeezing. An example of a high-quality frame is shown in figure 3.8. This image shows a reasonably comprehensive view of the squeezing over a large proportion of the x-axis.

Inspecting figure 3.8, the beginnings of a pattern do seem to be emerging, that is not

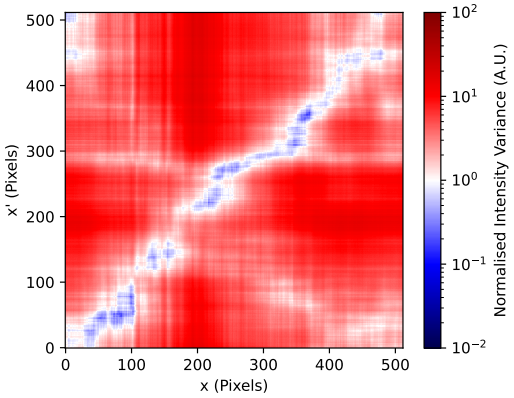


Figure 3.8: The squeezing map of frame 1, with a kernel size of 48x6 at y = 18.

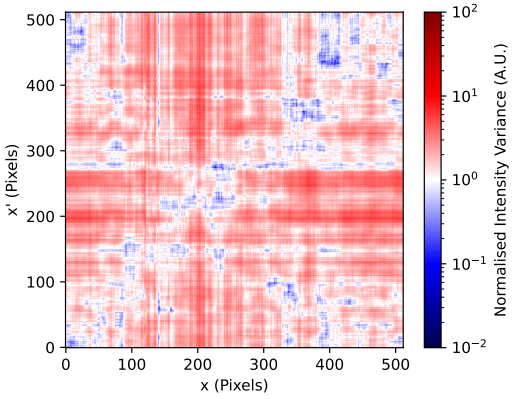


Figure 3.9: The squeezing map of frame 1, with a kernel size of 16x2 at y = 18.

on the x'=x line as may be naively expected. However, this pattern would have to be consistently displayed on multiple frames for such a conclusion to be made. Although there is a distinct decrease in the normalised variance along the $x' = x$ line, there is also a similar decrease in the $x' = 512 - x$ line. Never below 0, however. This hints at the presence of some classical effect that is causing this. Further evidence for this can be seen by taking this same image, but setting the kernel size to be 16x2, which is smaller than the predicted coherence area. If this effect were due to some squeezing process, it would now be expected to vanish. However, as seen in figure 3.9, neither of the lines disappear despite there being no squeezing present in the image.

One possible explanation would be some sort of classical noise on the power of the laser that produces the pump and probe beams. This would result in the same noise being imparted on the conjugate beam, which would cause some covariance between them. To determine how exactly this would affect the variance profile of our subtracted beams, each beam can be modelled as a position dependent random variable. These are then multiplied by another random variable, A, to simulate a shared classical white noise.

Thus, the subtracted variance of the two beams can be given as

$$\sigma_-^2 = Var(APr(x,y) - AC(x',y')), \tag{3.6}$$

where Pr(x,y) and C(x',y') are the idealised beams. Pr(x,y) and C(x',y') have a variance given by $\sigma_{Pr}^2(x,y)$ and $\sigma_C^2(x',y')$ and A is defined to have a variance given by σ_A^2 and expectation given as μ_A.

This can now be expanded using equation 3.6 to give the three term expression,

$$\sigma_-^2 = Var(APr(x,y)) + Var(AC(x',y')) - 2Cov(APr(x,y), AC(x',y')). \tag{3.7}$$

The first two terms can be further reduced by using the standard formula for the variance of the product of two random variables [84]. The final term may be expanded using the definitions of covariance and variance, like so

$$-2Cov(APr, AC) = -2(\overline{A^2 PrC} - \overline{APr}\ \overline{AC}), \tag{3.8}$$

where the dependency of Pr and C on position has been left out, for clarity, and the overline represents the mean of the combined variables. This then becomes

$$-2Cov(APr, AC) = -2(\overline{A^2}\ \overline{PrC} - (\overline{A})^2\ \overline{Pr}\ \overline{C}). \tag{3.9}$$

Then, using the definition of covariance, we arrive at

$$-2Cov(APr, AC) = -2(\overline{A^2} Cov(Pr, C)). \tag{3.10}$$

Finally, using the definition of variance, we result in the full expression for the subtracted variance, given by

$$\sigma_-^2 = \sigma_A^2(\mu_{Pr}^2(x,y) + \mu_C^2(x',y') - 2\mu_{Pr}(x,y)\mu_C(x',y'))$$

$$+(\mu_A^2 + \sigma_A^2)(\sigma_{Pr}^2(x,y) + \sigma_C^2(x',y')) \tag{3.11}$$

$$-2(\mu_A^2 + \sigma_A^2)Cov(P(x,y), C(x',y')),$$

where the position dependency of the terms has now been reinserted.

What is immediately obvious is that this is a three part expression, governed by different aspects of the system.

The first term only exists for systems where there is excess shared classical noise on the beams, hence $\sigma_A^2 > 0$. This is what seems to generate the cross shaped interference seen in the real data. This can be made clearer in a plot. This is done by first dividing this expression by $\mu_A(\mu_{Pr}(x,y) + \mu_C(x',y'))$ (our normalisation process). Then y is set to $y = y'$ and the covariance due to squeezing is assumed to be 0. After this $Pr(x,y)$ and $C(x',y')$ can be approximated to be 2D Gaussian functions centred on $x = 256$ $y = 32$, with Poissonian noise and FWHMs of 256. Finally, the normalised variance is plotted in terms of x and x'. The result is shown in figure 3.10.

Where σ_A^2 is set to 1 and the magnitude of μ_A can also be taken as 1, by definition. The maxima of Pr(x,y) and C(x',y') are arbitrarily set to 100. It is immediately obvious that the shape of this plot is very similar to the cross pattern seen in figure 3.8 lending this explanation some credence, although the cross seen in the real data is somewhat offset by the beams not being perfectly centred and striated by the prior top hat convolution. For any system with excess classical noise, outside the small region about the $x' = x$ and $x' = 512 - x$ lines, the normalised variance will rise rapidly. This could have a sig-

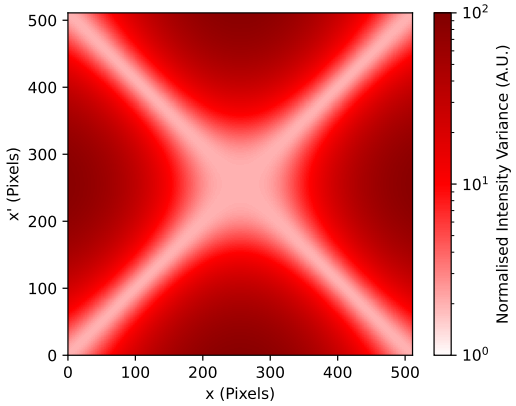


Figure 3.10: The Variance map of the simulated data.

nificant impact on the visibility of squeezing outside these small regions, rendering large displacements in the pattern invisible. This would mean that it would be impossible to build an intensity squeezed image if the squeezed regions in the beams were displaced from each other in a non linear way, even if image registration was used to correct for those displacements.

The second term of the expression will always be present, as it represents the combined shot noise of the system. Assuming the beams are shot noise limited, this should normalise to 1 and any fluctuations below this can confidently be seen as squeezing.

However, another problem arises for systems with $\sigma_A^2 > 0$, as this will produce an artificially larger term, that will normalise to a value higher than 1. The issue here is that the sensitivity to squeezing will be reduced over the entire image.

The third term concerns the extra covariance between the beams caused by the squeezing between them. It depends on both the mean and variance of the classical noise on the system. As the distribution of squeezing is the current focus, the σ_A^2 dependence is not a problem, but it may be beneficial to reduce it for other applications.

Largely, all of these issues can be removed by making the excess classical noise, and hence σ_A^2, sufficiently small. Fortunately, a solution to this could be implemented in the form

of the noise eater, a optomechanical device for reducing classical noise on the intensity of a laser beam. The efficacy of which is investigated in chapter 4.

CHAPTER 4

THE NOISE EATER

AS touched on in chapter 3, a noise eater was added to the apparatus to diminish the power noise on the main laser beam. The hope was that this would reduce the temporal noise on the beam such that squeezing would be less obscured by the classical noise 'X' effect seen in chapter 3 and could be seen on the camera. This is a significant effect when points of differing intensity on each beam are subtracted from each other, as the classical noise is not fully removed. Further, any loss on the probe beam would lead to imperfect classical noise cancellation. This would impact the whole beam and not just 'mismatched' regions.

A target noise suppression bandwidth of 100 KHz was decided upon, as this is significantly faster than the operation of the camera so should cover all the interfering frequencies. Additionally, if the bandwidth was found to be too high, it would have been simple to limit it with a standard RC filter.

4.1 General Principles

The function of a noise eater is to use electro-optical control elements and a feedback signal from a laser's output to compensate for any classical noise on the beam. The quantum noise cannot be reduced in this way since it will not be common to the main beam and the pick-off used for the feedback system [85, 86, 87]. For a similar reason, the greater the proportion of the beam that is taken in the pick-off the less detrimental the quantum noise will be to the feedback. This can be seen by noting that the pick-off signal will need to be multiplied by a constant, g, proportional to

$$g = \frac{P_{laser}}{P_{pick-off}} \tag{4.1}$$

where P_{laser} is the power of the main beam and $P_{pick-off}$ is the power of the pick-off, to properly compensate for the classical noise when it is applied to the final control element. The pick off will necessarily mix uncorrelated noise onto both the main beam and the pick off, which can be viewed as noise coupling from the vacuum port of the pick-off beam splitter. As such, this (non-common) noise will also be multiplied by g and applied to the main beam. This will limit the performance of the noise eater. It can be shown that in the best case the noise can be brought to shot noise, when the reference beam is much at a higher power than the main beam.

The frequency response of this system is limited by the bandwidth of the electrical components used in the noise eater, which is typically much lower than optical frequencies. However, since the classical intensity noise on a laser generally follows a 'pink' distribution, the majority of the noise it was required to remove falls below this bandwidth [88]. A diagram of the system used in the experiment shown in figure 4.1.

In this case, the feedback signal is provided by a fast photodiode, the details of which are

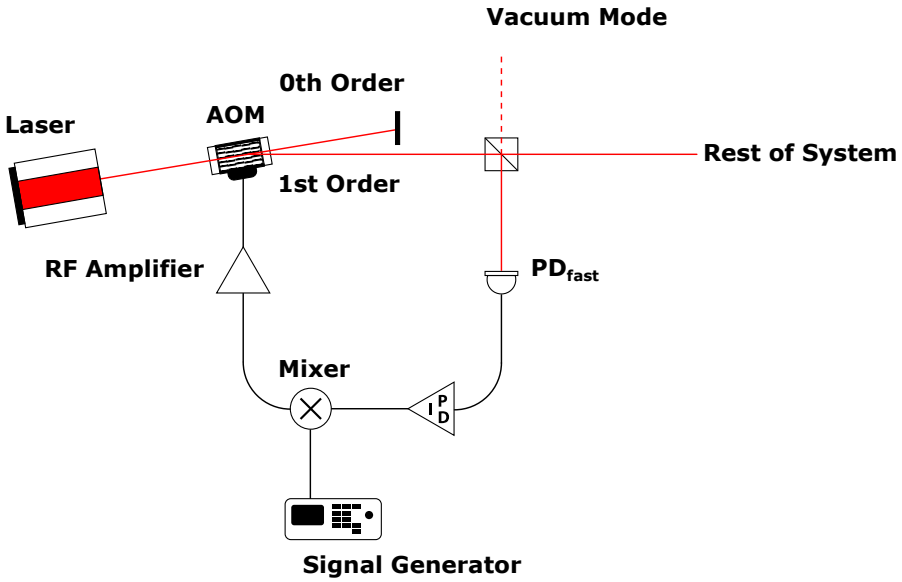


Figure 4.1: A diagram of the noise eater set up. In this case, the mixer is used as a variable current controlled attenuator for the RF driving the AOM.

discussed in the next section. This signal is transmitted through a PID (proportional, integral, differential) electronic control circuit and is used to modulate the intensity of the RF signal generated by the signal generator that is sent to the pre-AOM amplifier. The maximum power of the RF signal is set by adjusting the power of output of the signal generator. The AOM acts as a control element to modulate the laser power that is output to the rest of the system. This is because only the $1st$ order mode is allowed to pass, with the other modes being blocked with an aperture.

A power spectral density is a measure of how the power of a signal is distributed across different frequencies. It is typically defined for a real sationary signal, $x(t)$, as

$$S_x(f) = \int_{-\infty}^{\infty} R_x(\tau) e^{-2if\tau} d\tau, \tag{4.2}$$

where $R_x(t)$ is the auto correlation of $x(t)$ and τ is the time lag in the autocorrelation function.

The noise power spectral density, normalised such that 1 is the shot noise level of a coherent beam, achievable in this system can be found to be

$$S_f(\omega) = \frac{1 + \eta_f \epsilon_f S_0(\omega)}{|1 + \tilde{h}(\omega)|^2}, \tag{4.3}$$

for the beam intensity in the feedback path, and

$$S_n(\omega) = 1 + \frac{\eta_n \epsilon_n}{\eta_f \epsilon_f} \frac{\eta_f \epsilon_f S_0(\omega) + |\tilde{h}(\omega)|^2}{|1 + \tilde{h}(\omega)|^2} \tag{4.4}$$

for the output beam. Where: $S_0(\omega)$ is the power spectral density of the original beam; ϵ is the fraction of light diverted to each beam; η is the quantum efficiency of each detector; and $\tilde{h}(\omega)$ is the Fourier transform of $h(t)$, a time-domain convolution function that accounts for any filtering effects of the electronics, of the gain of the amplifier, and of any time delay in the electronics - the transfer function [89].

Interestingly, the noise on the feedback signal can be squeezed to an arbitrarily high level in this system. However, it would be impossible to use this beam practically, as it would mean taking it out of the feedback loop.

Looking at equation 4.4, it can be seen in the high gain limit, where this circuit tends to operate, $S_n(\omega)$ can be reduced to

$$S_n(\omega)_\infty = 1 + \frac{I_n}{I_f}, \tag{4.5}$$

where I_n and I_f are the powers of the output beam and the feedback beam. Since the pump and seed beams both derive from the noise eater output beam they both have their intensity noise reduced. However, the pump beam, which is roughly 100 times more intense than the feedback beam, will only have its noise suppressed minimally, whereas the seed beam noise will be significantly suppressed, since it is typically at tens

of microwatts and the feedback signal is at tens of milliwatts.

Further, in the cell the pump beam typically operates near saturation for the 4WM process, which prevents much of the noise from being imprinted on the final probe and conjugate beams. This leaves the seed beam as the dominant and most suppressed noise source. As such, the probe and conjugate beams will have a greatly reduced noise profile.

4.2 AOM considerations

It would be reasonable to consider using the $0th$ order output of the AOM instead of the $1st$ order, since less of the input beam would be lost before it passes to the rest of the system [90] and is used to generate the seed and pump beams. This is because the $0th$ order output only fundamentally limited by the insertion loss of the AOM. This is opposed to the $1st$ order output that has a limited diffraction efficiency, typically around 50% at saturation. Practically, this has to be even lower in a noise eater system, as the electro-optical control element ideally operates in a linear regime. This limits the total power that can be used to generate the pump beam, which in turn limits the maximum beam waist the pump can be focused to whilst still saturating the 4WM interaction in the Rb cell.

However, the nature of $0th$ order transmission through an AOM would make this topology unviable for the target bandwidth of the noise eater. Since the acoustic wave inside the AOM crystal takes time to propagate across the beam cross-section, there is a inherent delay on any signal's action on the beam. This delay limits the attainable bandwidth of the system. However, in this case, it is minimised by focusing the beam into the AOM which reduces the beam cross-section and thus reduces the inherent delay, allowing us to hit our target bandwidth. However, this comes with the compromise that the beam at its focus will is composed of a spectrum k-vectors that will each interact with the AOM

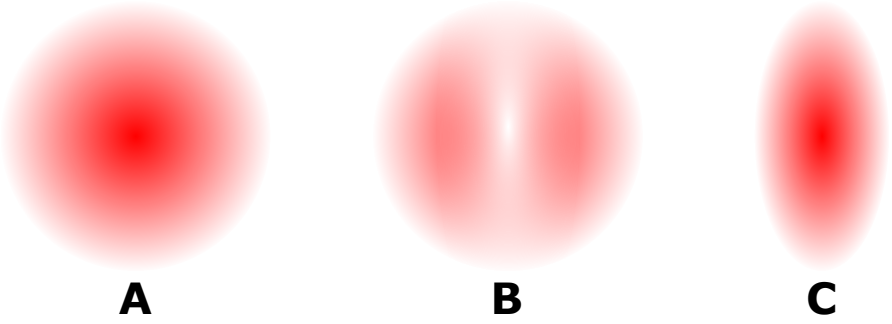


Figure 4.2: A diagram of the input and output modes of a typical AOM, in the far field of the AOM (momentum picture). A) A perfectly Gaussian input beam. B) The $0th$ order output. C) The $1st$ order output.

differently. The effect of this is made clearer by the diagram in figure 4.2 which shows the cross-section of some output modes of a typical AOM in the far field, given a focused Gaussian input.

It is important to note that while the input and non-zero output modes (A & C) are Gaussian the $0th$ order output typically is not. This is because, in standard operation, an AOM operates under the Bragg condition, given by

$$\theta_B = \frac{\lambda F}{2\nu}. \tag{4.6}$$

Where $\lambda = \lambda_0/n$ is the wavelength in the crystal, ν is the acoustic velocity and F is the input RF frequency.

As such, light that is incident at this angle will be efficiently diffracted into higher modes, while any movement from this optimum will rapidly decrease in diffraction efficiency. This means that a focussed beam that is aligned such that its average k-vector is at the Bragg angle will have its more aligned parts diffracted, whilst its more divergent parts are not. This leads to the far field intensity profile shown in B.

This highlights one reason the $0th$ mode is not used – poor output beam quality. On top of this, this control element would only be acting on the middle of the beam. So, while

the noise on the entire beam was suppressed, any noise corrections attempted would be imprinted from the periphery onto the central region of the beam, actually increasing the noise locally. This means some high spatial mode noise would be introduced to the system that was not there at the beginning. The result would be a beam that overall has a reduced classical noise profile, but locally has a much higher one. This could be useful in some applications, but is completely unacceptable for imaging applications like in our experiment. It was also not an option to fully clean the output beam using a fibre optic, since an especially large amount of power is needed that is far above the damage threshold for almost all readily available fibres not to mention that the coupling efficiency into the fibre would likely be no better than the efficiency through the AOM.
As such, the $1st$ order mode is a much superior option for this system, despite this coming at the cost of wasted power.

4.3 A High Power, Low Noise, and High Bandwidth Photodiode Front End

This section overviews the component selection and design process of the photodiode front end. The most relevant frequency response range for this device was defined by the PIXIS camera. When running in kinetic fast mode, an entire series of images, or a frame of data, can be collected in $\sim$ 3ms. This puts the minimum frequency that classical noise will be imprinted on the data in the 100Hz regime. The upper frequency of noise imprinting is defined by the shift speed of a single row of pixels in the camera. This occurs in $\sim 3\mu$s, which begets a characteristic frequency of $\sim$ 100KHz. As such, the main design goals of this project were set as a bandwidth of at least $0 - 100$kHz, as high of a maximum optical input power as possible, and an electronic noise floor below

the photonic shot noise incident on the detector.

4.3.1 Photodiode Theory

The first component to be selected in this photodetector design was the photodiode itself, since its characteristics defined the ultimate limitations of the device. There are many things to consider when picking a photodiode, which can be better understood when considering the physics of such a device.

Typically, for high bandwidth and high input power systems, a PIN photodiode is used, rather than a standard PN diode [91]. The primary advantages a PIN diode has over a PN diode are that the quantum efficiency is better, the saturation power is higher, and the capacitance is lower. The difference being that the PIN diode has a thick undoped intrinsic region sandwiched between the P and N regions, as shown in figure 4.3 [92]. In a PIN diode, most of the depletion region is within the intrinsic region and this depletion region is larger than in a PN diode.

This leads to the quantum efficiency of the device being superior, since the electron-hole pairs generated by photon absorption in the PIN depletion region are much more likely to contribute to output current than those generated in the P or N regions. This is because the electric field across the depletion region quickly sweeps the charges in opposite directions, preventing their recombination. Electron hole pairs generated in the P and N regions usually recombine, unless they diffuse apart quickly enough. Since the depletion region is much larger in a PIN diode, more of the incoming photons are converted. This larger volume of photon conversion also allows for a higher saturation power for PIN diodes, making them suitable for high-power applications. Another significant advantage of this system is that the capacitance of the PIN photodiode smaller. This is important for high bandwidth applications, as this capacitance will form a low pass filter with the

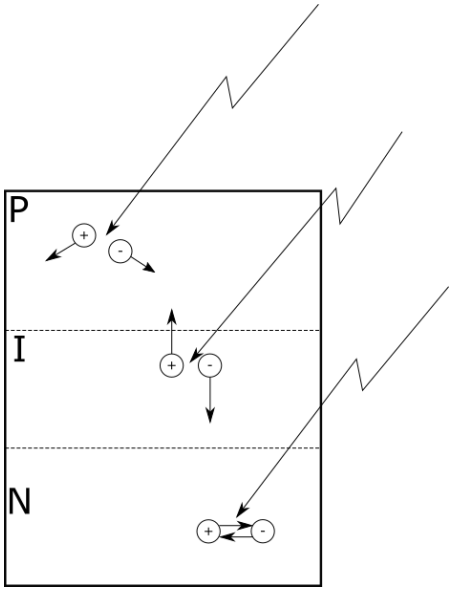


Figure 4.3: The structure of a PIN photodiode.

load resistance.

Reverse Bias

A PIN photodiode is often reverse biased by driving its cathode positive relative to its anode. This will cause its depletion region to grow, at the expense of the other regions. This grows the volume of effective photon conversion, which results in the saturation power of the diode increasing. The capacitance will also decrease, due to the increased distance between the charged regions in the diode. This decrease is given by

$$C_B = \frac{C_0}{\sqrt{1 + \frac{V_B}{\phi}}}, \tag{4.7}$$

where: C_0 is the initial junction capacitance of the diode, V_B is the bias voltage, ϕ is a constant and equal to 0.6 V, and C_B is the biased junction capacitance. [93]

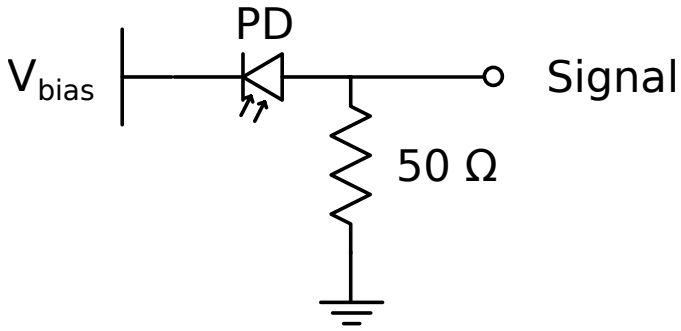


Figure 4.4: A circuit diagram of the photodiode front end circuit.

4.3.2 Front End Design

It was decided that an operational amplifier based trans-impedance amplifier circuit (TIA) was the best design for the photodiode front end. Using a TIA allows for a much lower load impedance, which reduces the low pass filtering effect of the photodiode and increases the signal bandwidth. This design also allows other noise reducing features to be added, which will be discussed later.

The Hamamatsu S1223-01 PIN photodiode was chosen as the photodiode in this device, since it has a relatively low junction capacitance of $20pF$ for its detection area, $13mm^{-2}$ and thermal dissipation ($100mW$) [94].

However, before committing to an exact design, the saturation characteristics of the chosen photodiode at different voltages were evaluated, since this information was not readily available on the data-sheet. They were also compared to a Thorlabs PA100A-EC photodetector already available in the lab for reference [95]. This was done using the test circuit in figure 4.4.

The test circuit and the Thorlabs detector were compared by directing a $780nm$ laser with a spot size of $1520 \pm 10\mu m$ onto each of the detectors and varying its intensity. The output voltage of each of the detectors was then plotted. The result of this is shown in figure 4.5.

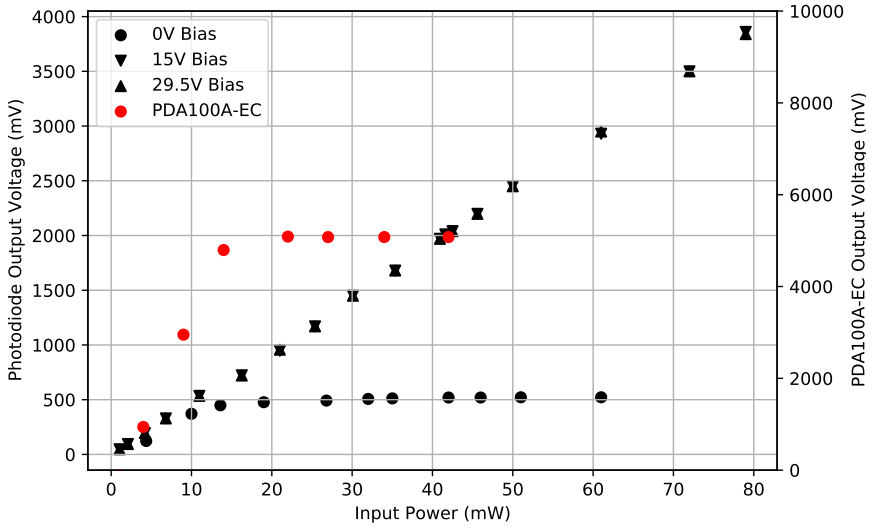


Figure 4.5: A comparison of the saturation powers of each of the photodetectors, the error on both the voltage and incident power is roughly shown by the size of the plotted points.

It is clear to see that even at the relatively modest bias of $15V$ the S1223-01 almost doubles the saturation power of the PA100A-EC photodetector. This advantage can be pressed far further, up to almost $30V$, but $15V$ was decided as a good starting bias to prevent any possibility of damage to the PID circuitry in the event of a short.

Based on this, a TIA photodiode front end was designed. A circuit diagram of this device is shown in figure 4.6.

The positive bias voltage for the photodiode is provided by a LM7815 voltage regulator that converts a supply voltage of $+18V$ to $+15V$. This provides the added benefit of filtering the noise from the power supply more than a simple low pass filter could.

The next stage was the TIA itself, constructed from a THS4631 op-amp, a resistor, and a capacitor. They also generally produce a more linear output than a simple resistor would. To minimise noise, the power rails on the op-amp were supplied via LM7915 and LM7815 voltage regulators, extra noise filtering was also implemented with a pair of

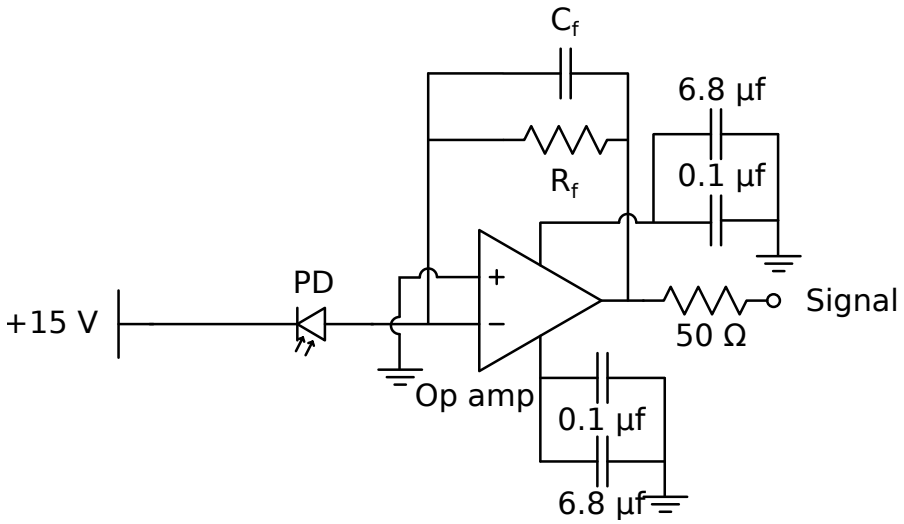


Figure 4.6: A circuit diagram of the TIA based photodiode front end.

ceramic capacitors on each rail ($0.1\mu F$ and $6.8\mu F$).

The THS4631 was chosen specifically because it has a high bandwidth whilst still being a FET input device. The advantage of a FET input is the extremely high input impedance at low frequencies, which helps to avoid variation in output offset voltage with input signal swing. As such, the accuracy of current to voltage conversion is maximised.

The final bandwidth of the detector can be calculated as

$$F_{-3dB} = \sqrt{GBP\ f_0} \tag{4.8}$$

Where GBP is the gain bandwidth product of the op amp ($210MHz$) and

$$f_0 = \frac{1}{2\pi R_f (C_i + C_f)}, \tag{4.9}$$

with R_f being the feedback resistor and C_f the feedback capacitor. C_i is a combination of the capacitance of the photodiode and op amp. [96] This was found to be approximately $30pF$ from data sheets. The feedback resistor was chosen to be 700Ω so that the maximum

feedback current was around $20mA$, the expected maximum output current from the photodiode. The feedback capacitor was chosen to be $9pF$, using a formula in the data sheet recommended for this purpose.
Putting this all together, the final bandwidth of the system was calculated to be roughly $40MHz$. However, this is more of an upper limit as, in practice, things like parasitic capacitance in the detector PCB reduce this bandwidth substantially.

Supply Ripple Rejection

After some preliminary testing of the custom detector, it was noticed that the signal it produced had a significant low frequency electrical noise imprinted on it. Since this noise was also present when there was no incident light on the detector, it was quickly traced to the circuit's power supply. Although the voltage regulators had a particularly high noise rejection, it was found that they were not efficient at removing mains ripple.
As such, an extra filtering stage was added just before the voltage input of the device. This consisted of a capacitance multiplier circuit, the design of which is shown in figure 4.7 [97].
This filter is, in essence, a simple low pass RC filter with amplification due to the transistor part of the circuit. The elements on the positive and negative rails are mirrors of each other, with the obvious exception that the negative rail uses a PNP transistor whilst the positive rail requires an NPN one.
The circuit functions as a typical RC filter, with a cut-off frequency

$$f_{-3dB} = \frac{1}{2\pi RC}, \tag{4.10}$$

where R is the resistance of the resistor and C is the capacitance of the capacitor. With a resistance of 220 kΩ and a capacitance of 10 μF this provides a cut-off of 0.07 Hz, far

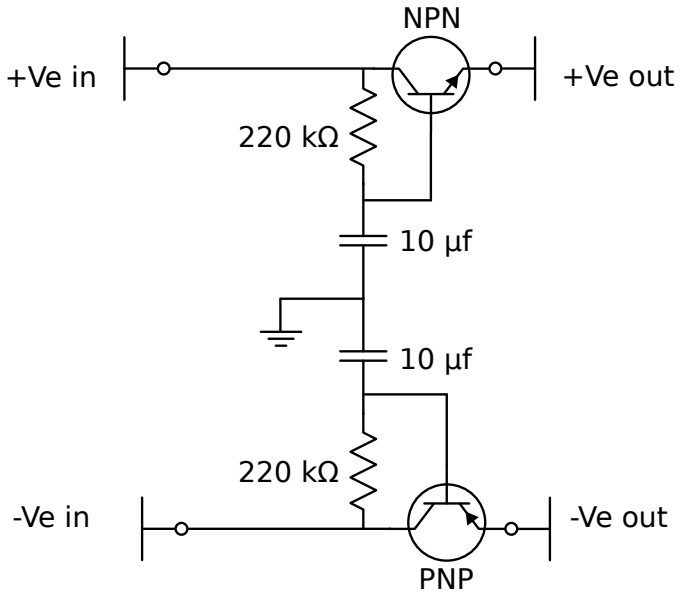


Figure 4.7: A circuit diagram of the capacitance multiplier filter.

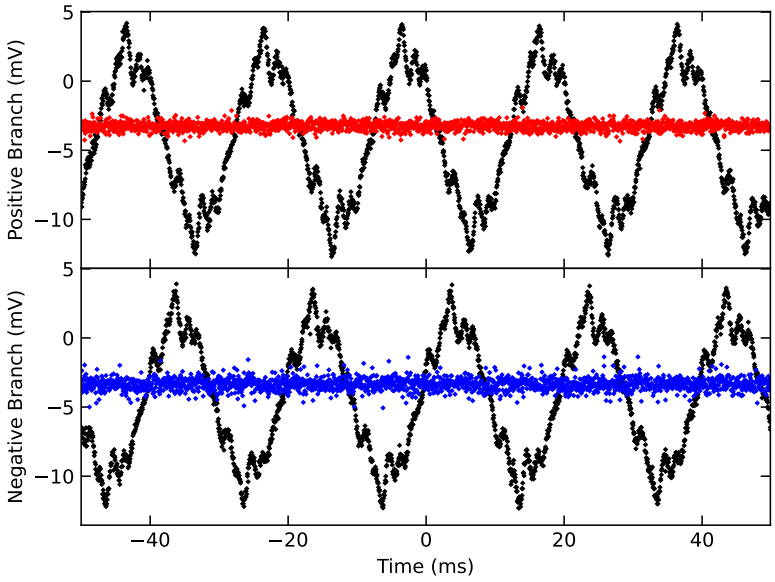


Figure 4.8: A recording of the ripple on the positive and negative branches of the power supply both before (black) and after (coloured) the capacitance multiplier filter.

below the 50 Hz mains ripple that was targeted.

As in a typical RC filter, the resistor provides the charging current for the capacitor. In the capacitance multiplier circuit it also provides the base current for the transistor. Without the transistor, any fluctuations in current demand from the circuit down stream would have to be met by a capacitor. As such, it would need a large capacitance to smooth effectively. However, with the transistor in place, the current demand is reduced by a factor, β, which is the gain of the transistor. As such, the system can supply much more current than just the capacitor alone so in this way acts as a much larger capacitor, hence the capacitance multiplier moniker. As such, much more smoothed current can be supplied and ripple reduction is multiplied by β.

Due to the presence of a transistor an extra voltage drop of approximately $0.65V$ was produced across the filter. This was not a problem, as it could be compensated for by increasing the input voltage from the power supply. Furthermore, the low current requirements of the custom photodetector meant that thermal dissipation was not an issue. The resistors used in this circuit were typical thick film through hole type, as resistance accuracy was not a performance critical attribute. The capacitors, however, were specifically chosen to be film type, as to avoid the microphonics associated with other types of capacitors [98]. These can couple ambient acoustics into the circuit and contribute to noise. The BC559 and BC549 transistors used in this circuit were chosen mainly for availability, but they are capable of direct current gains far exceeding 100x [99, 100].

The a comparison of the power supply ripple is shown before (black) and after (coloured) this filter in figure 4.8. This plot was produced using an oscilloscope in AC mode.

The signal-to-noise ratio (SNR) of the custom detector was then compared to the PDA100A-EC, to validate the design. This was done by taking an oscilloscope trace of the output of the two detectors in the cases where they were illuminated with 0 and 7.25 mW of laser

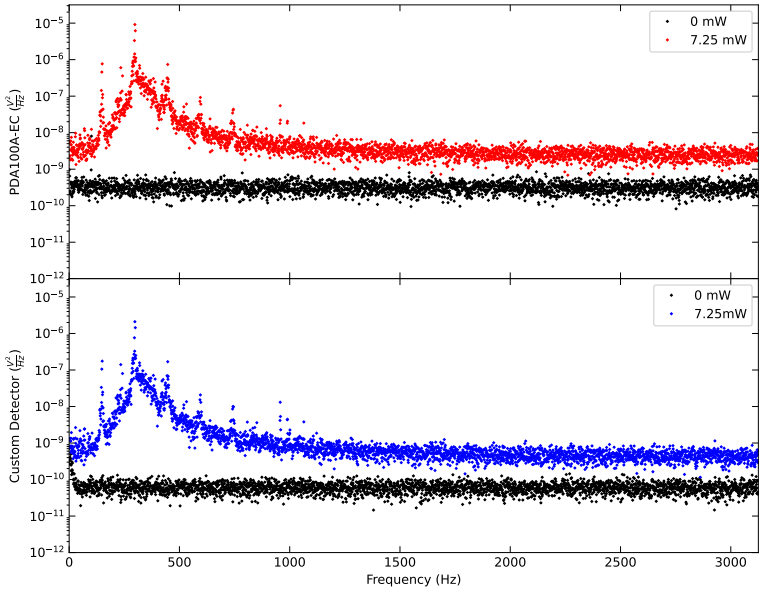


Figure 4.9: PSDs of both detectors, at $0mW$ and $7.25mW$ incident intensity.

light. These readings were then converted to a power spectral density. This is shown in figure 4.9.

As can be seen, the response of the two detectors is near identical over the $1KHz$ range shown here, with them both showing a distinct peak of the ratio at approximately $300Hz$. More intriguing, however, is the presence of sharp peaks spaced approximately $150Hz$ apart. These are harmonics of some large low frequency classical noise on the main laser, which it was hoped the noise eater will act to reduce.

These measurements also allowed a comparison of the transimpedance gain of the two detectors and it was found that the Custom detector to PDA100A-EC gain ratio was approximately 0.6.

4.4 The AOM, Amplifier, Mixer, and RF Chain

The next section of the system optimised was the electro-optical control element. This consists of a low noise 72-14122 RF generator that is fed through a ZP-5-S+ mixer, then an RF amplifier and finally an AOM. The initial AOM driving signal is produced by a signal generator at a power of 12 dBm. It is then passed through an 11 dBm limiter and reduced to 0 dBm by an 11 dBm attenuator. The goal was to saturate the limiter to reduce the noise on the RF signal. This works as, when saturated, a slight change in the input power will have an insignificant impact on the output power of the limiter. This is similar to the saturation attained in section 2.1 and works for the same reason. The AOM itself, however, cannot be saturated as it needs to be in a relatively linear region to effectively act as an electro-optical control element.

The mixer itself is used in an unusual configuration where the signal is input onto the input terminal of the mixer and the output is taken from the local oscillator terminal of the mixer which is then sent to the pre AOM amplifier. The output of the lock box is put into what would usually be the output terminal of the mixer. In this configuration, the output current of the lock box can control how much of the signal can pass into the amplifier and it acts as a variable attenuator. Ultimately, this allows control of the final amount of light that passes into the $1st$ mode of the AOM and into the rest of the experiment.

Due to this atypical setup, the saturation current into the mixer needed to be determined, as it was not quoted on the mixer's data sheet. This was so the output resistor, that defined the output current range, on the lock box could be set appropriately. This was done by simply recording the efficiency of the AOM transmission at different input currents, provided by a power supply. The result of this is shown in figure 4.10.

From this graph, the saturation power was approximated to be just over $5mA$, so the

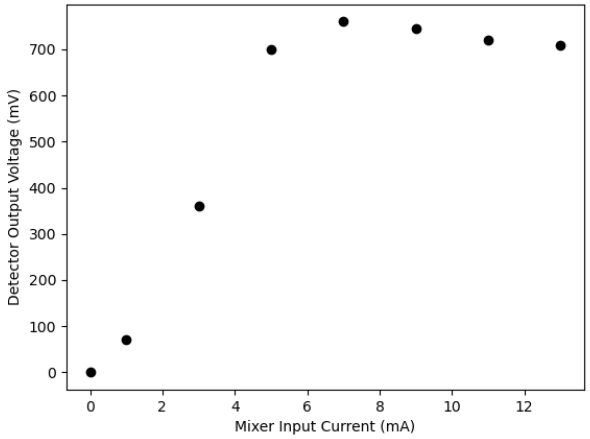


Figure 4.10: A plot of the input current into the mixer vs. the DC voltage on the feedback photodiode. The error on both the voltage and the current is roughly shown by the size of the plotted points.

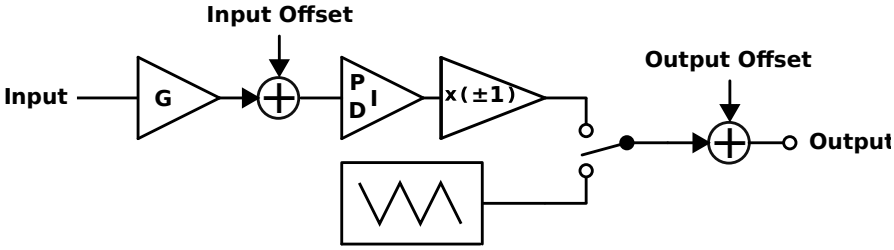


Figure 4.11: A simplified diagram of the lock box circuitry.

output resistor value on the lock box was chosen to be 1kΩ. This limited the absolute maximum output current of the system to $15mA$. From there, the lock box parameters could easily be adjusted to produce an output at the ideal range.

4.5 PID Lock Box

A simplified schematic of the circuit is shown in figure 4.11.

The lock box itself consists of two separate parts, that can be switched between during

operation. The first is a triangle wave generator (jagged line) that is used to ensure the system is working at as close to saturation as possible, hence operating at the highest possible transmission efficiency. The frequency, amplitude, and output bias can be altered using potentiometers built into the PCB.

The second section is the PID stream itself (top) [101]. This takes the input and passes it through an instrumentation amplifier (leftmost) of variable gain, G. After, an input bias is introduced via an op amp adder circuit. This allows the target position of the PID loop to be set. Then the signal is then split and passes through a unity gain amplifier, an op amp integrator, and an op amp differentiator (PID). The signal is then recombined with an adder and the contribution of each of these terms is set with potentiometers. Next, the signal can be optionally inverted with an inverter x($\pm$1) before passing through the output adder and out of the device.

4.6 Final System Testing

All the elements discussed previously were connected to form the final system, which was expected to reduce the classical noise greatly on the beams. However, to actually measure if there was any noise reduction caused by the system, additional optical elements had to be added to the setup. These facilitated the measuring of the noise on the beam before and after the noise eater, allowing the noise reduction to be measured. They also added flexibility on the power allowed to shine on each of the detectors. These additions are shown in figure 4.12.

The input beam is polarised in the vertical direction. The active elements in the setup are the AOM and the NE p.d., which are directly involved in the noise eating loop. Aside from this, there is also a pick-off from before the AOM that allows control of the power input into the system. Another pick-off is present just to the left of it, controlling the

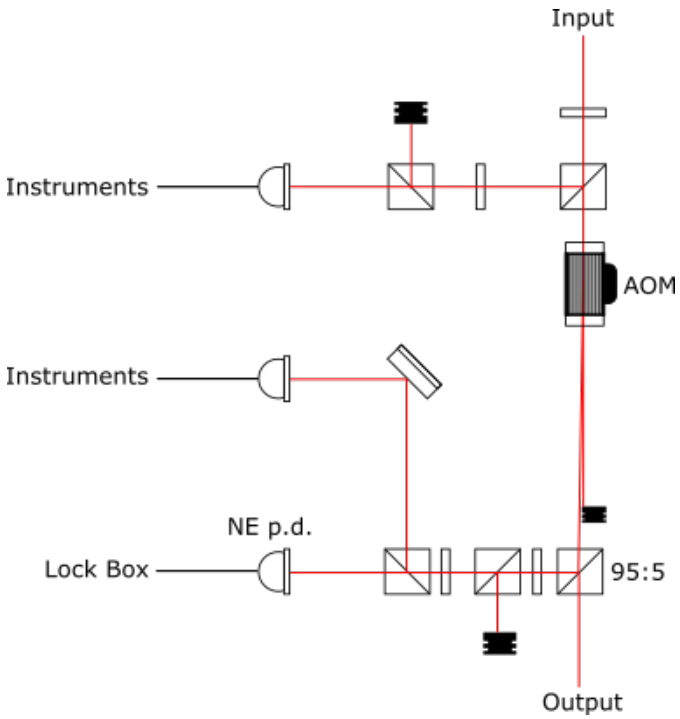


Figure 4.12: A simplified diagram of the optical set-up for measuring the level of noise reduction by the Noise Eater. The noise eater photodetector (NE p.d.) was the custom one previously discussed and the unlabelled photodetectors were Thorlabs PA100A-EC type.

power incident on one of two Thorlabs PDA100A-EC photodetectors. After the AOM, a beam block prevents the $0th$ mode from passing into the rest of the system, while allowing the $+1st$ mode to pass uninterrupted. After this, 95% of the beam continues on to the rest of the experiment, while 5% is shared between the NE p.d. and the other Thorlabs photodetector. All the pick-offs consist of a half-wave plate (HWP) and a polarising beam cube (PBS) to allow easy control of the pick-off proportions. The output of the detectors was connected to a DSO-X 3014A Oscilloscope, to measure noise power from DC to $100KHz$.

Before testing, the pick-offs were adjusted to ensure the power on each detector was as close to identical as possible, so that the noise readings on the instruments could be directly compared to each other.

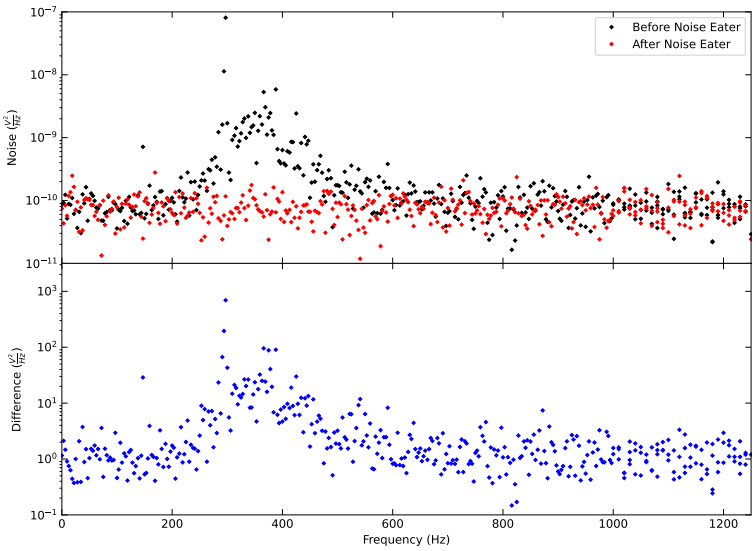


Figure 4.13: PSDs of the output before and after the noise eater as well as the difference between them.

The custom detector was used as the NE p.d., as shown in figure 4.12, thus was connected to the lock box input. The PID values of the lock box were then optimised for reduced noise. The power of each of the monitoring detectors was then set to (7.5 ± 0.01) mW and the power on the NE p.d. was measured as 25 mW. The laser power exiting the system was 1.045 W, which corresponded to an AOM transmission efficiency of 40.4%. The noise power before and after the NE was measured using the oscilloscope, with a time step of 10 ms. Power spectral densities (PSDs) were taken of this data and the results of this are shown in figure 4.13.

As can be seen, the system works! A clear improvement can be seen over the $200-600Hz$ band. Over this band, a broad peak with a magnitude of is present before the NE, but not after. There is an especially narrow peak at $\sim 300Hz$ with a magnitude which is removed too. By looking at the difference between the the before and after PSDs it can be seen that the peak noise reduction is around 30 dB (or 1000 times).

4.7 Conclusion

In this section, the construction and successful implementation of a low frequency laser intensity noise eater has been demonstrated. A final peak noise reduction of 30 dB was recorded on beams at $\sim 7.5mW$. This was achieved using a custom detector that allowed the use of an intense feedback beam.

The hope is that such a noise reduction will help to remove the classical noise that has thus far interrupted efforts to detect the displacement of squeezed regions, particularly when using the high speed PIXIS camera. This is encouraged by the fact that the majority of the removed noise was in the $200 - 600Hz$ band, which roughly corresponds to the frequency of slice taking within a frame. This should stabilise the power between slices of the same frame.

Further refinements could potentially be made by updating the PID circuitry with modern lower noise components. Of course, more feedback power would also increase the noise suppression, and this could be achieved by stringing multiple custom detectors together. Overall, the system has been demonstrated to work and there is more room for improvement should more noise reduction become necessary.

Part III:

Propagation Effects in an Extended Optical Amplifier

CHAPTER 5

LATERAL DISPLACEMENT OF BRIGHT PROBE AND CONJUGATE BEAMS

IT has been discussed that the finite length of the gain medium limits the minimum size of the correlated region. This is referred to as the coherence area. A possible additional displacement effect was also discussed, which would explain the excess noise at intermediate spatial frequencies.

It is then postulated that the small angle between the probe and conjugate could be responsible for this shift. In the optical amplifier equations, it can be seen that the probe and conjugate beams stimulate each other's growth. This leads to correlations at the quantum level. However, the finite angle between them because of the phase matching condition, tends to pull these correlations in the transverse direction. This effect is possibly inhomogeneous across the pump beam.

This chapter produces a working theory of this effect, as well as two numerical simulations that allowed the prediction of some of its characteristics. Further, this chapter quantifies

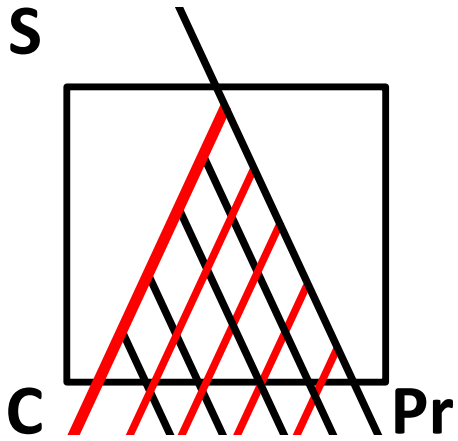


Figure 5.1: An idealised representation of the 4WM system within the cell.

and measures this effect with experiment, demonstrating that it behaves as predicted by the models.

5.1 A Potential Mechanism of Action

Picture an idealised 4WM setup. One where the pump beam is perfectly planar, and the seed is infinitesimal in width and incident at a shallow angle as it enters the cell. Such a system is represented in figure 5.1. As the seed travels it stimulates 4WM interactions, producing both probe and conjugate photons. This causes gain on the seed, which becomes the probe. At the same time, the conjugate beam starts to form. The conjugate beam also stimulates 4WM interactions and thusly gains, whilst causing more gain on the probe too. From looking at the diagram, it might seem obvious that where there is more overlap on the beams there will be more interactions back and forth and more gain. Therefore, the beams would tend to 'lobe' towards the centre point between them, the displacement between them perhaps reducing as the overall gain of the 4WM medium increases.

The effects of loss on the system are harder to imagine, but it would likely lead to

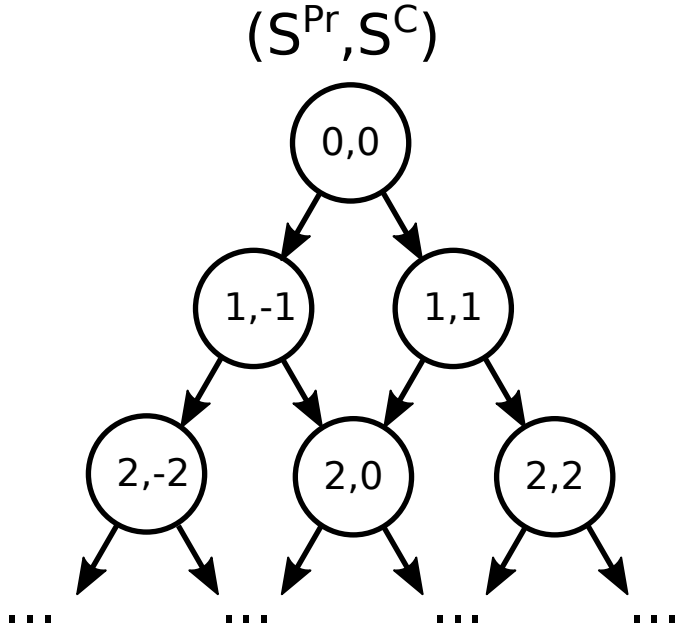


Figure 5.2: A nodal representation of the 4WM system within the cell.

some change in the differential displacement too. To more thoroughly explore this, a mathematical model and simulation was produced.

First, the cell itself was discretized into a diagonal grid and interactions were assumed to occur only on the intersections of said grid. This produces an arrangement similar to the black squares on a chessboard, another representation is shown in figure 5.2. Having an inherent diagonality in this model is convenient, as it builds in the (nearly) horizontal reflection in the propagation vectors of the probe and conjugate beams. The grid angle is set such that it matches the propagation angles of the probe and conjugate beams.

At each intersection, (i, j), a vector can be defined

$$\begin{pmatrix} Pr_{i,j} \\ C_{i,j} \end{pmatrix} = \begin{pmatrix} g^{Pr} C_{i-1,j-1} + l^{Pr} Pr_{i-1,j-1} \\ g^{C} Pr_{i-1,j+1} + l^{C} C_{i-1,j+1} \end{pmatrix}, \tag{5.1}$$

where $Pr_{i,j}$ and $C_{i,j}$ are the probe and conjugate powers. Equation 5.1 also includes the rules for propagating these powers forwards while considering the effects of the gain and

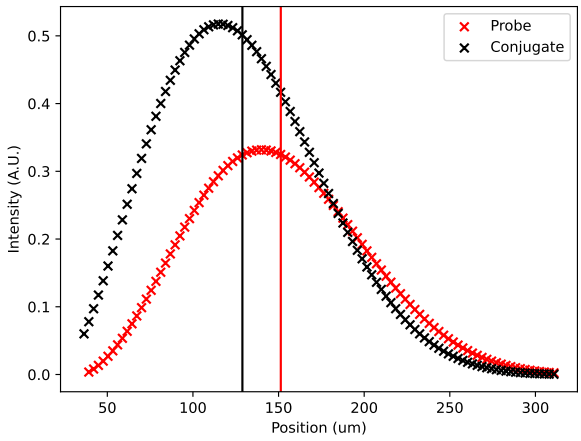


Figure 5.3: The result of a simulation produced using a seed value of $(0, 1)$, assuming negligible conjugate loss. 100 longitudinal steps were taken, where $g^{Pr} = g^{C} = 0.06$, $l^{Pr} = 0.95$, and $l^{C} = 1$. The final total probe gain was 15 and the final total conjugate gain was 22. The coloured vertical lines represent the weighted mean position of the beams. The asymmetry of the final probe and conjugate profiles comes from the fact that the probe experiences loss while the conjugate does not.

loss on the beams at each point, $g^{Pr,C}$ and $l^{Pr,C}$.

A seed power can be introduced at point $(0, 0)$ and the simulation allowed to tick forward a number of steps, dictated by the longitudinal precision required. A result of one of these simulations is shown in figure 5.3, for a virtual cell length of $20mm$.

It can be readily seen that, despite the initial 'infinitesimally' sized seed, the final probe and conjugate beams become significantly broadened by the time they leave the cell. They are also clearly in different positions. Without any background, since this is a simulation, the weighted mean position of the beams was taken and compared. In this case, a displacement of $22\mu m$ is reported, well within range of those seen in the previous experiment.

Further, many of these simulations were run while changing only the gain parameter. This almost perfectly simulates changing the temperature of the cell, since this tends to only change the number density hence the gain per unit length of the cell. To a lesser

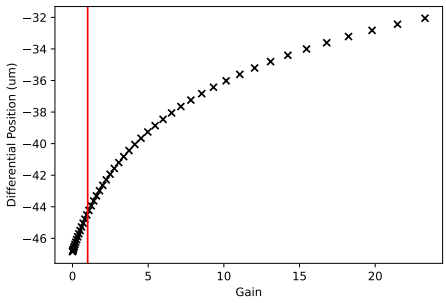


Figure 5.4: The resulting displacements seen in a series of simulations produced using a seed value of $(0, 1)$ in a lossless scenario. 100 longitudinal steps were taken, where $g^{Pr} = g^{C}$ was swept between 0 and 0.04 in equal increments, and $l^{Pr} = l^{C} = 1$. The coloured vertical line represents a gain of 1.

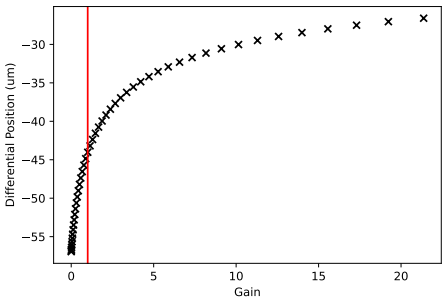


Figure 5.5: The resulting displacements seen in a series of simulations produced using a seed value of $(0, 1)$, in a lossy scenario. 100 longitudinal steps were taken, where $g^{Pr} = g^{C}$ was swept between 0 and 0.0525, and $l^{Pr} = 0.975$ and $l^{C} = 1$. The coloured vertical line represents a gain of 1.

extent, this can represent changing the pump power, so long as the light shift is minimal; otherwise this will impact the gain and loss terms simultaneously as 4WM resonance frequencies change. Two examples of this simulation are shown in figures 5.4 and 5.5.

Figure 5.4 shows a simulation that does not consider loss at all. Despite this, a significant displacement is seen as the probe gain increases. It also plateaus similarly to that seen experimentally, in the case where the gain change is caused by changing pump intensity across the cell. This is shown later in this chapter. It is as though the probe and conjugate segments are 'locked' together at higher gains. This is very similar to a phenomenon noted in the time domain studied previously. [102]

Figure 5.5 displays a similar scenario with some constant loss considered too. In this instance, the plateau is even more strikingly similar to that seen experimentally in the following sections. More so, the range of relative displacements is $30um$ - very close to the experimental values.

Interestingly, other more complicated effects can be produced too. For instance, figures

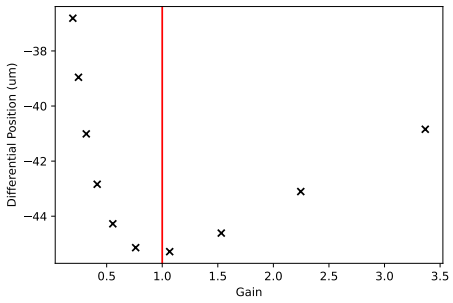


Figure 5.6: The resulting displacements seen in a series of simulations produced using a seed value of $(0, 1)$. 100 longitudinal steps were taken, where $g^{Pr} = g^{C} = 0.011$ and $l^{C} = 1$, and l^{Pr} was swept between 0.94 and 1 in equal increments. The coloured vertical line represents a gain of 1.

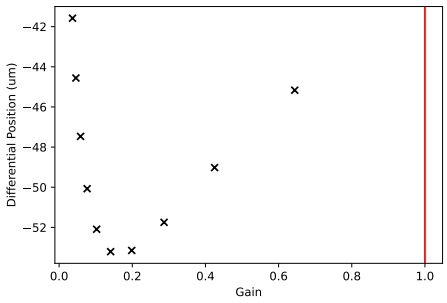


Figure 5.7: The resulting displacements seen in a series of simulations produced using a seed value of $(0, 1)$. 100 longitudinal steps were taken, where $g^{Pr} = g^{C} = 0.022$ and $l^{C} = 1$, and l^{Pr} was swept between 0.94 and 1 in equal increments. The coloured vertical line represents a gain of 1.

5.6 and 5.7 show an inflection point in the dynamics. These sweeps are produced by holding the gain constant and sweeping the loss. This indicates that the loss on the system can both enlarge and reduce the differential displacement in a complex way, that depends on the gain too.

5.2 A More Refined Model

Further, developing this model and bringing it closer to reality, more aspects can be included from the 4WM process. For this model, we rely on the propagation equations defined in the semi-classical model in section , equations 1.101 and 1.102.

Initially, we transform to Fourier space as a way of dealing with the x derivative in these equations, which is the rate of change of the beam profile transverse to the propagation

direction. For the probe this is given as

$$\varepsilon_{Pr}(x,z) = \int_{-\infty}^{\infty} \tilde{\varepsilon}_{Pr}(k_x,z)e^{ik_x x}dk_x. \tag{5.2}$$

In the case of the conjugate term, the complex conjugate of the Fourier transform must be taken instead, this is used in equation 1.102. This is

$$\varepsilon_{C}(x,z) = \int_{-\infty}^{\infty} \tilde{\varepsilon}^{*}_{C}(-k_x,z)e^{ik_x x}dk_x. \tag{5.3}$$

These cause equations 1.101 and 1.102 to become

$$-k_x^2\tilde{\varepsilon}_{Pr}(k_x,z) + 2ik_{Pr}\frac{\partial\tilde{\varepsilon}_{Pr}(k_x,z)}{\partial z} = -k_{Pr}^2\chi PrPr\tilde{\varepsilon}_{Pr}(k_x,z) - k_{Pr}^2\chi PrC\tilde{\varepsilon}^{*}_{Pr}(-k_x,z) \tag{5.4}$$

and

$$-k_x^2\tilde{\varepsilon}^{*}_{C}(k_x,z) - 2ik_{C}\frac{\partial\tilde{\varepsilon}^{*}_{C}(-k_x,z)}{\partial z} = -k_{C}^2\chi CC^{*}\tilde{\varepsilon}^{*}_{C}(-k_x,z) - k_{C}^2\chi CPr\tilde{\varepsilon}_{C}(k_x,z). \tag{5.5}$$

These are first order coupled differential equations, of the same form as those seen in section 1.1.3 and can be solved by the matrix method in much the same way. This produces

$$\tilde{\varepsilon}^{*}_{C}(k_x,z) = -\tilde{\varepsilon}_{s}(-k_x)e^{\delta az}\frac{a_{CPr}}{\xi}sinh(\xi z) \tag{5.6}$$

and

$$\tilde{\varepsilon}_{Pr}(k_x,z) = \tilde{\varepsilon}_{s}(k_x)e^{\delta a}(cosh(\xi z) + \frac{a}{\xi}sinh(\xi z)). \tag{5.7}$$

Which are the propagation equations for probe and conjugate plane waves in k-space, given an initial probe seed wave $\tilde{\varepsilon}_s(k_x)$, where $\delta a = \frac{1}{2}(a_{PrPr} - a_{CC})$, $\xi = (a^2 - a_{CPr}a_{Prc})^{\frac{1}{2}}$, $a = \frac{1}{2}(a_{CC} + a_{PrPr}) - \Delta k$, $\Delta k = \frac{ik_x^2}{2k_{Pr}} = \frac{ik^2}{2k_C}$, $a_{PrPr} = \frac{ik_{Pr}}{2}\chi_{PrPr}$, $a_{PrC} = \frac{ik_{Pr}}{2}\chi_{PrC}$, $a_{CPr} = \frac{ik_C}{2}\chi^{*}_{CPr}$, and $a_{CC} = \frac{ik_C}{2}\chi^{*}_{CC}$.

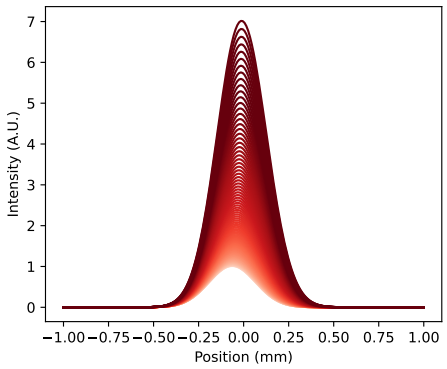


Figure 5.8: The resulting probe intensity profiles seen in a series of simulations produced using a $\chi_{PrPr} = 0.15 + 0.0i$. 100 steps in χk were taken, over a range of 0 – 0.17 rad mm^{-1}. Darker plots represent an increasing value of χ and gain.

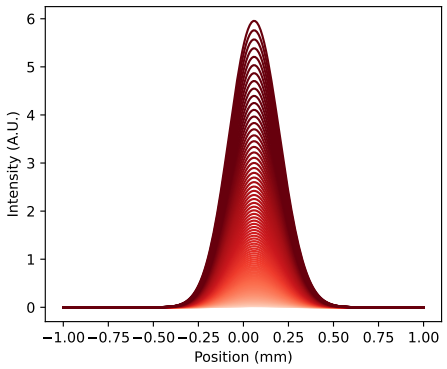


Figure 5.9: The resulting conjugate intensity probe profiles seen in a series of simulations produced using a $\chi_{PrPr} = 0.15 + 0.0i$. 100 steps in χk were taken, over a range of 0 – 0.17 rad mm^{-1}. Darker plots represent an increasing value of χ and gain.

Using these equations, an initial seed can be converted to the Fourier domain and propagated here by some distance, z. After, the profiles of the probe and conjugate in real space can be found by taking the inverse Fourier transform. Propagating the beams in k-space in this way is especially useful, as it allows us to account for how different Fourier components of the beams experience different phase matching conditions.

This was done numerically using python code written by the group previously, and the results of this for a seed beam with a waist of $0.36mm$ over a sweep of $\chi k = \chi_{PrC} k = \chi_{CPr} k$ are shown in figures 5.8 and 5.9. χ_{PrC} and χ_{CPr} were set to be both entirely imaginary and equal, as this is what is expected for these parameters in most cases where squeezing is observed. These simulations were run with $\chi_{CC} = 0$ and $\chi_{Pr} = 0.15$, indicating 0 absorption for both terms and a refractive index on the probe. Again, this is what is expected in situ for χ_{CC} however there are some cases where probe absorption is significant. This is investigated later.

It is immediately clear from the figures that while the conjugate beam grows uniformly

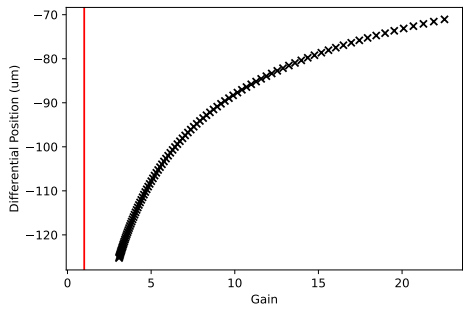


Figure 5.10: The resulting displacements seen in a series of simulations produced where $\chi_{PrPr} = 0.15 + 0i$, so there was no loss on the probe. The gain was changed by altering χk over a range of $0 - 0.17$ rad mm^{-1}, over 100 equal increments. The red line represents a gain of 1.

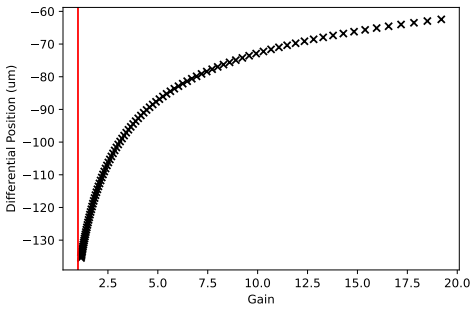


Figure 5.11: The resulting displacements seen in a series of simulations produced where $\chi_{PrPr} = 0.15 + 0.05i$, such that there was loss on the probe. The gain was changed by altering χk over a range of $0 - 0.20$ rad mm^{-1}, over 100 equal increments. The red line represents a gain of 1.

and maintains its position with changing gain, the probe beam grows in a much more asymmetric way. Specifically, it lobes on the side towards the conjugate beam as the gain increases.

This is reflected in plot 5.10, which represents the distance between the mean positions of the probe and conjugate beams at each probe gain. It is clear to see that the beams start fairly separated at low gains. This is because of the geometric propagation in the cell, as the transversely opposite k vectors of each of the beams causes them to propagate away from each other. However, as the gain increases, the probe beam is drawn towards the conjugate. This trend starts to plateau at higher gains, 'locking' the positions of the beams together. Further, this trend is seen even more strongly when some loss is introduced to the system, as seen in figure 5.11. Both a larger magnitude is seen in the effect and the plateau is stronger too.

All of these features are consistent with what is seen in the previous model in figures 5.4 and 5.5, as well as the magnitudes of the effect in both cases and the general form of the

curves produced. This evidences that the dominant cause of the displacement effect is the gain and loss on the system, as this was the only aspect considered in the previous model.

Overall, these simulations do offer compelling evidence that this theory could be the mechanism of action for a displacement effect. What remains to be seen is whether, in a MSM squeezed imaging system, it would be easier to simulate these displacements before imagining and account for them that way, to simply measure the displacements in situ before imaging and correcting using that, or even to account for and mitigate them optically – before imaging.

5.3 Beam Scan Investigation

The first of the experiments seeking to validate the previous simulations was the beam scan experiment.

In this study, the positions of the probe and conjugate beam positions were measured as the position of the input seed beam was changed relative to the pump within the gain medium so that it assumes all possible horizontal positions of the pump. In this way, the seed was scanned across the pump, hence the name 'beam scan' experiment. The aim was to prove that the inhomogeneity of the pump profile was a component of the differential displacement in the correlated regions of the probe and conjugate beams that was potentially preventing the acquisition of high-quality MSM squeezed images. Given that this was the case, this would pave the way to future experiments aiming to more precisely map the differential displacement of the beams and extract a function that could be used to rectify the images taken by the camera.

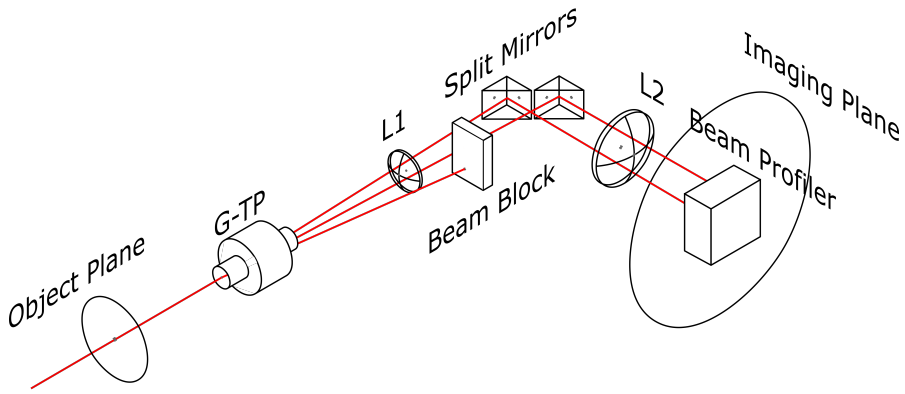


Figure 5.12: The 4F imaging system used in the beam scan experiment.

5.3.1 Method

The general idea was to measure the relative position of the output beams, as a function of the seed's position within the pump. This was done in the case of beams much smaller than those usually used for multimode squeezing when focused to the centre of the cell. Thus, the diameter of the beam waist of the Seed beam was altered to be approximately $240\mu m$. The goal was to make the displacement comparable to the size of the coherence area. For this, ideally, we would use the smallest beam possible, one that has a Rayleigh range comparable to the cell length. This would make the beam size equal to the coherence area. However, the Rayleigh range of this beam is closer to $0.2m$. This had to be the case, as otherwise the twin beams would diverge too much upon exiting the cell and overlap with the pump before they could be picked off for measurement.
Rather than displacing transversely the probe, we chose to shift the pump beam sideways instead, for practical reasons.
Firstly, the input Seed and Pump beams were combined at a small angle with a PBS and injected into a $20mm$ cell. Here, four wave mixing occurs, and a conjugate beam was generated. All system parameters were the tuned to those optimal for squeezed state generation. A $20mm$ length cell was used here instead of the typical $12.5mm$ one

to increase the path length the beams gain over and thereby maximise any propagation effects. After this, two lenses are positioned in a 4F arrangement, such that the EM field at the surface of the cell is exactly replicated in the second near field with a 3x magnification. Here, a Thorlabs BC106N-VIS(/M) beam profiler captures an image of the beams. This is shown in figure 5.12.

To separate the beams, so both can be independently seen on the beam profiler, a split mirror is placed in the Fourier plane. Its two elements were angled such that the probe and conjugate travelled slightly different paths through the system and landed separately on the beam profiler CCD, despite them being in the imaging plane.

The pump was mostly removed using a Glan-Thompson Polariser, and spatial filtering in the imaging system (a beam block in the Fourier plane). To further reduce pump impact, subtraction imaging was also implemented; so two images were taken at each position, one with the probe seed blocked before the cell and one where it is not blocked. This allowed the pump remnant to be isolated and subtracted from the combined image.

The beam positions were determined from the subtracted images by curve fitting, with a Gaussian function. Previous testing, with a resolution target, determined the resolution of the imaging system was around (12 ± 2) μm. This is much smaller than the shifts seen in the results, so this precision is deemed appropriate. Errors were also considered to be much lower than this, as peaks can typically be located much more precisely than the resolution of a system would indicate [103].

The PBS before the cell, as shown in figure 2.2, was moved side to side using a micrometer-driven displacement stage, changing the position of the pump beam in the cell with a $\sim 10\mu m$ accuracy.

Gain was calculated by dividing the total beam power seen on the beam profiler by the seed power before the cell. It was important to measure this, as the gain at each position can be seen as a proxy for the pump intensity. Since only this aspect of the system is

changing at each point. So if the displacements are related to gain in this case, it can be said that the local pump intensity is responsible for them. The seed power was calculated from the reading given by the photodetector, as the PBS used to pick off the beam here divides its intensity by a known fraction determined at the start of the experiment. It was then assumed to remain constant throughout. In both cases, the readings were taken over a 10-second measurement period and averaged.

5.3.2 Results and Discussion

Initially, the gain of the probe and conjugate beams were plotted against the pump position as it was moved across the cell, shown in figures 5.13 and 5.14. This produced the expected result that the gain of each beam varies with the pump power.

The reliability of these results was measured by plotting the seed beam power as the experiment progressed. The RMS of this was then taken and divided by the mean of the seed power to show a relative fluctuation estimate of 2.56×10^{-3} for a single point. This error was propagated to the gain in each graph, to produce error bars that account for the uncertainty introduced by a fluctuating probe seed beam. These were so small as to be considered insignificant. However, it has previously been determined that frequency drift in the initial beam can be a significant source of error, producing a drift in gain of approximately 0.1. As such, this was also considered in the calculation of the error.

Finally, the peak positions of each beam were plotted against pump displacement. This is shown in figure 5.17.

The most striking feature of this graph is the disparity between the conjugate beam, which seems to move very little, and the probe, which displaces by almost $50\mu m$ at its maximum.

By subtracting the relative positions of each of these beams (figure 5.18) a relative dis-

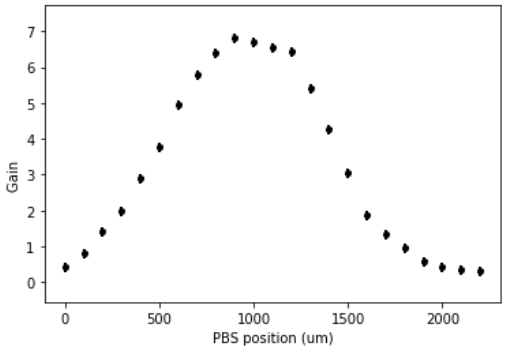


Figure 5.13: The probe Gain vs. Seed position along the cell.

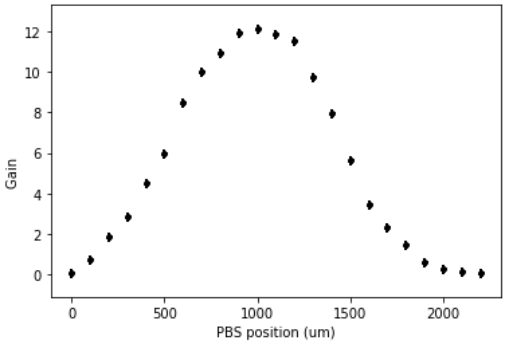


Figure 5.14: The conjugate Gain vs. Seed position along the cell.

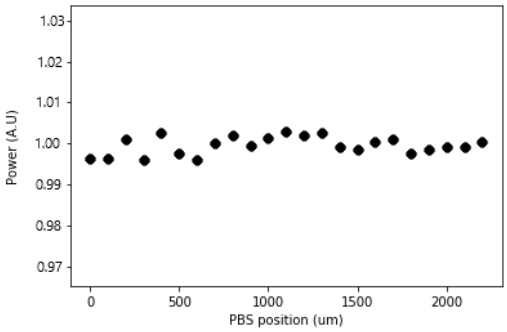


Figure 5.15: The probe Seed intensity vs. Seed position along the cell.

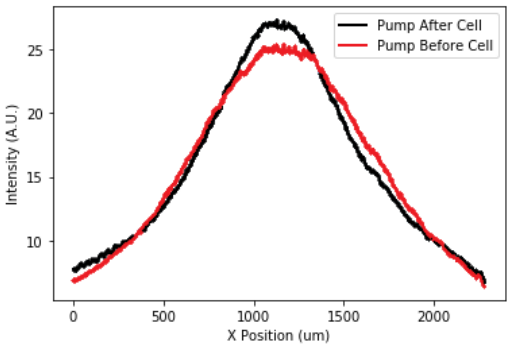


Figure 5.16: Horizontal cross-section of the pump beam intensity.

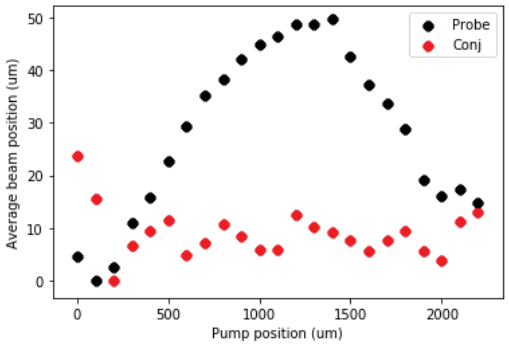


Figure 5.17: Peak positions of the probe and conjugate vs. Seed position along the cell.

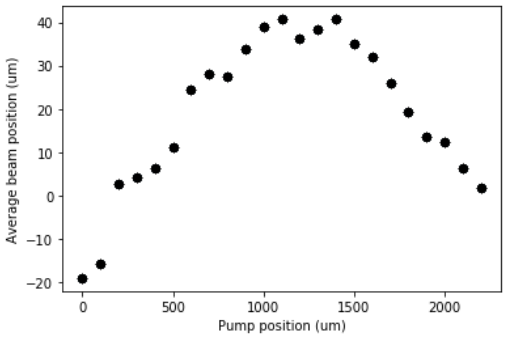


Figure 5.18: Relative displacement between peak positions of the probe and conjugate vs. Seed position along the cell.

placement map can be produced.

5.4 Elliptical Beam Investigation

To complement the previous investigation, it was decided that the displacement effect needed to be explored over the full parameter range of the 4WM resonance. It was also desired that the full range of the pump intensities that the probe and conjugate beams would be exposed to was explored simultaneously. This offered the benefit that any measurements of the displacements made would not be susceptible to fluctuations on the pump beam over time.

To achieve this, the seed beam was modified to be much wider in the axis perpendicular to the angle between the pump and seed beams. The idea here being that it was made wide enough that the seed extended from outside the influence of the pump, directly through the centre of it, and then back out of its influence on the other side. Having regions of the seed outside the pump also provided an absolute reference for the seed position, unperturbed by the effects of the pump. Slices of equal pump intensity of the resulting beams were then taken, and the position of each slice was compared to the reference positions to determine the magnitude of any displacement seen.

It was important that each slice only sampled a very narrow range of pump intensity, so it could be assumed that the pump was constant. For this reason, the slices had to be very thin. Its relatively small extent in the vertical axis also made it easy to measure the translation of the beam caused by the 4WM process.

5.5 Experimental Preparations

5.5.1 Producing an Elliptical Seed and Taking Real-Time Seed Power Measurements.

As detailed in figure 5.19, the Seed beam was shaped and steered with an arrangement of lenses and mirrors to ensure its focus was placed exactly in the centre of the cell with a beam waist of $250\mu m$ in the vertical direction. Cylindrical lenses were added to expand the beam in the horizontal direction. The setup remained functionally identical in the vertical axis to that shown in section 5.3, but two $f = 25mm$ cylindrical lenses were inserted in the horizontal direction. This was done because the cylindrical lenses were easier to mount in this orientation. This resulted in the beam being very slightly converging 0.5mrad and approximately $1500\mu m$ wide at the cell centre.

We were interested in measuring the gain of all the slices at all positions in the pump beam, so this could be plotted alongside the probe and conjugate displacements as a way to validate our proposed model. For this, the power of the beams before and after the cell had to be measured. Real-time measurements of the seed power were required to compensate for any fluctuations in the overall beam power fed into the experiment. Measuring the power of the seed beam was achieved by adding a 50 : 50 beam splitter between mirrors M3 and M4 and focusing the deflected output on a photo detector. After the system was calibrated using a trusted power-meter. Imaging and measurement of the beams after the cell is discussed in section 5.5.3.

The final system is shown in figure 5.19.

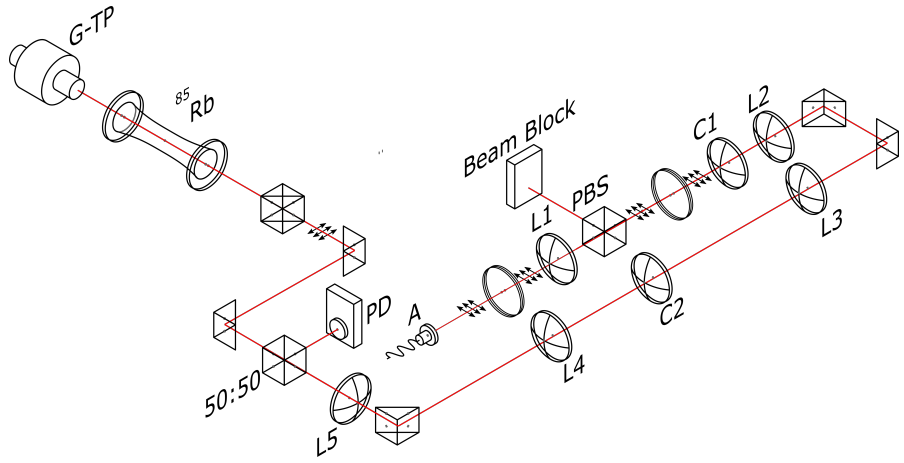


Figure 5.19: The final setup of the post fibre Seed prep for the elliptical beam experiment. The focal length of the spherical lenses used are; $L1 = 100mm$, $L2 = 50mm$, $L3 = 50mm$, $L4 = 200mm$, and $L5 = 500mm$. The cylindrical lenses both have a focal length of $C1 = C2 = 25mm$

5.5.2 Achieving 4WM and Measuring the Angle of Incidence Between the Pump and Probe Beams

Due to the seed being expanded in the horizontal direction, the seed needed to be injected into the cell at an angle along the vertical plane, instead of the usual horizontal plane. However, this should not have produced any difference in the results, since the vapour density in the cell was isotropic. The obvious generation of two beams (probe and conjugate) was enough to confirm that 4WM was occurring, and the Seed had been sufficiently aligned to the phase matching condition.

After this, the probe and pump beams were allowed to propagate from the unheated cell by a known distance to a screen. The distance between the two beams was then measured and the angle between them calculated to be (6.9 ± 0.2) $mrad$.

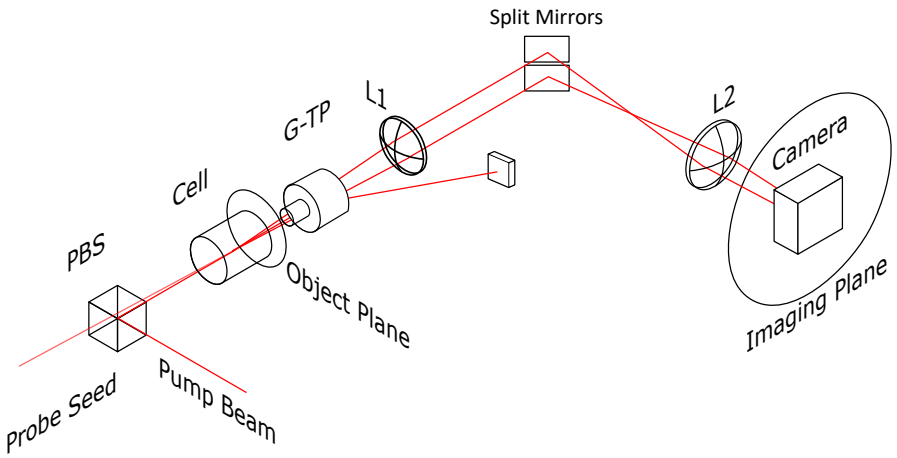


Figure 5.20: The $2F - 2F'$ imaging system used in the experiment.

5.5.3 The $2F - 2F'$ Imaging System

To image the beams on the output surface of the cell, the intensity distribution had to be replicated exactly (aside from magnification) on the detector used to measure it. In this case, it was a Thorlabs BC106N-VIS(/M) beam profiler. This transfer was achieved using a simple $2F - 2F'$ imaging system similar to the one used in the previous experiment, shown in figure 5.20. This produced a 3x magnified image at the imaging plane.

It can be seen that the system consisted of two lenses separated from each other by the sum of their focal lengths. The first lens, $L1$, was one focal length from the cell, as the beam profiler was one focal length from $L2$. The focal lengths of $L1$ and $L2$, are $250mm$ and $750mm$ respectively.

Between $L1$ and $L2$ at the focus of both lenses a pair of split mirrors were placed (one on top of the other), which allowed the steering of the probe and conjugate independently, so each could be separated and imaged on the detector at the same time. Otherwise, they would be on top of each other in the imaging plane.

To ensure accurate calibration of the recorded magnification of the final images, the

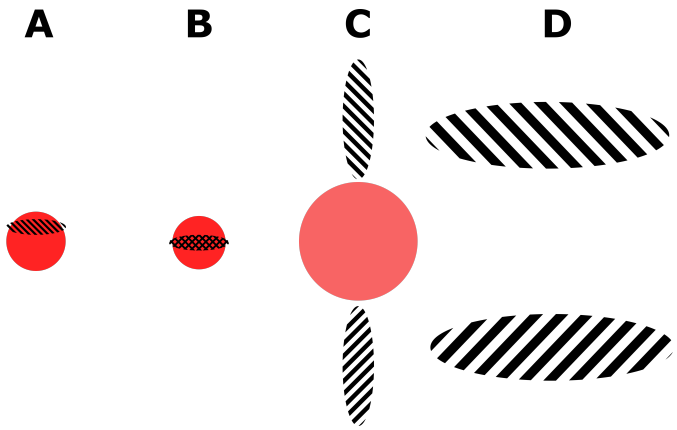


Figure 5.21: A representation of the beam profiles at various points in the experiment. A) Initially, the oppositely polarised pump and probe seed beams combine at the PBS, shown in figure 5.20. B) After, they are focused to the centre of the cell where 4WM occurs, producing gain on the probe and generating the conjugate beam. Hence, all three beams are present in the object plane. C) The beams are then transported to the Fourier plane by lens $L1$. Here, most of the pump has already been removed by the G-TP, but the rest passes between the split mirrors. The long and short axes of the probe and conjugate beams are switched due to diffraction effects. D) Finally, the probe and conjugate are projected onto the imaging plane by $L2$ with a magnification factor of 3x.

magnification of the system was determined by illuminating a resolution target of known size (1951 USAF resolution test chart) with the pump beam and capturing an image of it. The target was placed at the point that the cell surface would occupy in the final experiments, and the correct scaling factor was thusly calculated.

A diagram of the beams as they pass through the system is shown in figure 5.21

5.5.4 Measuring Pump Beam Stability

To ensure it would not be a significant source of error for the calculation of local gain, the stability of the pump beam was measured over the course of 100 minutes. This was done by blocking the seed and slightly tilting mirror M1 such that the pump fell onto one of the split mirrors. This allowed it to be imaged by the 4F system and seen by the

beam profiler. After, an image of the pump was taken every 10 minutes. Then, each of the images were fitted to 2D Gaussian functions and the amplitude, mean positions, and beam diameters of these fitted Gaussians were plotted over time.

As a result of this analysis we saw that the pump's intensity varies very little over the allotted time, having a relative error of less than 0.2%. Thus, it is not considered to be a large source of error in the results.

Further it was seen that the position in both the x and y-axis varied very little over the 100 minute period, resulting in a standard error on the pump position of $3.25\mu m$ and $1.28\mu m$ in the x and y directions respectively.

The variation in the beam diameter was considered insignificantly small also, being less than $1\mu m$ in each case. This could have easily been caused by noise on the beam profiler itself interfering with the Gaussian fitting process. The average beam diameter was found to be $1661\mu m$ and $1708\mu m$ in the x and y axes.

5.5.5 Calculating an Accurate Gain for Vertical Slices of the probe and conjugate Beams

The image data of the probe and conjugate beams was analysed by first slicing it into 100 thin vertical segments.

To calculate a gain for each part of the resultant probe and conjugate beams an image of the probe seed beam was taken when far from the 4WM resonance to produce a known profile of the seed. This was sliced into 100 even segments. Then, the power of the overall seed beam was measured using P.D.2 (shown in figure 5.20) and each slice was assigned a portion of this power in accordance with the relative intensity of the slices on the original image.

To calculate the gains from the final experimental data, the power of the probe and

conjugate beams was calculated for each slice of the images and they were divided by the previously calculated seed slice powers.

5.5.6 Determining the Increments of 1-Photon Detuning Used

The 1-photon detuning was controlled by adjusting a reference cavity attached to the SolsTiS Ti:Sapphire laser. This was done using a piezoelectric crystal. To produce an accurate measurement of the step size used in the experimental sweeps, the wavelength of the seed beam was measured using a Moglabs Economical Wave meter over 35 increments. A linear line was fitted to the results, which determined the step size to be $1.42 \times 10^{-4} nm$. Residuals on this fit were so low that any error on this was deemed insignificant. This step size corresponds to $\sim 67 MHz$ as a frequency, in the regime we are working in.

5.5.7 Method

To fully explore the parameter range of the 4WM, four key aspects needed to be swept over 1-photon detuning, cell temperature, total pump power, and 2-photon detuning. Sweeping the 1-photon detuning was accomplished using the cavity described earlier, and the cell temperature was swept by simply turning off the cell heater and taking measurements as it cooled. The total pump power was adjusted using the pump AOM. The 2-photon detuning was adjusted with the $1.5 GHz$ probe AOM running in double pass configuration, by altering the frequency of the incoming RF signal.

First, the probe beam was aligned such that its centre intersected with the peak of the pump beam, whilst some portion of it on either side was entirely clear of the pump. Then the parameters not being swept were set or recorded to be the values in table 5.1.

The blue-detuning referenced in table 5.1 is the frequency of the 1-photon detuning rela-

Table 5.1: The values of each static parameter for each parameter sweep. The blue-detuning is relative to the point of maximum gain of the 4WM, which not the 1-photon detuning resonance. In actuality, the absolute 1-photon detuning is on the order of 1 GHz from the resonance.

Scan	1P.D.(MHz)	Temp.(C)	P.P.(W)	2P.D.(MHz)	Seed P.(V)
1 P.D.	NA	106	1.2	8	3.3
Temp.	250 → blue-detuned	NA	1.2	8	3.5
Pump Power	250 → blue-detuned	106.3	NA	8	3.26
2 P. D.	250 → blue-detuned	105.8	1.2	NA	4.0

tive to its value at the maximum 4WM gain. This not the 1-photon detuning resonance. In actuality, the absolute 1-photon detuning is on the order of 1 GHz from the resonance. First the probe gain is optimised to its maximum value and then the 1-photon detuning is stepped 250 MHz blue-detuned.

For each sweep, at each increment, an image of the two beams was captured, using a CCD beam profiler like in the beam transit experiment. Another image was also captured with the seed beam blocked before the cell. This provided a profile of the pump remnant, that made it through the various filtering methods in the system. This profile was then subtracted from the original image to reduce the error from this effect, as well as the influence of the background noise. This produced a series of noise reduced images ready for further analysis.

After this, the images were sliced into 100 even segments in the vertical direction. The segments were then averaged in the horizontal direction to produce 100 $1D$ strips, all at different points along the beams. A Gaussian function was then fit to these data. The mean positions of each of these Gaussians were then plotted as a function of the pump beam at each point. This information was used to see how the probe beam moved as compared to its initial undisturbed position, as well as the differential displacement between probe and conjugate segments. A diagram of this process is outlined in figure 5.22.

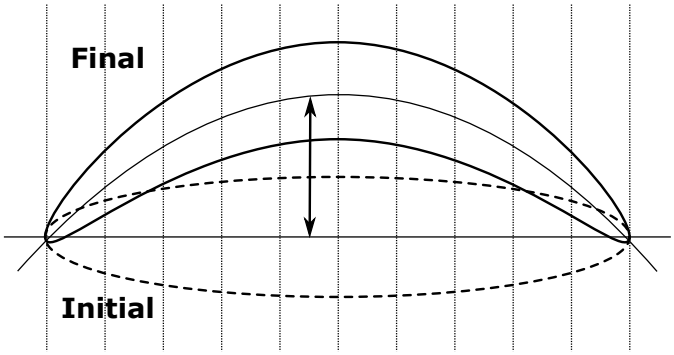


Figure 5.22: A diagram showing the process of cutting the beams into vertical sections, averaging each segment horizontally, and then fitting a Gaussian to each segment to find its midpoint. The beam depicted with a solid line is the probe at the exit surface of the cell, and the beam shown in the dashed line is the undisturbed probe seed beam. The vertical slices are divided with straight dashed lines and the midpoint vertical position of each beam is shown with a solid line running through their centres. The displacement in this diagram is greatly exaggerated for illustrative purposes; in reality, the displacement of the beam is tiny (~ 40 μm) as compared to its width (~ 250 μm).

5.6 Results and Discussion

5.6.1 1 Photon Detuning Sweep

The raw results of this sweep are shown in figure 5.23. It can be seen that generally the noise reduction methods outlined above were successful in obtaining clear images of the beams. However, the final few images appear to have a lower SNR, due to the low intensity of the probe and conjugate relative to the background and other noise sources. Beyond this, it is clear in the final 3 images that both the probe and conjugate beams start to split into two. The reason for this is not fully understood, but may be related to the changing absorption and gain parameters of the system as the 1-photon detuning is swept. As a result of this, plotting a well defined beam position becomes very difficult, so these last two images are neglected in the final analysis.

Splitting the images into a hundred vertical slices, the profiles of the probe and conjugate

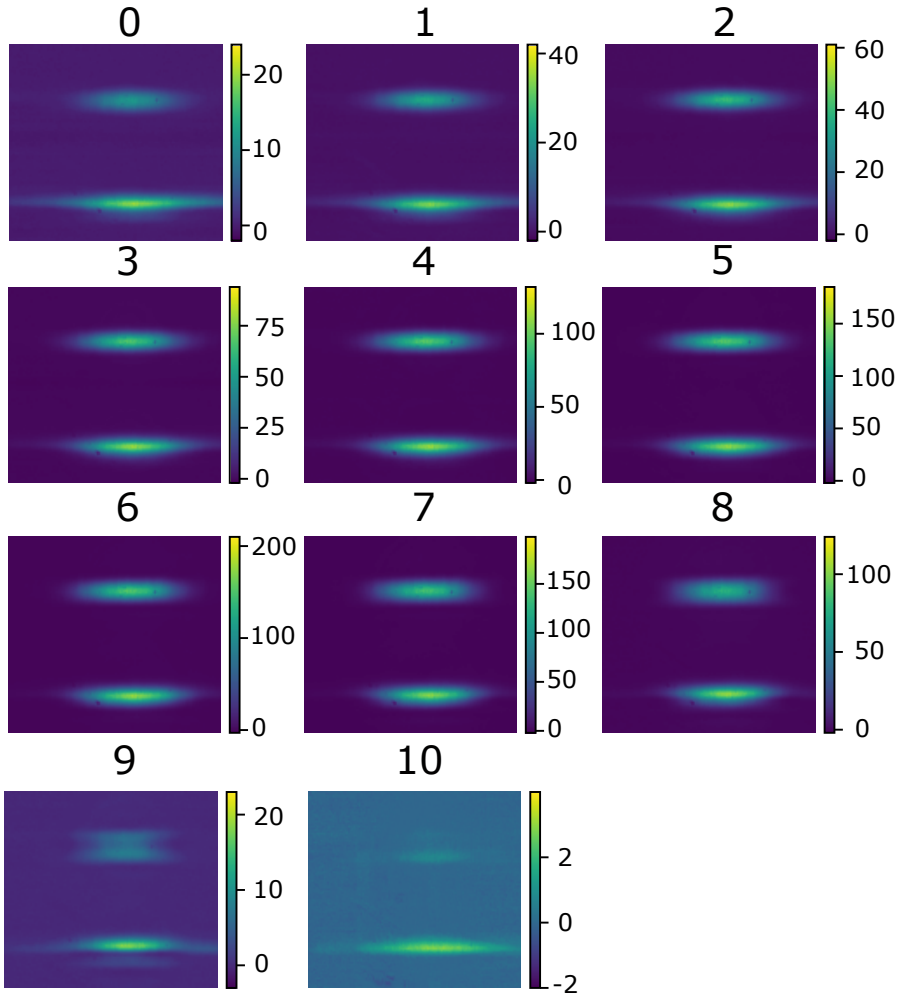


Figure 5.23: The full array of subtracted images obtained in the 1-photon detuning sweep, each increment represents a $\sim 67MHz$ shift in 1-photon detuning. The scale represents the intensity of the beam at each pixel in arbitrary units and the x and y axis are spacial with each pixel in the images representing a pixel on the camera.

can be plotted, the results of this are shown in figures 5.24 and 5.25.

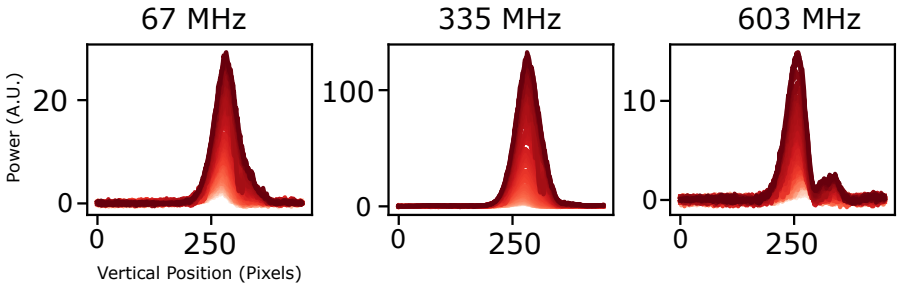


Figure 5.24: The profiles of the probe beam obtained in the 1-photon detuning sweep, each increment represents a $\sim 67MHz$ shift in 1-photon detuning. The 1-photon detuning was swept from a blue-detuned state towards the 4WM resonance. The line colour darkens the closer the slice is to the centre of the beam; hence, each plot represents many regions of differing gain and loss.

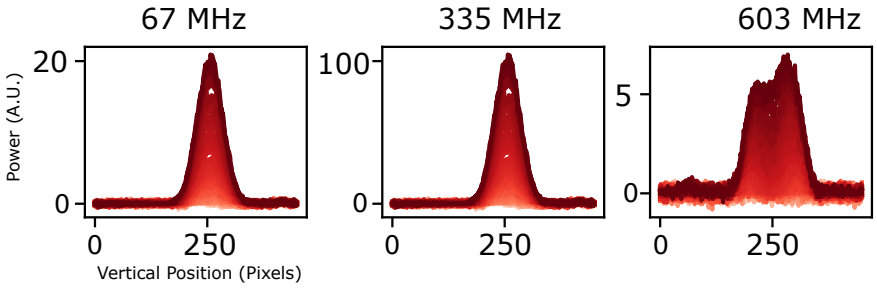


Figure 5.25: The profiles of the conjugate beam obtained in the 1-photon detuning sweep, each increment represents a $\sim 67MHz$ shift in 1-photon detuning. The 1-photon detuning was swept from a blue-detuned state towards the 4WM resonance. The line colour darkens the closer the slice is to the centre of the beam; hence, each plot represents many regions of differing gain and loss.

Looking at the probe profiles, a slight displacement in the position of the profiles closer to the centre of the pump beam can be seen (darker profiles). It can also be seen that they develop a tail on one side. This tail grows as the amplitude of the beam slices increase. Towards the end of the sweep, the probe fragments into two peaks before shrinking and disappearing. However, the secondary peak is much smaller than the primary.

Conversely, conjugate profiles do not seem to shift at all as their amplitude increases. They also do not grow tails as the probe profiles do. However, they fragment much more dramatically. This is obvious in the last image, where the beam splits into two equally intense fragments.

A more enlightening way to look at the data is to map the displacement of each of the beams by fitting a Gaussian to each slice and seeing how their peak positions vary regarding each other. The results of this process applied to the probe and conjugate beams, as well as the difference between the two, is shown in figure 5.26. The right side also displays the gain profiles of the beams, for comparison.

Although the gain graphs could be calculated for the full range of the 1 photon detuning sweep, the fragmentation of the beams meant that peak fitting was not an accurate method for determining the beam translation beyond $600MHz$. As such, the position graphs are clipped at this point. Note that the gain peaks for the probe and conjugate beams were not symmetric along the 1-photon detuning axis. There was a 'slow side' where the gain changes slowly with 1-photon detuning (at the smaller relative detunings) and a 'fast side' where the gain changes quickly with 1-photon detuning (at the larger relative detunings).

What is immediately obvious is that the probe slices move considerably, whilst the conjugate slices remain relatively flat in their peak positions. This is reassuring, since this is a feature that is predicted by the theory used to model this process. Further, the displacements seen on the probe slices increase with their gains, which are in turn influenced by the local intensity of the pump beam. A high pump intensity leads to a high gain, which leads to a more significant probe position displacement. This displacement is in the positive direction when the beams are being drawn towards the pump axis, so the probe and conjugate beams get closer as gain increases.

However, one striking feature on the probe position plot is the dip in position apparent between $400MHz$ and $600MHz$. This is also the point where the apparent gain decreases on the probe gain graph, despite the 1-photon detuning getting closer to the 4WM resonance. In this case, the distance between the beams increases. This is reasoned to be caused by some absorption effect that leads to loss on the probe beam. This draws the

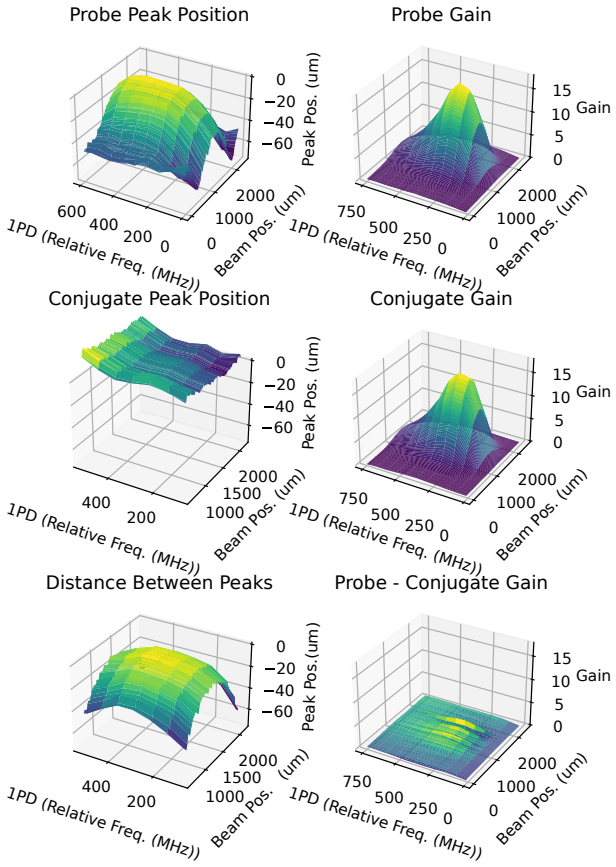


Figure 5.26: The peak position and gain profiles of the beams over the 1 photon detuning sweep. Beam position on the y axis references the position of each slice laterally across the beams. The peak position on the z axis referrers to the mean position of the vertical Gaussians fitted to each slice. The actual positions of each of the peaks are arbitrary, it is the relative positions that matter here. As such, each of the position graphs have been displaced to lie around 0. Positions closer to 0 represent the beams closer together at the cell. Positions shown here are magnification corrected, so represent the magnitude of the actual displacements at the cell.

beam downwards, potentially leading to the beam splitting that was seen earlier. This did not occur on the edges of the beam, which were not pump exposed, so was unlikely to be caused by beam drift. This is further supported by the fact this occurred on the

red-detuned side of the gain profile, which is closer to the 4WM resonance and has been shown already to be a highly absorbing region. [43]

The conjugate beam itself seems very flat, effectively having no translation when exposed to different pump powers (along the beam position side of the graph). However, it does move away from the pump centre as a whole as the 1 photon detuning is moved further from resonance, on the 'slow side' of the gain profile. The edges of this graph had to be clipped in the beam position axis as the conjugate was so weak on the edges there were giant errors on the fitted peak position.

The combined effects on the probe and conjugate beams leads to a significant change in the distance between them when they emerge from the cell. This is almost entirely due to changes in the position of the probe over a range of around $50\mu m$. This is on the 'slow side' of the gain peak, where it is expected that losses play only a minor role. These trends are very similar to those seen in the simulation in figures 5.4 and 5.5. They are also of a very similar magnitude, which helps to validate this model further.

To further investigate the role of the gain on the distance between the probe and conjugate beams, it is better to plot the differential peak positions regarding probe gain. This is done in figure 5.27.

It can be seen that in all cases that the distance between the probe and conjugate slices decreases as probe gain does, above the 1 gain point (red line on the graph). However, below this point the differential peak position also increased. For a gain less than 1 there must be some absorption involved, this could have had a significant effect. Further, this trend is very similar to the effect seen when varying the probe absorption in the simulation, shown in figures 5.6 and 5.6, which further supports this idea. Above a gain of 1, plots themselves are clearly offset from one another.

Plotting just the outline of these displacements, as is done in figure 5.28, reveals that the displacement with gain remains 'locked' in place as gain changes on the 'slow side'

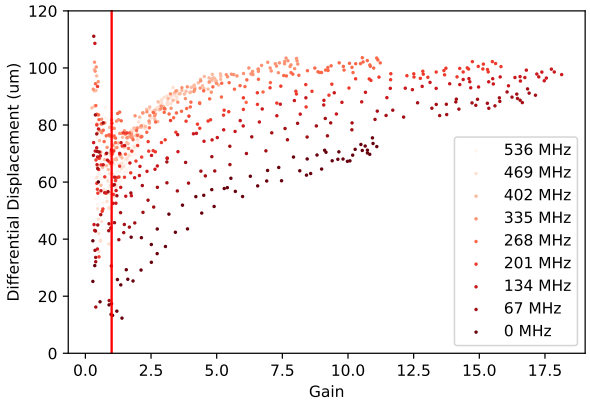


Figure 5.27: The distance between probe and conjugate beam slices vs. gain for each 1 photon detuning increment. The origin in the graph is arbitrary, since the absolute distance between the beams is not known, by the nature of the experiment.

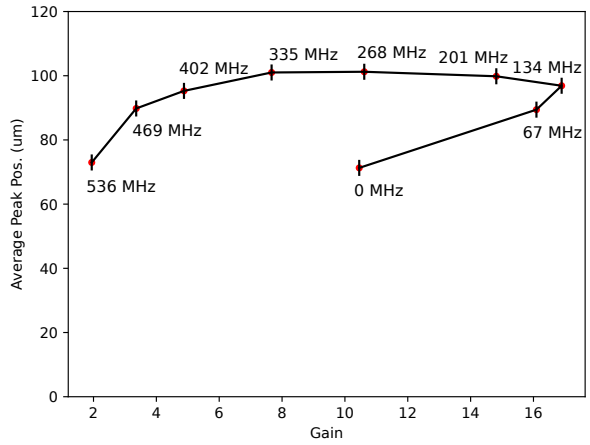


Figure 5.28: A parametric plot of the distance between the average positions of the 10 probe and conjugate beam slices nearest the centre of the pump profile vs. gain for each 1 photon detuning increment. The origin in the graph is arbitrary, since the absolute distance between the beams is not known, by the nature of the experiment.

of the 1-photon detunings. However, on the 'fast side' there is a noticeable dip away, as the plot doubles back on itself. This could be due to the higher probe absorption on this side of the gain peak.

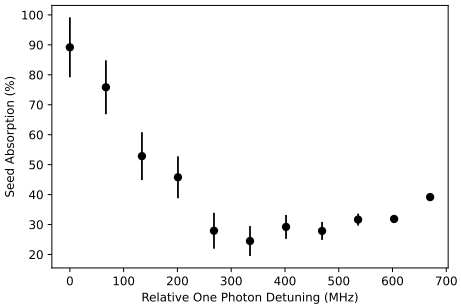


Figure 5.29: Total absorption of the seed over the 1Pd range.

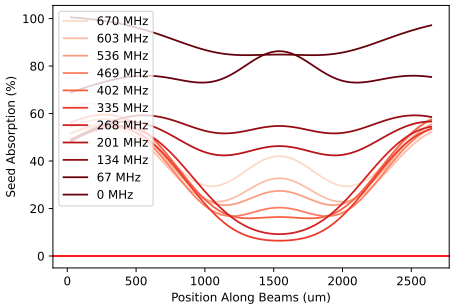


Figure 5.30: Spatial absorption of the seed over the 1pd range. The absorption valley is of a similar width to that of the pump beam diameter ($\sim 2000\mu m$).

It has also been seen from simulation that the displacement of the beams can be affected by loss as well as gain. To further investigate this, the seed absorption for each point in this range was determined, by two methods. The first was by simply integrating the probe, conjugate and seed beam images into three optical powers and calculating the difference between the probe and conjugate contributions as a percentage of the original seed beam power and subtracting this from 100. When there are no losses, the difference in power between the probe and conjugate should be the seed power, so the absorption should be 0%. The result of this is shown in figure 5.29. The error for this graph was calculated by propagating the approximate error on the measurement of each of the individual beam powers ($\pm 1\mu W$).

The other method was to first fit a Gaussian, in the horizontal direction, to each of the beam images, after they have been summed over the vertical direction. The difference between the probe and conjugate Gaussians as a proportion of the seed Gaussian was then calculated, subtracted from 100, and plotted in figure 5.30.

In the case of figure 5.29, it is clear that the peak in the transmittance is around the $400MHz$ point. This shows that could be a correspondence between the transmission (or absorption) on the Probe beam and the differential displacement of the squeezed regions.

This is because the pure gain and loss at each point may be position dependent, due to the light shift caused by the local pump intensity. This would significantly alter the susceptibilities in each region, which are responsible for the gain and loss in the 4WM system. The right side of the peak also decreases rapidly to extremely low seed transmissions, around 10% at its lowest point; this hints that there may be a relationship between this higher absorption and the beam splitting seen in the final images of figure 5.23.

5.6.2 Temperature Sweep

Next, a sweep of the cell temperature was undertaken over the typical ranges seen during a squeezing experiment (from $110°C$ to $100°C$). This was done by turning off the cell heater and allowing the temperature to drop as images of the probe and conjugate beams were taken. This parameter is especially important to investigate as it fluctuates the most from day to day, as it is dependent on the ambient room temperature in the lab.

It was thought this may have some considerable impact on displacement, as it affects the number density of Rubidium atoms in the cell. This in turn affects the 4WM efficiency and coherence time of the 4WM interaction. These both affect the susceptibilities involved in the interaction.

The same Gaussian fitting and peak plotting process used before was employed here. The results of this are shown in figure 5.31, where the differential displacement for each temperature is plotted against probe gain. This results in a familiarly curved differential peak position as gain increases, for each cell temperature. As before, the maximum gain of both the probe and conjugate beams deceases with falling temperature, likely a result of the falling number density of rubidium atoms leading to fewer 4WM interactions. The temperature itself does not seem to appreciably change how the differential displacement

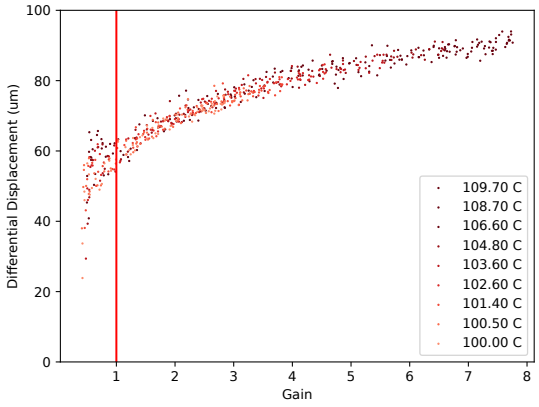


Figure 5.31: The differential displacement vs. gain for each cell Temperature.

depends on gain.

It looks very convincingly like the displacement at each temperature depends on probe gain the same way, as they all lie along the same curve in figure 5.31. Furthermore, when investigating the absorption of the beams during the temperature sweep, it can be seen that the total absorption of the seed beam is very consistent and all points are within error of each other. This is shown in figure 5.32.

When looking at things more granularly (figure 5.33) it can be seen that the absorption is very consistent between different temperatures. Further, it can be seen that the absorption once again flattens about the centre of the beams and that this flatness is consistent too. It is thought that this consistence may be related to why squeezing can be easily acquired over this temperature range, and is an encouraging sign that the relative displacement between squeezed regions should not change over this temperature range. As such, the exact temperature of the cell is unlikely to be a particularly important factor when trying to predict the relative displacement of squeezed regions, during a real world measurement.

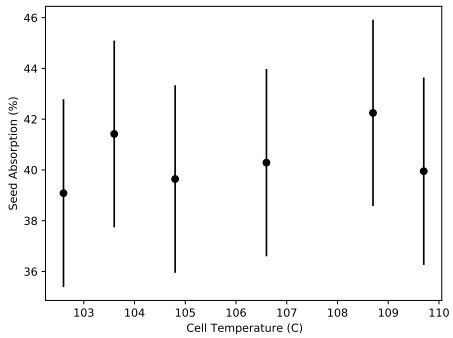


Figure 5.32: Total absorption of the seed over the temperature range. There is no change over the temperature range, within error.

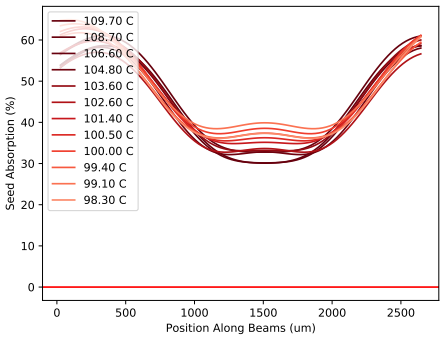


Figure 5.33: Absorption of the seed over the temperature range. The absorption valley is of a similar width to that of the pump beam diameter ($\sim 2000\mu m$). The absorption is nearly very similar for each temperature, with the integrated absorption being the same for each case.

5.6.3 Pump Power Sweep

Afterwards, a similar sweep was performed as the overall power of the pump beam was altered, instead of the 1 photon detuning. This experiment was performed as a sanity check to ensure that varying the overall pump power was equivalent to power being varied over the pump envelope, as there were a couple of effects that could have made this not quite so. In this instance, the 1 photon detuning was set to $270MHz$ away from the probe gain peak, in the 'slow side' direction. This was because this was the point where maximal displacement had been seen previously. The same peak finding and plotting process used previously was applied, and the displacement was be plotted against gain for each of the pump powers. This is shown in Figure 5.34.

As expected, the differential displacement for each overall pump power seems to depend on probe gain in approximately the same way, each plot seemingly having the same curvature and offset. Another key point to make here, is that this also indicates that

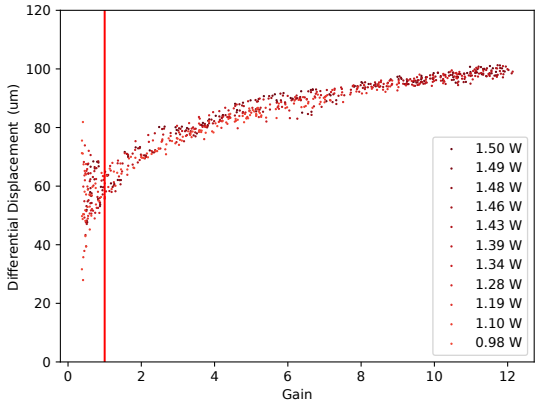


Figure 5.34: The differential displacement vs. gain for each overall pump power.

there is not a significant difference in the displacement effect on either side of the beam (where the k vector of the seed is either pointing towards the pump centre or away from it). Previously, there had been some concern that this could be a contributing factor.

Another potentially disruptive effect would be that the intensity gradient of the pump beam varied across the cell, due to the Gaussian envelope of the pump. Due to the horizontal motion of the beams, as they propagated through the cell, they were exposed to a narrow range of pump powers. There was a concern that this could have created an inhomogeneous growth for the beam profiles. However, this effect was not seen on the data. So, it can be said that the average local intensity across the beam path is all that matters, for these purposes.

Encouragingly, as can be seen in figure 5.36, the seed transmission is similar to that recorded in the $1pd$ sweep, with only a 10% difference between the recorded results.

Finally, since the pump intensity can be well controlled and the change in the differential displacement of the squeezed beams is small with small changes of the pump power, it is unlikely that this parameter will drift enough to cause issues whilst attempting to use the beams to take squeezed images, once a map of the displacements has been produced.

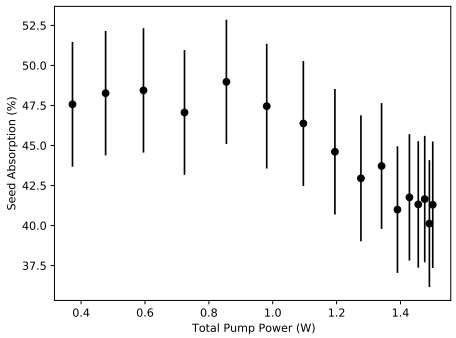


Figure 5.35: Total absorption of the seed over the power range.

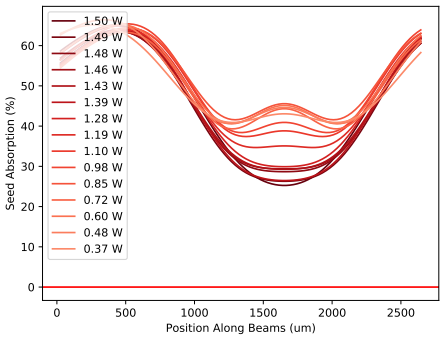


Figure 5.36: A plot of the total absorption of the Seed beam against total pump power. The absorption valley is of a similar width to that of the pump beam diameter ($\sim 2000\mu m$).

5.6.4 2 Photon Detuning Sweep

The final sweep was of the 2 photon detuning, over a range of $-2MHz$ to $8Mhz$. The resultant images from this sweep are shown in figure 5.37.

One interesting aspect of these images is that the sides of the beams seem to get more strongly clipped, as the detuning is decreased. One potential explanation for this could be that as the gain of the system increases to such high levels (up to 50 in the first image) the pump beam perhaps cannot be considered to be a constant field and starts to be depleted. Near the edge of the beam, where the pump power is already lower, it may be depleted enough to significantly affect the gain of the probe and conjugate. Hence, the shared displacement on the edges of the beams. These images were once again split and the peak positions were plotted against the gain of each of the slices. This is displayed in figure 5.38. Once again, the differential position, at least for this range of two-photon detunings, depends only on gain. However, the maximum gain achieved depended strongly on the exact two photon detuning used.

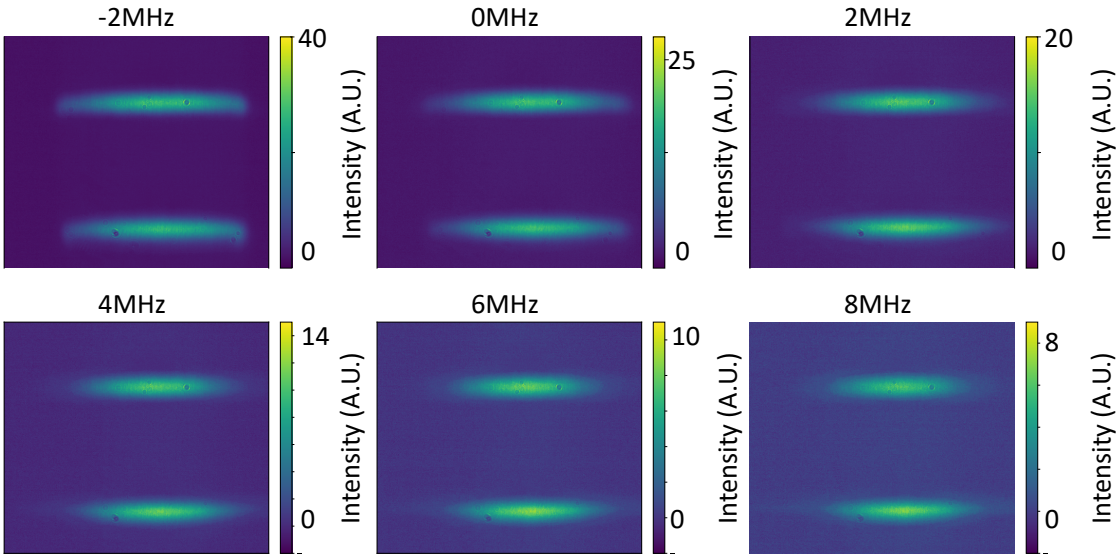


Figure 5.37: The full array of subtracted images obtained in the 2 photon detuning sweep. The x and y axis are spacial, with each pixel in the images representing a pixel on the camera.

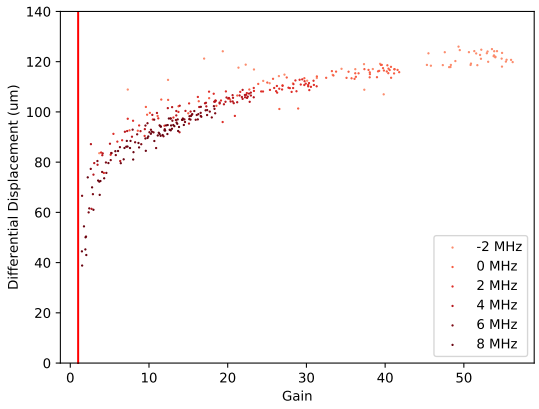


Figure 5.38: The differential displacement Vs. gain for each 2-photon detuning increment.

5.7 Conclusion

In this chapter, two simple models were proposed for a displacement effect between the probe and conjugate beams that caused them to move towards each other. Similar effects were seen in the simple model and the more physical one, validating that the dominant forces in this process are gain and loss of the system and not other potential aspects, such as refraction.

The effect was then seen, as produced by the varying intensity of the pump profile, through a beam transit investigation. The effects of other system parameters on the displacements were also measured and yielded gain curves of similar form and magnitude to those produced by simulation, validating them.

Overall, the effect of changing cell temperature in the $100°C$ to $110°C$ range was minimal, so mild instability in this should not impact future attempts to attain squeezed images. The role of pump power across the cell was shown to be equivalent to simply shifting the pump power locally, so future experiments could exploit this fact for ease of testing. Varying the 2-photon detuning over the $-2MHz$ to $8MHz$ range had a significant impact on beam gain and differential displacement, but all points conformed to the same curve, indicating that gain was the only important parameter in this case. In this region, loss is consistent, so is unlikely to have caused a significant impact. Finally, the 1-photon detuning was investigated over a $600MHz$ range and shown to have the most variability in its impact on the differential displacements. This is likely due to significant absorption on the 'fast side' of the gain curve, as on the 'slow side' the displacement curves are more similar in nature.

The general range of the effect was around $50\mu m$. This is large enough that it could be interrupting the formation of squeezed images, so this is consistent with previous postulates. This work builds the foundation for a second investigation that focuses on how

the squeezing itself is displaced and if it follows how the classical intensity distributions behave.

CHAPTER 6

PROPAGATION EFFECTS ON THE SPATIAL DISTRIBUTION OF THE SQUEEZING

AS demonstrated in chapter 5, the intensity profiles of narrow beams generated by the 4WM process can be displaced relative to each other by different amounts as according to different 4WM parameters. It was conjectured that this displacement is not just limited to the classical case, but might also cause a displacement of the quantumly correlated regions within the beams – a mode mismatch. This could represent a significant barrier to the production of squeezed images. Such a mode mismatch in a multi-spatial mode system would not just cause the misalignment of the correlated regions but would mean that light above the shot noise would be paired together, effectively anti-squeezing the system. This is because the intensity fluctuations on the beams as a whole are actually above the shot noise as discussed in section 1.1.4. As such, when any two sub-regions are subtracted from each other they will produce an anti-squeezed output, unless they are the sub-regions that are specifically correlated with each other.

In this chapter, investigations proving this to be the case are undertaken. Initially, a balanced photodetector was used to demonstrate squeezing between the entirety of probe and conjugate beams generated by the 4WM process. After this, a search was conducted, using physical slits, to find the relative location of the correlated regions within each of the beams. It was shown that the distance between these correlated areas varied according to the parameters of the 4WM similarly to how it does in the classical case, as was expected.

6.1 Measuring the Squeezing

To see displacements between the correlated sub-regions of the beams, it was necessary to be able to measure the level of squeezing between those sub-regions. The squeezing was two mode intensity difference type, as discussed in chapter 1. As such, measuring the level of squeezing was done using a custom-built Balanced Photo-Detector (BPD). Segments of the squeezed beams were separately focused by lenses onto the photo-detectors of the BPD. Internally, the signals they generate were subtracted from each other by the detector and the result was output to an oscilloscope and a spectrum analyser. From this, the power of the beams was measured and the noise at a 2.25 MHz was too. This was compared to a what would be expected from a shot noise limited beam, which was determined from a previous calibration measurement. As such, the level of squeezing between the beams was deduced.

The BPD itself consisted of two photodiodes leading into a trans-impedance amplifier. By the construction of the circuit (shown in figure 6.1), the currents of the two diodes operate in opposition to each other and naturally subtract and are amplified to produce V_{diff}. The BPD also has instrumentation amplifier buffered outputs at each of the photodiodes, V_1 and V_2. This allowed the power of each beam to be determined independently, allowing

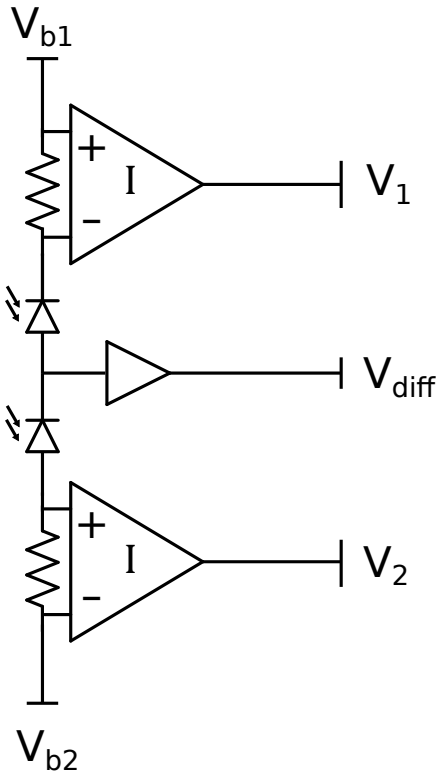


Figure 6.1: A circuit diagram of the BPD internals, the photo currents generated by the two photodiodes subtract at the junction between them and are converted to a voltage, V_{diff}, by a transimpedance amplifier. Resistors on either side of the photodiodes convert the small current they produce into a small voltage drop across them. This is amplified by two instrumentation amplifiers, I, to produce V_1 and V_2.

automation of the squeezing measurements.

6.2 Detector Calibration

Before meaningful results could be obtained from the BPD, its response at shot noise was evaluated such that it could be calibrated. Ideally, a measurement of the shot noise would be generated using a coherent state on each input of the BPD. However, in practise, it was equivalent to just splitting a (possibly noisy) beam $50:50$ and projecting each part onto each of the photo-detectors in the BPD. A noise measurement could then be taken,

Table 6.1: Calibration parameters for the BPD

Parameter	1V/	500mV/	200mV/	100mV/
α_0	3.24×10^{-9}	3.09×10^{-9}	3.10×10^{-9}	3.19×10^{-9}
N_0	4.62×10^{-10}	6.21×10^{-10}	6.16×10^{-10}	6.16×10^{-10}
Channels	CH3, CH4	CH3, CH4	CH3, CH4	CH3, CH4
Offsets (mV)	-118, -77.9	-77.9, -77.9	-10.5, -4.33	-7.79, -4.27

for a given total beam power. It was important that the intensities were as close to 50 : 50 as possible, as this helped mitigate any common mode classical noise on the beams that would else wise have caused error in the calibration.

The total power of the beam was varied and the noise detected at $2.25MHz$ was recorded as well as the voltage recorded by the oscilloscope when only one of the two beams was shone into their corresponding photo-detectors, v_1 and v_2. The squeezing was measured at this frequency as it was at its maximum here, since above this frequency the squeezing begins to reach the limits of its bandwidth and below this frequency classical noise begins to dominate.

It was known that the conversion from incident power to output voltage on the BPD was linear for the powers measured. As such, any noise measurements taken of the 4WM generated beams could be easily compared to the expected noise power from equivalently intense coherent beams, using

$$N_e = \alpha V + N_0, \tag{6.1}$$

where N_e is the expected noise power, $V = |v_1| + |v_2|$ is the combined voltage outputs from each of the photo-detectors when they are exposed to the beams, and α and N_0 were constants determined from the calibration process.

The calibration of a and N_0 was performed by taking measurements of the electronic noise on the BPD at 2.25 MHz when balanced beams of 15 incremented powers were incident on it. Equation 6.1 was then fit to the results and the constants determined. This was done for four different oscilloscope voltage divisions and the results are shown

in table 6.1.

From this, the squeezing level for any arbitrary input beams could be calculated simply by measuring their noise, N_m, and V. Then the expected noise could be calculated using equation 6.1 and the values compared logarithmically to produce squeezing value, s. Where

$$s = 10 \log_{10} \frac{N_m - N_0}{N_e - N_0}. \tag{6.2}$$

6.3 Searching for squeezed regions

To physically search for squeezed regions it was not enough to simply look at the intensity distribution of the beams, as was done in the classical experiment. Instead, small portions of each of the beams were picked off in the near field and their power fluctuations compared with the BPD. This was a simple matter of using a physical slit to block all but small vertical slices of each of the beams. A diagram of this is shown in figure 6.2, where the dashed lines represent the edges of the slits s_1 and s_2.

One slit was held static whilst the other was moved across the beam and the squeezing recorded at each point. The point of maximal squeezing can be understood to be when slit s_2 overlaps most with the region of beam 2 correlated with the region of beam 1 selected by slit s_1 (diagonal shading).

Various parameters of the system were altered and their effect on the relative position of these regions, ΔX, was determined. In these experiments, the parameters that were expected to have the biggest effect were the same as those in the classical ones: one photon detuning, two photon detuning, pump power, and temperature. Only the first three were investigated, as the temperature of the cell could only be changed by either altering the set point of the PID loop controlling it or by turning off the heating element and allowing it to 'free fall'. In the former case, this took too long to stabilise for an

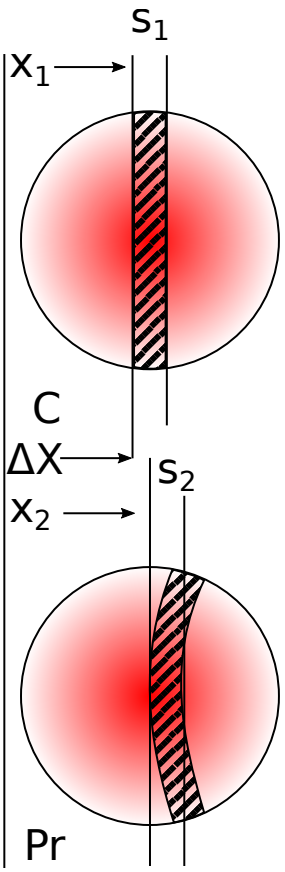


Figure 6.2: Diagram of the near field images of the probe and conjugate beams. The diagonal shaded regions represent two correlated areas between the probe and conjugate beams. The area is curved in the probe beam due to the influence of the varying pump intensity. The lines that extend beyond the circle represent the boundaries of two slits s_1 and s_2, that are used to select small slices of each beam for comparison.

experiment to be undertaken without sizeable error on the results. In the latter, the temperature changed too quickly for a single data set to be taken.

There was another complication in that the pump power varied in both the horizontal and vertical direction. If the pump power did have a significant effect, it would seem that any displacement effect would have varied in magnitude as the pump did. As such, a straight region in one of the beams would actually most correlate with a curved one in the other, as shown in the diagram. Since only straight sided slits were used in this

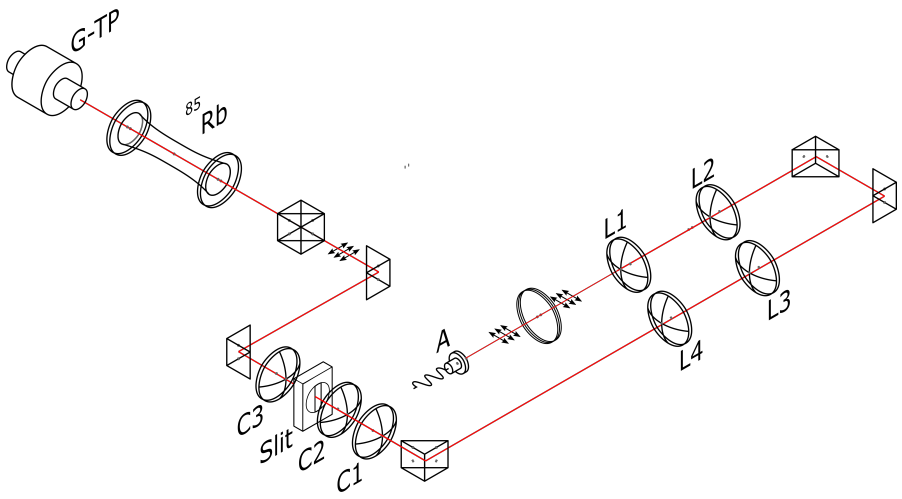


Figure 6.3: Diagram of the lens arrangement that produced a seed beam of the desired shape and size focused at the centre of the Rubidium vapour cell. The focal powers of the spherical lenses were $L1 = 100mm$, $L2 = 50mm$, $L3 = 50mm$, and $L4 = 100mm$. The focal powers of the cylindrical lenses were $C1 = 50mm$, $C2 = 50mm$, and $C3 = 100mm$.

experiment, it was key to mitigate this effect as much as possible.

This was done by shaping the seed beam such that it was very thin on the vertical axis and broad in the horizontal, as well as ensuring it was centred on the pump beam. This minimised any bending, as the peak of the Gaussian pump varied very little over the small diameter of the seed. The wide horizontal aspect of the Seed was useful as it allowed the pump power parameter to be varied both by changing the overall pump power and by simply transiting the other slit an increment between each sweep.

6.4 Seed Beam Shaping

As stated, before the cell, the seed beam needed to be shaped such that it had a high aspect ratio; ideally such that it was confined to a narrow region of the pump on the vertical axis whilst extending on the horizontal axis through a significant region of the pump intensity profile.

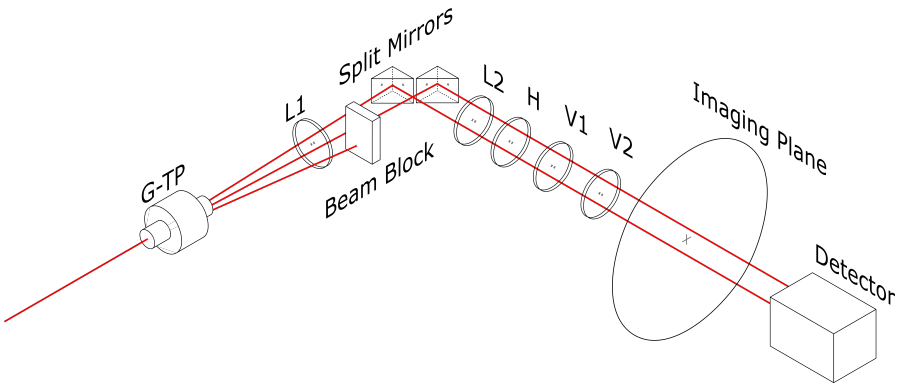


Figure 6.4: Diagram of the imaging setup that projects the probe and conjugate beams to the BPD

This was achieved with the system described in figure 6.3. It effectively consisted of two parts. The first, constructed entirely of spherical lenses ($L1 - L4$), served to focus a narrow beam into the centre of the cell both transversely and longitudinally. The second, formed of the slit and cylindrical lenses $C1 - C3$, expanded the beam in the horizontal direction. Part one of the system ensured that the beam waist was focused at the centre of the cell and was $200\mu m$ in the vertical direction. Part two of the system expanded this in the horizontal direction to $850\mu m$, resulting in an aspect ratio of $4.25 : 1$.
This portion of the system also allowed the beam to be positioned and angled transversely to the pump to optimise squeezing. In these experiments, the beam was centred on the pump and impinged at an angle of roughly $0.07mrad$ in the horizontal direction, corresponding to the phase-matching condition for typical 4WM parameters.

6.5 Imaging Setup

A detailed view of the imaging system used to capture the probe and conjugate beams is displayed in figure 6.4. After the cell, the probe and conjugate beams were separated and isolated from the pump beam. This was done by first passing the beams through

a Glan-Taylor polariser. Since the input pump beam was polarised orthogonally to the input probe seed, the output pump was mostly orthogonal too. Thus, most of it was deflected and removed. Some of it, however, made it through, as it was unpolarised light generated by florescence in the cell. Then the three beams entered the 4F imaging system formed by lenses $L1$ and $L2$. All of this was identical to how it was done previously.

The probe and conjugate beams were intercepted by a pair of split mirrors at the focal point of $L1$ whilst the pump remnant was allowed to pass between them. It was easiest to separate the beams here, as the ratio of beam separation vs beam size was maximised at this point. The split mirrors were angled such that the beams took separated paths that were equal in length through the rest of the system. The beams were then returned to their original state by another lens placed one focal length away, $L2$. Here, the arrangement of the split mirrors was different from in the previous investigation, being horizontal rather than vertical. This is because the beams were angled in the horizontal plane this time, and we were looking for horizontal displacements.

After this, the beams passed through a new anisotropic imaging system formed of three cylindrical lenses; one oriented horizontally, h, and the others vertically, $V1$ and $V2$. This system further stretched the beams by a horizontal magnification of around 8x at the imaging plane. It was at this plane that slits were placed to physically block all but a sliver of the beams, so the squeezing between those smaller sections could be measured. Such a large magnification was useful as it also magnified any displacements in the squeezing too and made them easier to measure.

Finally, the unblocked parts of the beams were focused onto the photodiodes of the BPD so that said squeezing measurements could be taken.

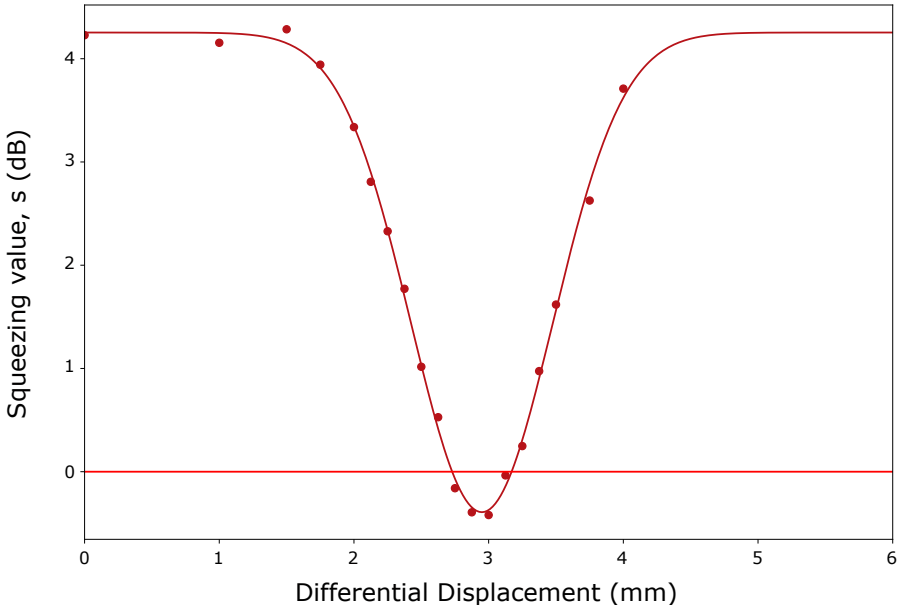


Figure 6.5: The squeezing recorded during a complete transit of the conjugate slit whilst the probe slit was held steady at parameters optimised for full beam squeezing. A Gaussian fit is also provided.

6.6 Motorised Translation Stage

To take reliable data, a method of quickly and accurately scanning the slits across regions of interest needed to be developed. Addressing this issue, an existing Thorlabs Linear Translation Stage was modified with the addition of a driving motor. The result was a Wi-Fi controlled motorised stage with a positional accuracy of smaller than $1\mu m$. Comparing multiple test runs determined that the measurable precision of the system was limited by the reading on the micrometer.

6.7 A Demonstration of Multi-Spatial Mode Squeezing

As discussed previously, the MSM nature of the squeezed light source was such that it allowed for quantum correlations between spatially matched regions of the twin beams [104, 105, 106]. To prove that this experimental system was capable of detecting such a squeezed state, a simple experiment was enacted.

First, the free parameters of the system were adjusted to maximise the squeezing on the entire beams, which was verified by the BPD to be $-1.81dB$. This was lower than typically seen as the shape of the beams was optimised for imaging local squeezing rather than for squeezing over the whole beam.

Next, a $1mm$ slit was placed in the imaging plane of the probe beam and transversely at the point of highest gain (this is the point of most intense pump within the cell). Another, $1mm$, slit was attached to the motorised translation stage, at the conjugate's imaging plane. This was done such that it could be swept across the entire conjugate image, along the long horizontal dimension. As a result, this experiment functioned as a physical version of the process in chapter 3.

The conjugate slit was then moved across the beam, stopping at regular intervals. At each stop, a measure of the squeezing between the selected regions was taken using the BPD. This produced a Gaussian dip similar to that seen in figure 6.5. This was used to determine a variable step size for a follow up sweep that became smaller near the peak such that there was a higher density of readings here. This follow up sweep was used as the final data for each measurement. This increased the accuracy of fits made to said peak.

That next sweep was then produced and the results are shown in figure 6.5, and it is immediately clear that the squeezing was spatially localised. This is highlighted by the inverted Gaussian seen in the noise data. Furthermore, encouragingly, the localised noise

reduction did dip below the quantum noise limit at its peak, so this noise reduction was definitely caused by squeezing rather than, for example, some common mode classical noise cancellation. However, at $2.25MHz$ the classical noise is negligible and the system is effectively at shot noise anyway.

The form of the peak can be understood by considering that only the intensity difference between the beams is squeezed and, further, that squeezing is only between small regions of the beams. Outside of these small regions, the photon statistics between the beams are not correlated. In actuality, when the beams are considered in isolation, the beams are anti-squeezed and have noise higher than the photonic shot noise of a coherent state. So, when uncorrelated regions are subtracted from each other, their noise adds together and the resulting measurement has a noise much larger than 0 dBm, as seen in figure 6.5. This anti-squeezing is what defines the magnitude of the upper bound of the squeezing values.

6.8 Demonstration of Displaced Squeezing

Previously, it was established that this setup was capable of producing MSM squeezed states. Next, the relative displacement of these correlated regions was demonstrated over a range of 4WM parameters. As such, a compelling explanation as to why MSM squeezing has been previously hindered has been provided.

In order for this to be done, a similar setup as seen before was used. Only this time, many sweeps of the conjugate slit were taken whilst another key system parameter was changed between each.

The parameters most relevant and practical to explore were the 1-photon detuning (1pd), 2-photon detuning (2pd), and the pump power. The results of these experiments are covered in order below.

6.8.1 One Photon Detuning Sweep

In this sweep, all parameters were held static aside from the 1pd. In this case, the 2pd was $8MHz$, pump power was $1.3W$, and the temperature was $\sim 100°C$.
The 1pd was altered by changing the frequency of the TI:Sapphire laser. Practically, this was done via a control over IP interface and automated using Selenium WebDriver – a program typically used for web scraping.
Initially, all parameters were optimised for maximal squeezing over the entirety of the beams. After this, an initial optimisation sweep of the conjugate position was completed, with the conjugate slit position being incremented $1mm$ at a time and the squeezing at each point being measured via the method described in sections 6.1 and 6.2. This allowed the point of peak squeezing to be deduced so that the increments used in subsequent sweeps could be reduced to ensure a high density of samples near the squeezing peak.
By this method, the points in figure 6.6 were produced. These were used to create fits of the equation

$$G(x, A, \bar{x}, \sigma, c) = -|A|e^{\frac{-(x-\bar{x})^2}{2\sigma^2}} + c. \tag{6.3}$$

All parameters were left unconstrained.
These fits are also shown in figure 6.6. Next, to determine a relative displacement of the squeezed regions, over the 1pd sweep, the mean positions, $\bar{x}$, were plotted in figure 6.7. Here it can be seen that when blue detuned from the gain peak, in the low loss region of the 1-photon detuning, the distance between the probe and conjugate squeezed regions was static and 'locked' together. This is the same as seen classically. As the 1pd moves towards the absorption peak, the relative displacement of the squeezed regions increases rapidly. This corresponds well with the movements seen classically. This region of rapidly changing displacement is also on the 'fast side' of the gain curve of the 4WM resonance. This is to say that although there was a strong gain in the probe and conjugate beams

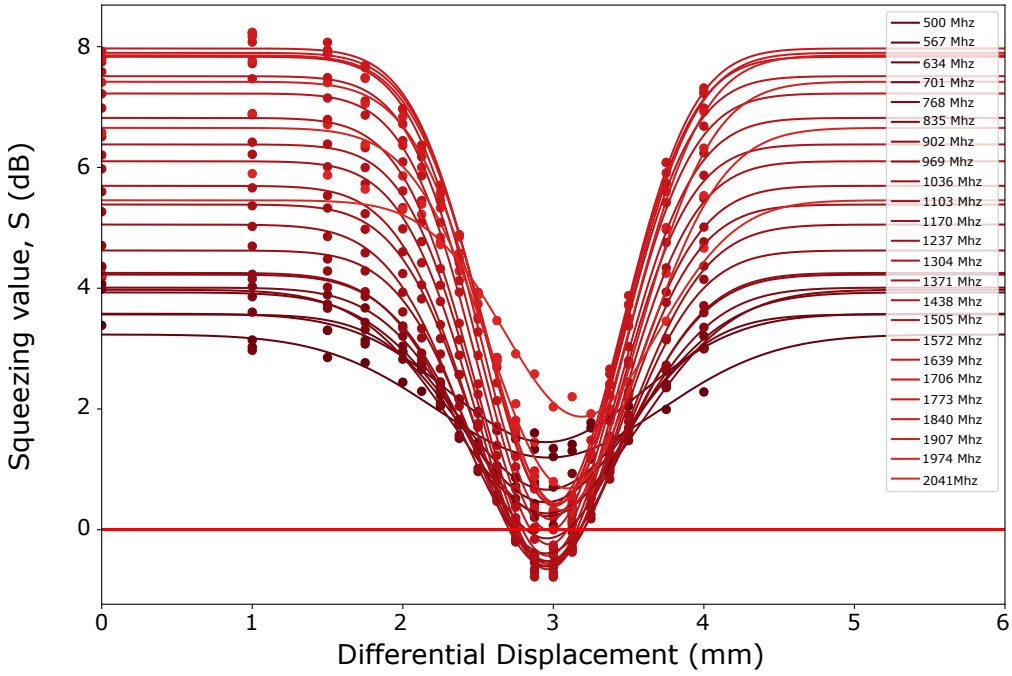


Figure 6.6: The squeezing recorded during a series of complete transits of the conjugate slit whilst the probe slit was held steady and the one photon detuning (1pd) was increased in each transit. A Gaussian fit is also provided for each of these transits too.

due to 4WM, there was also significant loss due to absorption of the beams by the atomic medium.

The effect of absorption on displacement does seem to be intimately linked to the rapid movement and degradation of the squeezing dips. This is seen in the final peaks of figure 6.6. It has also been shown, in simulation, to allow a differential displacement that increases away from the optical axis, as was seen here. In order to more accurately track the 1pd frequency as it was swept, a simple transmission spectroscopy produced alongside the other experimental measurements. This was done using a beam pick-off just before the noise eater AOM, passing a $100\mu W$ beam through a natural Rubidium vapour cell. The output was then recorded using a photodetector. The pick-off was roughly as the frequency of the pump, after subtracting $160MHz$ due to the effect of the noise eater and pump AOMs.

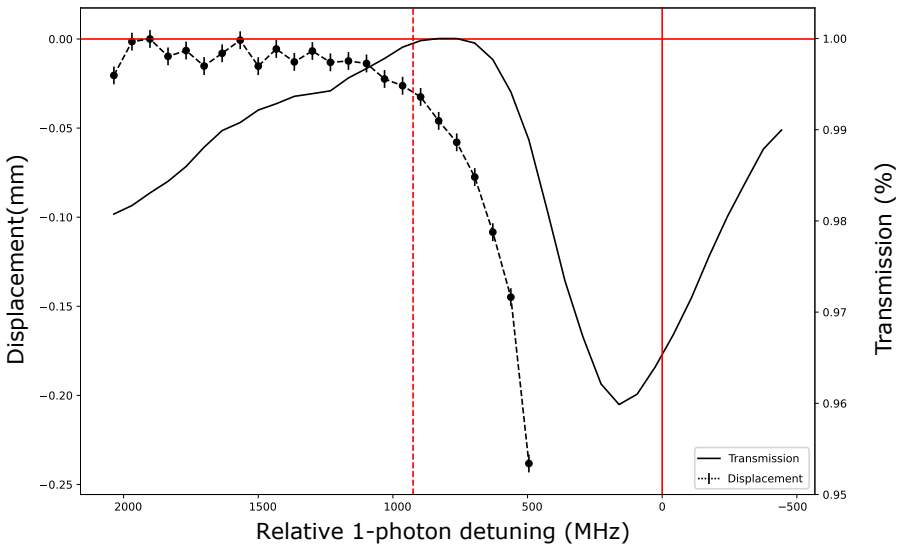


Figure 6.7: The relative mean position of each of the fits displayed in figure 6.6. Alongside is a plot of a rubidium transmission spectra, allowing an accurate frequency estimation for the 1pd at each point. The errors on these points were produced by first holding all parameters at optimal squeezing, then transiting the conjugate 10 times. The standard deviation of the mean of fits made to these transits was then used as an estimate of the error. The dashed red line represents the position at which the maximum probe gain was realised.

The tacit assumption here was that the overall intensity of the laser was stable, so a reference beam was not needed. In practice, this was mostly true. The results of this are plotted alongside the displacements in figure 6.7.

Another perspective on these results can be seen by instead plotting differential displacement as a function of probe gain, as is shown in figure 6.8.

Here it is clear that the differential displacement was very flat as gain increases, along the 'slow side' of the 4WM peak. This indicates that the probe and conjugate segments are already well locked together at this point. From this point on, the 4WM resonance only got stronger, so it would have been expected that this locking got stronger too. However, the absorption term on the probe grew especially rapidly towards the 'fast side' of the resonance, and this is where we see both the gain decreasing and the differential displacement increasing away from the pump axis. Similar behaviour has been seen in

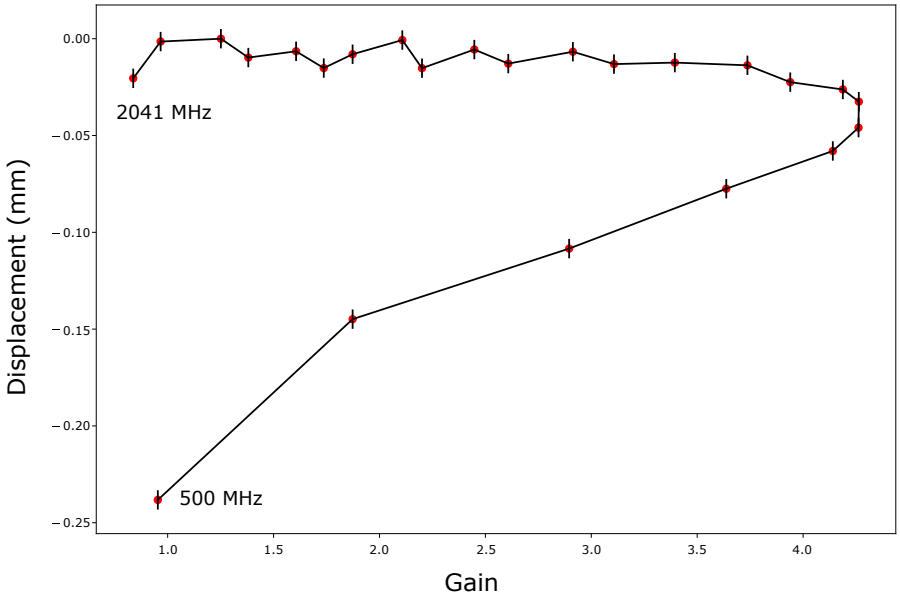


Figure 6.8: A parametric plot of the mean displacement of each peak against the gain on the probe portion.

the classical case and simulations too, specifically in figure 5.28.

6.8.2 Two-Photon Detuning and Power Sweeps

The 2-photon detuning and power sweeps were performed next and their results are displayed in figures 6.9 and 6.10.

The movements of the differential displacement as a result of the 2-photon detuning sweep are somewhat complicated. This is suspected, mostly, to be due to the interplay between gain and loss effects as this parameter was changed. Looking at figure 6.11 and above a gain of 2 a simple correspondence can be seen, where more gain linearly relates to movement towards the pump axis. This is the same trend, direction, and of roughly the same magnitude was seen on the classical data too. Of course, the magnitude of the effect is hard to compare directly, as the cell used in these experiments was 12.5 mm long rather than 20 mm, like that in the classical experiments. However, looking below a gain

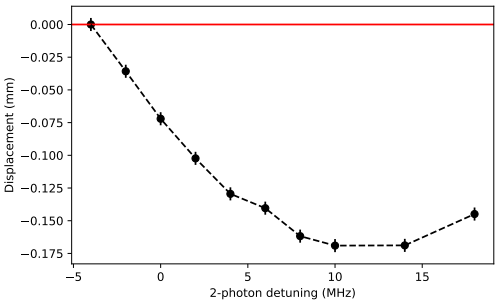


Figure 6.9: The mean position of each of the fits made as 2pd was swept.

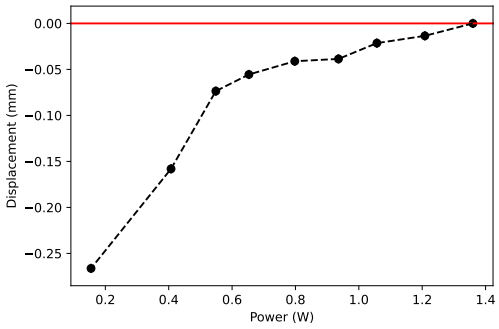


Figure 6.10: The mean position of each of the fits made as pump power was swept.

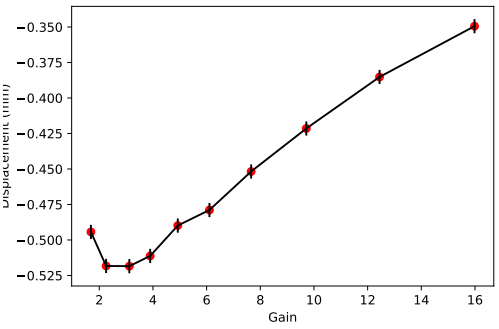


Figure 6.11: A plot of the mean displacement of each peak against the gain on the probe portion (2pd sweep).

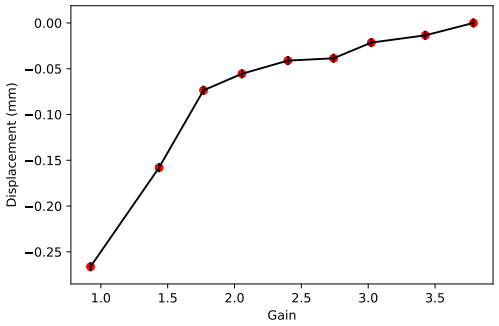


Figure 6.12: A plot of the mean displacement of each peak against the gain on the probe portion (power sweep).

of 2, a situation wherein the differential displacement doubled back on itself developed. It is thought that this was due to the effect of significant probe loss beyond this point. Conversely, the pump power sweep has simple behaviour. The differential displacement begins positive (away from the pump axis) and, as the power is increased, the displacement reduces linearly. It then plateaus, or saturates, past a certain point in much the same way as has been seen in the classical results and simulations. Looking at figure 6.12 shows us effectively the same trend, leading to the interpretation that this change of differential displacement (moving towards and locking to the pump axis) was almost entirely caused by changing gain. This was the same trend, direction, and of roughly

the same magnitude seen on the classical data too. It also seems there was little impact from absorption effects. This makes sense, since the other parameters in the system were optimised to a high level of squeezing, inherently limiting the absorption on the system.

6.9 Double sweep

Finally, these results were related to the situation when generating full-sized beams, with a probe transit experiment. In this case, the incremented parameter was the position of the probe slit, between each transit of the conjugate. In effect, this sampled different pump powers, due to the Gaussian envelope of the pump. The results are shown in figure 6.13.

It is immediately recognisable that the points trend linearly upwards with probe position, which does not correspond with the probe gain. However, this is explainable by a difference in magnification between the probe and conjugate beams, which is a well documented effect caused by probe lensing in the cell. The approximate difference in magnification can be calculated by fitting a linear line to two displacement points of similar gain and taking its gradient. Points of a similar gain are used to mitigate any differential displacement effects not caused by magnification. This gradient corresponds to a roughly 2.6% difference in magnification.

Focusing on the difference between the data and the trend line, a distinct movement away from the pump axis can be seen as gain decreases below 3. Despite this, generally a very minimal effect is seen, with the differential displacement being mostly flat at higher gains. This is expected since this experiment was performed in the high gain 'saturated' region of the pump power.

With this in mind, it is likely that a larger displacement would be seen if a larger range of probe gains was explored, then this effect would be more significant. This could be

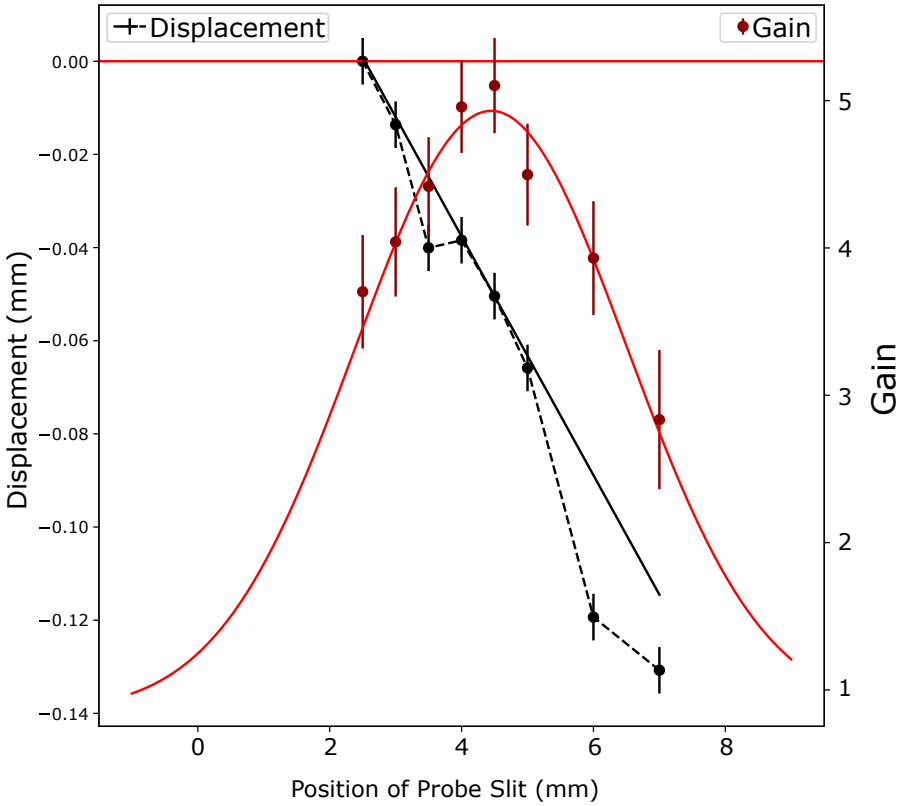


Figure 6.13: The results of the probe transit sweep, The probe gain is shown in red while the differential displacement shown in dashed black. A linear fit of two points at the similar gain is shown in solid black.

achieved by widening the probe seed beam further such that it samples more of the pump beam envelope. Centring this on the pump beam would also allow the effect to be seen on either side of the pump beam, presenting as a dip in the displacements. This would allow conformation of the effect despite any interference from differential beam magnification.

CHAPTER 7

A SCHEME FOR ALL OPTICAL CORRECTION OF THE PROPAGATION EFFECTS

THE nature of the propagation effects in a two mode optical amplifier has now been thoroughly explored, both in simulation and experimentally, through exploring a 4WM interaction in a Rubidium vapour. More precisely, a large displacement effect has been seen in both cases. It has been discussed how this effect may represent a significant barrier to the formation of squeezed images. Now let us discuss how we may overcome it in the future.

7.0.1 Split Amplification with Intermediary backpropagation

Split Amplification with Intermediary backpropagation (SAI) is a proposed technique that aims to reduce the displacement effect in extended two mode optical amplifiers through optical design such that it is small enough that electronic corrections are not

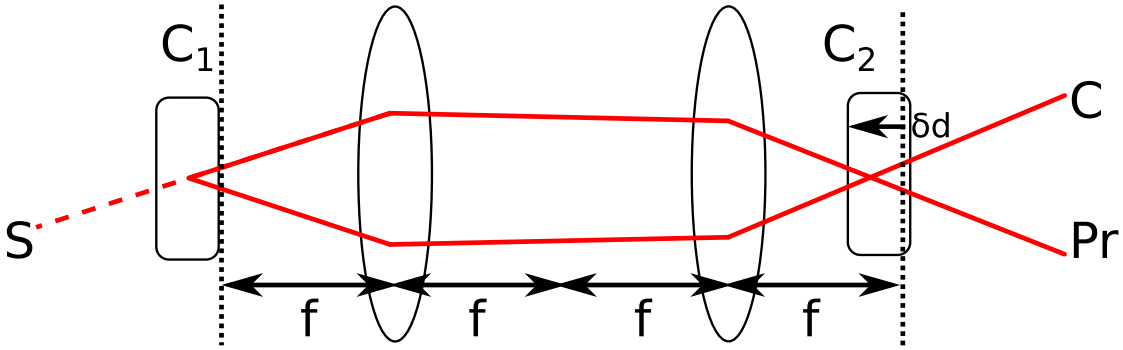


Figure 7.1: A general scheme of SAI, where an initial optical amplifier C_1 generates two beams, and a displacement effect between them. This is followed by a 4F system that inverts the k vectors of each of the beams before they enter into another optical amplifier C_2. Any displacement effect in the second amplifier is in the opposite direction to that seen in the first, so acts to mitigate the effect of the initial displacements. C_2 is displaced from the focal point of the 4F system by δd, to tune the amplifier.

required at the imaging stage.

It works by splitting the amplifier into two sections, C_1 and C_2, that are separated by a 4F system. A seed is introduced into C_1 at an angle as usual and this results in the generation of twin output beams, that will experience a displacement effect between them. After, the 4F system serves to refocus the twin beams into C_2. However, the front face of C_2 is placed before the focal point of the second lens in the 4F system. This is effectively the same thing as back propagating the probe and conjugate beams by δd in free space before they propagate into the second cell. When δd is large enough, this switches the positions and momenta of the two beams so that when they propagate through C_2 the displacement effect acts in the opposite direction to what occurred in C_1.

Figure 7.1 gives a more accurate picture of this scheme. Here it can be seen that the focal point, or object plane, of the 4F system is positioned at the output surface C_1. The exact position of C_2 can be moved, regarding the imaging plane of the 4F system. It can be moved from $0mm$ where the input surface of C_2 lies on the imaging plane, to

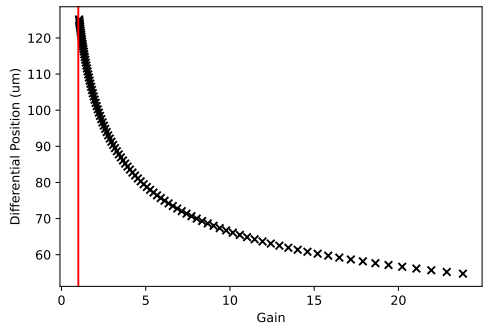


Figure 7.2: A simulation of a SAI amplifier where C_1 and C_2 are identical. In this case, each of the cells are $10mm$ long, $\chi_{PrPr} = 0.15 + 0i$, and χ_k is swept over a range of 0 – 0.23 rad mm^{-1}. These parameters are as similar to previous simulations as possible while producing similar levels of gain. This allows for a direct comparison between them. In this case $\delta d = 0mm$.

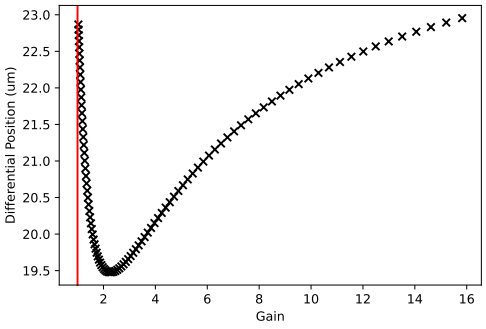


Figure 7.3: A simulation of a SAI amplifier where C_1 and C_2 are identical. In this case, each of the cells are $10mm$ long, $\chi_{PrPr} = 0.15 + 0i$, and χ_k is swept over a range of 0 – 0.23 rad mm^{-1}. These parameters are as similar to previous simulations as possible while producing similar levels of gain. This allows for a direct comparison between them. In this case $\delta d = 16mm$.

any displacement back towards the imaging optics. By positioning C_2, the field received at C_2 can be altered. The goal of this is to 'flip' the input position and propagation directions of the beams so that the displacement effect of C_1 can be undone by C_2.

Of course, the effect is not entirely cancelled, as the situations at C_1 and C_2 are subtly asymmetric. This is because the system is only seeded on one beam for C_1 whilst it is seeded on both beams for C_2. The overall powers and shapes of the seeds also differ due to the initial gain from C_1.

This scheme was demonstrated in simulation, using the same initial seed and parameters as used in figure 5.10. The only significant difference was that, instead of a single $20mm$ gain region, the gain region was split into two $10mm$ sections with a back propogation stage between them. The results of this are shown in figures 7.2 and 7.3.

In this case, two situations were simulated. Figure 7.2 shows the case where $\delta d = 0mm$. This is equivalent to there being no back propagation at all, so can be used as a benchmark

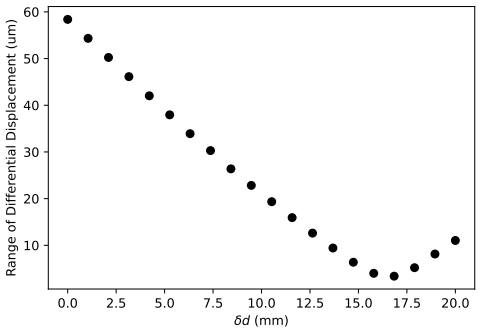


Figure 7.4: The range of displacements seen, over a gain range of $0 - 10$, against δd.

that figure 7.3 can be compared to. In this case $\delta d = 16mm$. In both cases, the form of the displacement is upside-down as compared to what is seen elsewhere in this thesis. This is because the 4F system also imparts a -1x magnification on the beams. Still, the magnitude of the displacement and overall gain seen in the first case is essentially the same as seen in previous simulations. Focusing in on a smaller region, a range in differential displacement of $\sim 60um$ was seen over a gain range of $0 - 10$.

In the second case, it can be seen that the amplifier produces a displacement effect with a range of only $\sim$ 5% of that seen in the previous case, for a gain range of $0 - 10$. This represents a significant improvement for such a simple geometry. Further, this is significantly smaller than the coherence area for a $10mm$ long cell ($\sim 50um$). Therefore, it has been diminished to the point where it is no longer likely to be a significant barrier to squeezed image generation.

It can be seen that $\delta d = 16mm$ is near optimal by looking at figure 7.4, where the range of differential displacements has been plotted against δd. Here it can be seen that the differential displacement trends down until this point before beginning to ascend again. Such a minimal displacement shows up very obviously when the probe and conjugate intensity profiles are plotted as they exit the C_2. This is shown in figures 7.5 and 7.6.

Another thing of note is that the curve in figure 7.3 starts increasing in the positive

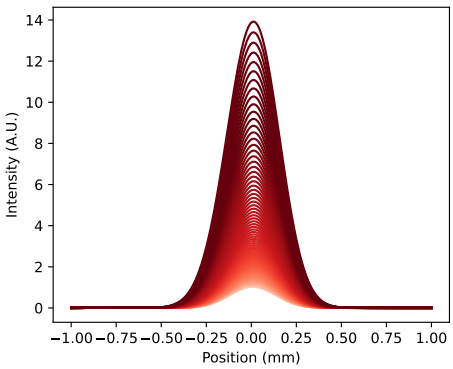


Figure 7.5: The probe intensity profiles after exiting C_2, when $\delta d = 16$.

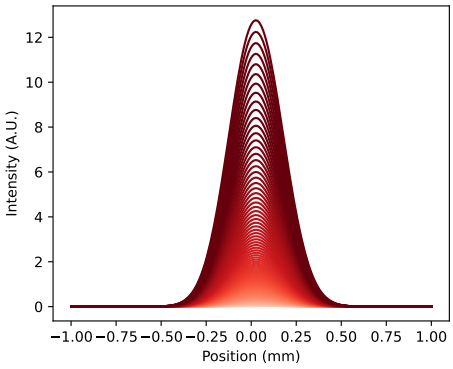


Figure 7.6: The conjugate intensity profiles after exiting C_2, when $\delta d = 16$.

direction and then begins to fold back on itself just after the gain of 2 mark. This is likely because the contribution of C_1 is the dominant aspect at lower overall gains and C_2 begins to dominate at higher gains, dragging the differential displacement in the negative direction. It is likely that cleverly adjusting the relative lengths of C_1 and C_2 or even adding further SAI stages would allow for tailoring of the displacement curve to minimise its range and flatten its response. However, this is would not be worthwhile while the magnitude of the effect is smaller than the coherence area. It may still be worth adding further stages, though, to form a SAI stack. This is because, in the case where the beams are continually refocused into multiple cells, the coherence area depends solely on the length of the longest cell. As such, multiple cells can be used to produce arbitrarily high gains, without the usual limitation of increasing the coherence area as well. This is effectively coherence area shrinking.

Overall, this technique represents a pathway to compensate for the displacement effect entirely optically. This comes with the advantage that when generating squeezed images, it would not require any extra calibration or processing steps, at the expense of adding slight optical complexity. Further, the SAI stack structure could represent a way to push past the coherence area, which has been considered a much more fundamental limit of

such optical amplifiers.

CHAPTER 8

CLOSING REMARKS

NOW, we come to the end of my writing, so let's take the opportunity to look at some highlights from my time here.

One significant milestone in these investigations has been in the identification and formal expressing of the 'x' effect, that has plagued previous attempts to form squeezed images at low temporal frequencies. Specifically, understanding the impact of even small amounts of shared classical noise on the beams led to an emphasis on developing a 'noise eater' system. This was shown to reduce classical noise significantly at the frequencies it mattered most (centred around the PIXIS camera operating frequency). As such, the experiment is primed for another camera-based investigation, that will hopefully yield much clearer results.

Generally, however, classical noise will likely always represent a problem when attempting to produce images with CCD cameras. This is because, even when running in kinetic mode, CCDs are relatively slow integrating devices, as compared to other measurement tools such as photodiodes. As a result, the images they acquire will only be able taken

at a relatively slow rate, where classical noise is large. Alternatively, this could be solved with one development – an image sensor that can sample in the low MHz range. It seems simple, but then it must be considered that this sensor needs to contain on the order of $1MPs$, have a quantum efficiency in the high $90\%s$, and an exceptionally low electronic noise.

One option would be a microlens array spaced in front of a precision photodiode array. Photodiodes would allow for much faster acquisition times than a CCD, since they are continuous in their output. If this technology is developed, then a squeezed imaging platform could be operated in the high frequency regime, where the 'x' effect holds no power. To prevent unnecessary power being dumped into the sample, the probe beam could be microsecond pulsed by pulsing the seed beam appropriately, too.

Another area of significant development was in discovering and charting of the differential displacement due to the propagation effects in the 4WM gain media, as well as the development of a simple model to explain its action. This persists even into the high temporal frequency domain. Despite this effect being small spatially, it could have a significant impact on the quality of the local squeezing. This is because outside a localised correlated regions the beams are anti-squeezed. As such, the noise rapidly increases when the regions are ever slightly mismatched.

Fortunately, since the spatial displacement is so small, it is an option to correct for it digitally via image registration. When this is solved, any stray displacement in the correlated regions could be calibrated for in situ. A blank image could be taken and software algorithms can be run to find the best mapping of correlated regions from one beam to another. Then, when samples are imaged, this mapping can be used to correctly subtract the beams from each other and extract a squeezed image.

It has also been shown, via simulation, that this effect could be corrected for optically, by running the optical amplifier as a SAI system. This would have the advantage of remov-

ing the need for digital correction and calibration being required, since the displacement would be automatically corrected for even as system parameters changed.

In short, quantum imaging is on the horizon and there are bright things ahead for this technology.

APPENDIX A

FURTHER DETAILS

A.1 Derivations and calculations

A.1.1 Magnetic Field Derivation

Taking

$$\xi_x(z,t) = \xi_0 \sin(kz)\sin(\omega t) \tag{A.1}$$

and given that

$$-\frac{\partial B_y}{\partial z} = \epsilon_0\mu_0\frac{\partial \xi_x}{\partial t}, \tag{A.2}$$

we see that

$$B_y = -\int \epsilon_0\mu_0\frac{\partial \xi_x}{\partial t}\delta z. \tag{A.3}$$

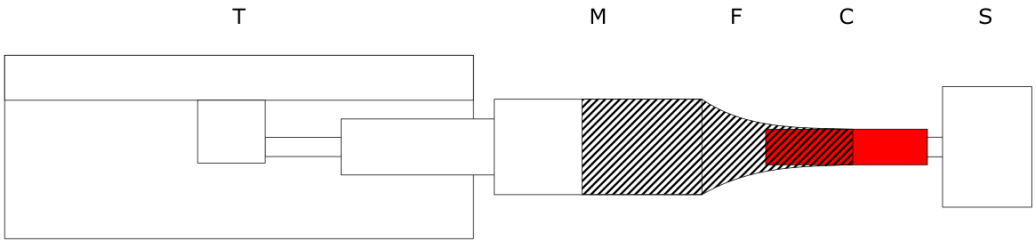


Figure A.1: A diagram of the mechanical part of the motorised translation stage; the various parts are labelled: T, translation stage; M, micrometer; F, flexure; C, coupling; S, stepper motor.

Via differentiation, we see:

$$B_y = -\int \epsilon_0 \mu_0 \omega \xi_0 \sin(kz) \cos(\omega t) \delta z. \tag{A.4}$$

Therefore:

$$B_y = \frac{\epsilon_0 \mu_0 \omega \xi_0}{k} \cos(kz) \cos(\omega t). \tag{A.5}$$

Which finally brings us to:

$$B_y = B_0 \cos(kz) \cos(\omega t). \tag{A.6}$$

A.2 Technical Details

A.2.1 Motorised Translation Stage System Design

The system consisted of two subsystems, electronic and mechanical. The electronic part consisted of a Pi Pico W, an RP2040 based microcontroller board, and a driver board to control the stepper motor used in the system. Together, these provided a flexible way to

power and control the board.

Control of the device was via a website hosted on the Pi Pico W itself; the Pico was configured as a network access point such that it acted as a Wi-Fi router that any capable device could connect to. From here, the device could be controlled via a Graphics User Interface (GUI) by connecting to the Pico using a browser. Alternatively, it could be code interfaced via URL requests.

The mechanical aspect of the system is represented in figure A.1. It consisted of a Thorlabs Linear Translation Stage, T, connected to a 28BY-J-16 stepper motor, S. The stage itself was driven by a micrometer, M, such that each full rotation of the micrometer produced a translation of $0.5mm$ on the sliding top of the stage.

The stepper motor was coupled to the micrometer via a plastic coupling, C, and flexure join, M. The flexure allowed for the rotational motion of the motor to be translated to the micrometer despite an offset between each of their axes of rotation – allowing greater flexibility in the positioning of the motor relative to the micrometer.

The stepper motor stepped 16 times per full rotation and contained an internal gearbox with a reduction of $16:1$. As a result, each rotation of the micrometer took 512 steps, allowing an angular control of $0.7°$. This translated to $0.976\mu m$ of linear motion at the stage.

Ramp Up and Ramp Down

One key source of inaccuracy in stepper motors is missed steps during accelerations of the driven load. Since the load has its mass and inertia, it could only be accelerated so quickly by the limited torque of the motor.

If a faster acceleration were attempted then steps would be missed such that the maximum torque of the motor was not exceeded. This resulted in a system where the requested

number of steps did not match the actual number of steps taken and positional accuracy is lost. One solution was to set a constant time between each step, T, so large that the system never attempted to accelerate beyond its capacity. This worked, but severely impacts the maximum angular velocity achievable.

The superior solution was to start T at a relatively large value and linearly decrease this value at a constant rate until a set minimum is reached. This process was then reversed when the motor was slowed, which helped to avoid the inertia of the system causing step overshoot as well as allowing a smooth change in motor direction. This process is called ramping and was implemented in the control code for the device [107].

BIBLIOGRAPHY

[1] T. H. MAIMAN. "Stimulated Optical Radiation in Ruby". In: *Nature* **187** (June 1960), pp. 493–494. DOI: 10.1038/187493a0. URL: https://doi.org/10.1038/187493a0.

[2] M. Tse et al. "Quantum-Enhanced Advanced LIGO Detectors in the Era of Gravitational-Wave Astronomy". In: *Phys. Rev. Lett.* **123** (23 Dec. 2019), p. 231107. DOI: 10.1103/PhysRevLett.123.231107. URL: https://link.aps.org/doi/10.1103/PhysRevLett.123.231107.

[3] Ling-An Wu et al. "Generation of Squeezed States by Parametric Down Conversion". In: *Phys. Rev. Lett.* **57** (20 Nov. 1986), pp. 2520–2523. DOI: 10.1103/PhysRevLett.57.2520. URL: https://link.aps.org/doi/10.1103/PhysRevLett.57.2520.

[4] Oleg V. Misochko, Jianbo Hu, and Kazutaka G. Nakamura. "Controlling phonon squeezing and correlation via one- and two-phonon interference". In: *Physics Let-*

ters A **375**.46 (Nov. 2011), pp. 4141–4146. DOI: 10.1016/j.physleta.2011.09.054. URL: https://doi.org/10.1016%5C%2Fj.physleta.2011.09.054.

[5] Jian Ma et al. "Quantum spin squeezing". In: *Physics Reports* **509**.2-3 (Dec. 2011), pp. 89–165. DOI: 10.1016/j.physrep.2011.08.003. URL: https://doi.org/10.1016%5C%2Fj.physrep.2011.08.003.

[6] Henning Vahlbruch et al. "Detection of 15 dB Squeezed States of Light and their Application for the Absolute Calibration of Photoelectric Quantum Efficiency". In: *Phys. Rev. Lett.* **117** (11 Sept. 2016), p. 110801. DOI: 10.1103/PhysRevLett.117.110801. URL: https://link.aps.org/doi/10.1103/PhysRevLett.117.110801.

[7] R. E. Slusher et al. "Observation of Squeezed States Generated by Four-Wave Mixing in an Optical Cavity". In: *Phys. Rev. Lett.* **55** (22 Nov. 1985), pp. 2409–2412. DOI: 10.1103/PhysRevLett.55.2409. URL: https://link.aps.org/doi/10.1103/PhysRevLett.55.2409.

[8] C. F. McCormick et al. "Strong relative intensity squeezing by four-wave mixing in rubidium vapor". In: *Opt. Lett.* **32**.2 (Jan. 2007), pp. 178–180. DOI: 10.1364/OL.32.000178. URL: https://opg.optica.org/ol/abstract.cfm?URI=ol-32-2-178.

[9] M. D. Levenson, R. M. Shelby, and S. H. Perlmutter. "Squeezing of classical noise by nondegenerate four-wave mixing in an optical fiber". In: *Opt. Lett.* **10**.10 (Oct. 1985), pp. 514–516. DOI: 10.1364/OL.10.000514. URL: https://opg.optica.org/ol/abstract.cfm?URI=ol-10-10-514.

[10] C. F. McCormick et al. "Strong low-frequency quantum correlations from a four-wave-mixing amplifier". In: *Phys. Rev. A* **78** (4 Oct. 2008), p. 043816. DOI: 10.1103/PhysRevA.78.043816. URL: https://link.aps.org/doi/10.1103/PhysRevA.78.043816.

[11] Zhongzhong Qin et al. “Experimental Generation of Multiple Quantum Correlated Beams from Hot Rubidium Vapor”. In: *Phys. Rev. Lett.* **113** (2 July 2014), p. 023602. DOI: 10.1103/PhysRevLett.113.023602. URL: https://link.aps.org/doi/10.1103/PhysRevLett.113.023602.

[12] Da Zhang et al. “Enhanced intensity-difference squeezing via energy-level modulations in hot atomic media”. In: *Phys. Rev. A* **96** (4 Oct. 2017), p. 043847. DOI: 10.1103/PhysRevA.96.043847. URL: https://link.aps.org/doi/10.1103/PhysRevA.96.043847.

[13] Mikhail I. Kolobov. “The spatial behavior of nonclassical light”. In: *Rev. Mod. Phys.* **71** (5 Oct. 1999), pp. 1539–1589. DOI: 10.1103/RevModPhys.71.1539. URL: https://link.aps.org/doi/10.1103/RevModPhys.71.1539.

[14] Guilherme B. Xavier and Gustavo Lima. “Quantum information processing with space-division multiplexing optical fibres”. In: *Communications Physics* 3.1 (Jan. 2020). ISSN: 2399-3650. DOI: 10.1038/s42005-019-0269-7. URL: http://dx.doi.org/10.1038/s42005-019-0269-7.

[15] Marco Genovese. “Real applications of quantum imaging”. In: *Journal of Optics* **18**.7 (June 2016), p. 073002. DOI: 10.1088/2040-8978/18/7/073002. URL: https://doi.org/10.1088%2F2040-8978%2F18%2F7%2F073002.

[16] Ashok Kumar and A. M. Marino. “Spatial squeezing in bright twin beams generated with four-wave mixing: Constraints on characterization with an electron-multiplying charge-coupled-device camera”. In: *Phys. Rev. A* **100** (6 Dec. 2019), p. 063828. DOI: 10.1103/PhysRevA.100.063828. URL: https://link.aps.org/doi/10.1103/PhysRevA.100.063828.

[17] M. W. Holtfrerich and A. M. Marino. “Control of the size of the coherence area in entangled twin beams”. In: *Phys. Rev. A* **93** (6 June 2016), p. 063821. DOI:

10.1103/PhysRevA.93.063821. URL: https://link.aps.org/doi/10.1103/PhysRevA.93.063821.

[18] Michael A. Taylor et al. "Biological measurement beyond the quantum limit". In: *Nature Photonics* **7**.3 (Feb. 2013), pp. 229–233. ISSN: 1749-4893. DOI: 10.1038/nphoton.2012.346. URL: http://dx.doi.org/10.1038/nphoton.2012.346.

[19] Ben Lawrie, Raphael Pooser, and Petro Maksymovych. "Squeezing Noise in Microscopy with Quantum Light". In: *Trends in Chemistry* **2**.8 (2020), pp. 683–686. ISSN: 2589-5974. DOI: https://doi.org/10.1016/j.trechm.2020.06.003. URL: http://www.sciencedirect.com/science/article/pii/S2589597420301507.

[20] C. S. Embrey et al. "Observation of Localized Multi-Spatial-Mode Quadrature Squeezing". In: *Physical Review X* **5**.3, 031004 (July 2015), p. 031004. DOI: 10.1103/PhysRevX.5.031004. arXiv: 1409.6561 [quant-ph].

[21] M. Fox. *Quantum Optics: An Introduction*. Oxford Master Series in Physics. OUP Oxford, 2006. ISBN: 9780198566731. URL: https://books.google.co.uk/books?id=2_ZP-LDF9jkC.

[22] James Clerk Maxwell. "VIII. A dynamical theory of the electromagnetic field". In: *Philosophical Transactions of the Royal Society of London* **155** (1865), pp. 459–512. DOI: 10.1098/rstl.1865.0008. eprint: https://royalsocietypublishing.org/doi/pdf/10.1098/rstl.1865.0008. URL: https://royalsocietypublishing.org/doi/abs/10.1098/rstl.1865.0008.

[23] Grant R Fowles. *Analytical Mechanics*. en. 3rd ed. London, England: Thomson Learning, Jan. 1977.

[24] Ulf Leonhardt. *Measuring the Quantum State of Light*. Cambridge University Press, 2005.

[25] David J. Griffiths. *Introduction to Quantum Mechanics (2nd ed.)* Prentice Hall, 2004.

[26] Leonard Susskind and Art Friedman. *Quantum mechanics: The theoretical minimum*. New Delhi, India: Allen Lane, Feb. 2014.

[27] H. P. Robertson. "The Uncertainty Principle". In: *Phys. Rev.* **34**.1 (1929), pp. 163–64.

[28] Roy J. Glauber. "Coherent and Incoherent States of the Radiation Field". In: *Phys. Rev.* **131** (6 Sept. 1963), pp. 2766–2788. DOI: 10.1103/PhysRev.131.2766. URL: https://link.aps.org/doi/10.1103/PhysRev.131.2766.

[29] S. M. Roy and Virendra Singh. "Generalized coherent states and the uncertainty principle". In: *Phys. Rev. D* **25** (12 June 1982), pp. 3413–3416. DOI: 10.1103/PhysRevD.25.3413. URL: https://link.aps.org/doi/10.1103/PhysRevD.25.3413.

[30] Robert Boyd. *Nonlinear Optics (3rd ed.)* Academic Press, 2008.

[31] C. Gerry and P. Knight. *Introductory Quantum Optics*. Cambridge University Press, 2004. ISBN: 9781139453554. URL: https://books.google.co.uk/books?id=MDwgAwAAQBAJ.

[32] Raul Carranza and Christopher C. Gerry. "Photon-subtracted two-mode squeezed vacuum states and applications to quantum optical interferometry". In: *J. Opt. Soc. Am. B* **29**.9 (Sept. 2012), pp. 2581–2587. DOI: 10.1364/JOSAB.29.002581. URL: https://opg.optica.org/josab/abstract.cfm?URI=josab-29-9-2581.

[33] Quentin Glorieux et al. "Hot atomic vapors for nonlinear and quantum optics". In: *New Journal of Physics* **25**.5 (May 2023), p. 051201. ISSN: 1367-2630. DOI: 10.1088/1367-2630/acce5a. URL: http://dx.doi.org/10.1088/1367-2630/acce5a.

[34] David Jeffrey Griffiths. *Introduction to electrodynamics 3/e*. en. 2006.

[35] Sybil P Parker, ed. *McGraw-hill encyclopedia of physics*. en. 2nd ed. New York, NY: McGraw-Hill, Mar. 1993.

[36] R.B. Feynman R.P.; Leighton and M. Sands. *Feynman Lectures on Physics: Volume 2, Addison-Wesley*. 1964.

[37] David Cotter Paul N. Butcher. *The Elements of Nonlinear Optics*.

[38] Nicolaas Bloembergen, ed. *Nonlinear Optics (4th Edition)*. 4th ed. Singapore, Singapore: World Scientific Publishing, Jan. 1996.

[39] M. Bass et al. "Optical Rectification". In: *Phys. Rev. Lett.* **9** (11 Dec. 1962), pp. 446–448. DOI: 10.1103/PhysRevLett.9.446. URL: https://link.aps.org/doi/10.1103/PhysRevLett.9.446.

[40] Quentin Glorieux et al. "Hot atomic vapors for nonlinear and quantum optics". In: *New Journal of Physics* 25.5 (May 2023), p. 051201. ISSN: 1367-2630. DOI: 10.1088/1367-2630/acce5a. URL: http://dx.doi.org/10.1088/1367-2630/acce5a.

[41] Richard Tilley. *Crystals and Crystal Structures*. en. Hoboken, NJ: Wiley-Blackwell, June 2006.

[42] H. Weyl. *The Classical Groups*. Princeton University Press, 1939.

[43] M. T. Turnbull et al. "Role of the phase-matching condition in nondegenerate four-wave mixing in hot vapors for the generation of squeezed states of light". In: **88**.3, 033845 (Sept. 2013), p. 033845. DOI: 10.1103/PhysRevA.88.033845. arXiv: 1303.7187 [quant-ph].

[44] L. HOLLBERG A. S. ZIBROV A. B. MATSKO and V. L. VELICHAN. "Resonant enhancement of refractive index in a cascade scheme". In: *Journal of Modern Optics* **49**.3/4 (2002), pp. 359–365.

[45] M. T. Turnbull et al. "Role of the phase-matching condition in nondegenerate four-wave mixing in hot vapors for the generation of squeezed states of light". In: *Physical Review A* **88**.3 (Sept. 2013). ISSN: 1094-1622. DOI: 10.1103/physreva.88.033845. URL: http://dx.doi.org/10.1103/PhysRevA.88.033845.

[46] G. M. D'Ariano, M. G. A. Paris, and M. F. Sacchi. "On the parametric approximation in quantum optics". In: *Nuovo Cimento B Serie* **114**.3 (Mar. 1999), p. 339. arXiv: quant-ph/9902013 [quant-ph].

[47] Albert Messiah. *Modern Quantum Mechanics*. Addison-Wesley, 1994.

[48] B. J. Lawrie and R. C. Pooser. "Toward real-time quantum imaging with a single pixel camera". In: *Opt. Express* **21**.6 (Mar. 2013), pp. 7549–7559. DOI: 10.1364/OE.21.007549. URL: https://opg.optica.org/oe/abstract.cfm?URI=oe-21-6-7549.

[49] M. Lassen et al. "Tools for Multimode Quantum Information: Modulation, Detection, and Spatial Quantum Correlations". In: *Phys. Rev. Lett.* **98** (8 Feb. 2007), p. 083602. DOI: 10.1103/PhysRevLett.98.083602. URL: https://link.aps.org/doi/10.1103/PhysRevLett.98.083602.

[50] Jeremy B. Clark et al. "Imaging using quantum noise properties of light". In: *Opt. Express* **20**.15 (July 2012), pp. 17050–17058. DOI: 10.1364/OE.20.017050. URL: https://opg.optica.org/oe/abstract.cfm?URI=oe-20-15-17050.

[51] A. Meda et al. "Absolute calibration of a charge-coupled device camera with twin beams". In: *Applied Physics Letters* **105**.10 (2014), p. 101113. DOI: 10.1063/1.4895665. eprint: https://doi.org/10.1063/1.4895665. URL: https://doi.org/10.1063/1.4895665.

[52] B.J. Lawrie, N. Otterstrom, and R.C. Pooser. "Coherence area profiling in multi-spatial-mode squeezed states". In: *Journal of Modern Optics* **63**.10 (2016), pp. 989–

994. DOI: 10.1080/09500340.2015.1080869. eprint: https://doi.org/10.1080/09500340.2015.1080869. URL: https://doi.org/10.1080/09500340.2015.1080869.

[53] P.R. Hemmer M.S. Shahriar. "Generation of squeezed states and twin beams via non-degenerate four-wave mixing in a system". In: *Optics Communications* **158** (1998), pp. 273–286.

[54] A. G. Fox and Tingye Li. "Resonant modes in a maser interferometer". In: *The Bell System Technical Journal* **40**.2 (1961), pp. 453–488. DOI: 10.1002/j.1538-7305.1961.tb01625.x.

[55] A. Fox and Tingye Li. "Computation of optical resonator modes by the method of resonance excitation". In: *IEEE Journal of Quantum Electronics* **4**.7 (1968), pp. 460–465. DOI: 10.1109/JQE.1968.1075368.

[56] L. Lopez et al. "Multimode squeezing properties of a confocal optical parametric oscillator: Beyond the thin-crystal approximation". In: *Physical Review A* **72**.1 (July 2005). DOI: 10.1103/physreva.72.013806. URL: https://doi.org/10.1103%2Fphysreva.72.013806.

[57] M. Martinelli et al. "Experimental study of the spatial distribution of quantum correlations in a confocal optical parametric oscillator". In: *Physical Review A* **67**.2 (Feb. 2003). DOI: 10.1103/physreva.67.023808. URL: https://doi.org/10.1103%2Fphysreva.67.023808.

[58] O. Jedrkiewicz et al. "Detection of Sub-Shot-Noise Spatial Correlation in High-Gain Parametric Down Conversion". In: *Physical Review Letters* **93**.24 (Dec. 2004). DOI: 10.1103/PhysRevLett.93.243601. arXiv: quant-ph/0407211 [quant-ph].

[59] A.E. Siegman. *Lasers*. G - Reference,Information and Interdisciplinary Subjects Series. University Science Books, 1986. ISBN: 9780935702118. URL: https://books.google.co.uk/books?id=1BZVwUZLTkAC.

[60] Benjamin J. Lawrie et al. "Quantum Sensing with Squeezed Light". In: *ACS Photonics* **6**.6 (May 2019). ISSN: 2330-4022. DOI: 10.1021/acsphotonics.9b00250. URL: https://www.osti.gov/biblio/1557517.

[61] R. C. Pooser et al. "Truncated Nonlinear Interferometry for Quantum-Enhanced Atomic Force Microscopy". In: *Phys. Rev. Lett.* **124** (23 June 2020), p. 230504. DOI: 10.1103/PhysRevLett.124.230504. URL: https://link.aps.org/doi/10.1103/PhysRevLett.124.230504.

[62] Xinrui Wei et al. "Twin-beam-enhanced displacement measurement of a membrane in a cavity". In: *Applied Physics Letters* **115**.25 (Dec. 2019), p. 251105. DOI: 10.1063/1.5129547. URL: https://doi.org/10.1063%2F1.5129547.

[63] P. F. Moulton. "Spectroscopic and laser characteristics of Ti:Al2O3". In: *J. Opt. Soc. Am. B* **3**.1 (Jan. 1986), pp. 125–133. DOI: 10.1364/JOSAB.3.000125. URL: https://opg.optica.org/josab/abstract.cfm?URI=josab-3-1-125.

[64] T. R. Steele et al. "Broadly tunable high-power operation of an all-solid-state titanium-doped sapphire laser system". In: *Opt. Lett.* **16**.6 (Mar. 1991), pp. 399–401. DOI: 10.1364/OL.16.000399. URL: https://opg.optica.org/ol/abstract.cfm?URI=ol-16-6-399.

[65] *SolsTiS: ULTRA NARROW LINEWIDTH CW TI: SAPPHIRE LASER - Datasheet*. M Squared.

[66] M. Jasperse, L. D. Turner, and R. E. Scholten. "Relative intensity squeezing by four-wave mixing with loss: an analytic model and experimental diagnostic". In: *Optics Express* **19**.4 (Feb. 2011), p. 3765. DOI: 10.1364/oe.19.003765. URL: https://doi.org/10.1364%2Foe.19.003765.

[67] Jason D. Mueller, Nigam Samantaray, and Jonathan C. F. Matthews. "A practical model of twin-beam experiments for sub-shot-noise absorption measurements". In:

Applied Physics Letters **117**.3 (July 2020), p. 034001. DOI: 10.1063/5.0015576. URL: https://doi.org/10.1063%2F5.0015576.

[68] Jr. Eddie H. Young and Shi-Kay Yao. "Design considerations for acousto-optic devices". In: *Proceedings of the IEEE* **69**.1 (1981), pp. 54–64. DOI: 10.1109/PROC.1981.11920.

[69] Jose Carlos Pedro et al. *The Cambridge RF and microwave engineering series: Nonlinear circuit simulation and modeling: Fundamentals for microwave design*. Cambridge, England: Cambridge University Press, June 2018.

[70] A. Carter and B. Samson. "Panda-style fibers move beyond telecom". In: **40** (Aug. 2004), S11–S14.

[71] Paul E Gray and Campbell L Searle. *Electronic principles*. Books S. Brisbane, QLD, Australia: John Wiley and Sons (WIE), Jan. 1970.

[72] Sh Kogan. "Generation–recombination noise". In: *Electronic Noise and Fluctuations in Solids*. Cambridge: Cambridge University Press, Aug. 1996, pp. 118–129.

[73] Michael Peter Norton and Denis G Karczub. *Fundamentals of noise and vibration analysis for engineers*. en. 2003.

[74] Allen B Downey. *Think complexity*. en. Sebastopol, CA: O'Reilly Media, Mar. 2012.

[75] "Damage". In: *Scientific Charge-Coupled Devices*. 1000 20th Street, Bellingham, WA 98227-0010 USA: SPIE, 2009, pp. 721–845.

[76] Princeton Instruments. *IS-1024BR eXcelon specifications*. URL: http://c1170156.r56.cf3.rackcdn.com/UK_PRN_1024B-PIXISSeriesCCDCamera_DS.pdf.

[77] F.A. Haight. *Handbook of the Poisson Distribution*. Operations Research Society of America. Publications in operations research. Wiley, 1967. ISBN: 9788391014424. URL: https://books.google.co.uk/books?id=l8Y-AAAAIAAJ.

[78] John A Rice. *Mathematical statistics and data analysis*. en. Florence, KY: Brooks/Cole, 2007.

[79] A. de Moivre. *The Doctrine of Chances: Or, A Method of Calculating the Probability of Events in Play*. Eighteenth century collections online. W. Pearson, 1718. ISBN: 9780598843753. URL: https://books.google.co.uk/books?id=3EPac6QpbuMC.

[80] Norman L Johnson, Adrienne W Kemp, and Samuel Kotz. *Univariate Discrete Distributions*. en. 3rd ed. Wiley Series in Probability and Statistics. Chichester, England: Wiley-Blackwell, Aug. 2005.

[81] Roy Yates and David J Goodman. *Probability and stochastic processes*. en. 2nd ed. Nashville, TN: John Wiley & Sons, June 2004.

[82] Sangtae Ahn and Jeffrey A Fessler. "Standard errors of mean, variance, and standard deviation estimators". In: *EECS Department, The University of Michigan* 1.2 (2003).

[83] Steven W Smith. *The scientist and engineer's guide to digital signal processing*. California Technical Pub, Dec. 1997.

[84] Leo A Goodman. "On the Exact Variance of Products". In: *Journal of the American Statistical Association* **55**.292 (1960), pp. 708–713.

[85] R. Paschotta. *Intensity Noise*. RP Photonics Encyclopedia. Nov. 2006. DOI: 10.61835/lkh. URL: https://www.rp-photonics.com/intensity_noise.html (visited on 12/12/2023).

[86] R. Paschotta. *Noise Eaters*. RP Photonics Encyclopedia. June 2005. DOI: 10.61835/mgh. URL: https://www.rp-photonics.com/noise_eaters.html (visited on 12/12/2023).

[87] R. Paschotta. *Stabilization of Lasers*. RP Photonics Encyclopedia. Aug. 2007. DOI: 10.61835/fkd. URL: https://www.rp-photonics.com/stabilization_of_lasers.html (visited on 12/12/2023).

[88] Lincoln D. Turner et al. "Frequency noise characterisation of narrow linewidth diode lasers". In: *Optics Communications* **201** (2002), pp. 391–397.

[89] Matthew S. Taubman et al. "Intensity feedback effects on quantum-limited noise". In: *J. Opt. Soc. Am. B* **12**.10 (Oct. 1995), pp. 1792–1800. DOI: 10.1364/JOSAB.12.001792. URL: http://www.osapublishing.org/josab/abstract.cfm?URI=josab-12-10-1792.

[90] D. J. McCarron. 2007. URL: https://jila1.nickersonm.com/papers/A%20Guide%20to%20Acousto-Optic%20Modulators.pdf.

[91] John Sparkes. *Semiconductor Devices*. CRC Press., 1994.

[92] *PIN Diode Fundamentals*. Microsemi Corp. 2022. URL: https://www.microsemi.com/sites/default/files/micnotes/701.pdf.

[93] Jerald Graeme. *Photodiode Amplifiers: OP Amp Solutions*. McGraw-Hill, 1995.

[94] *Si PIN photodiodes*. Hamamatsu. URL: https://www.hamamatsu.com/content/dam/hamamatsu-photonics/sites/documents/99_SALES_LIBRARY/ssd/s1223_series_kpin1050e.pdf.

[95] *PDA100A(-EC) Si Switchable Gain Detector User Guide*. Thorlabs. URL: https://www.thorlabs.de/drawings/53713e0692cd700e-E520D81E-FC6B-23EE-98B30C1AADF214FE/PDA100A-Manual.pdf.

[96] *HIGH-VOLTAGE, HIGH SLEW RATE, WIDEBAND FET-INPUT OPERATIONAL AMPLIFIER*. THS4631. Texas Instruments. 2011.

[97] *Op Amp Circuit Collection, National Semiconductor Application Note AN-31, reproduced in National Semiconductor Applications Handbook*. 1994.

[98] R. Nelson and L. Davidson. "Electrical noise generated from the microphonic effect in capacitors". In: *2002 IEEE International Symposium on Electromagnetic Compatibility*. Vol. **2**. 2002, 855–860 vol.2. DOI: 10.1109/ISEMC.2002.1032708.

[99] *BC546 / BC547 / BC548 / BC549 / BC550 NPN Epitaxial Silicon Transistor*. Fairchild. 2014. URL: https://www.mouser.com/datasheet/2/149/BC547-190204.pdf.

[100] *PNP Epitaxial Silicon Transistor BC556, BC557, BC558, BC559, BC560*. Onsemi. URL: https://www.mouser.co.uk/datasheet/2/308/BC556BTA_D-2310029.pdf.

[101] Kiam Heong Ang, G. Chong, and Yun Li. "PID control system analysis, design, and technology". In: *IEEE Transactions on Control Systems Technology* **13**.4 (2005), pp. 559–576. DOI: 10.1109/TCST.2005.847331.

[102] V. Boyer et al. "Ultraslow Propagation of Matched Pulses by Four-Wave Mixing in an Atomic Vapor". In: *Phys. Rev. Lett.* **99** (14 Oct. 2007), p. 143601. DOI: 10.1103/PhysRevLett.99.143601. URL: https://link.aps.org/doi/10.1103/PhysRevLett.99.143601.

[103] Ying S. Hu et al. "Single-Molecule Super-Resolution Light-Sheet Microscopy". In: *ChemPhysChem* **15**.4 (2014), pp. 577–586. DOI: https://doi.org/10.1002/cphc.201300732. eprint: https://chemistry-europe.onlinelibrary.wiley.com/doi/pdf/10.1002/cphc.201300732. URL: https://chemistry-europe.onlinelibrary.wiley.com/doi/abs/10.1002/cphc.201300732.

[104] Joshua Hordell et al. "Transport of spatial squeezing through an optical waveguide". In: *Opt. Express* 26.**18** (Sept. 2018), pp. 22783–22792. DOI: 10.1364/OE.26.022783. URL: https://opg.optica.org/oe/abstract.cfm?URI=oe-26-18-22783.

[105] Raphael C. Pooser et al. “Squeezed light and entangled images from four-wave-mixing in hot rubidium vapor”. In: *Quantum Communications and Quantum Imaging VI*. Ed. by Ronald E. Meyers, Yanhua Shih, and Keith S. Deacon. SPIE, Aug. 2008. DOI: 10.1117/12.795474. URL: https://doi.org/10.1117%2F12.795474.

[106] Alberto M. Marino et al. “Entangled Images from 4-Wave Mixing in Rubidium Vapor”. In: *Conference on Lasers and Electro-Optics/Quantum Electronics and Laser Science Conference and Photonic Applications Systems Technologies*. Optica Publishing Group, 2008, QFB3. URL: https://opg.optica.org/abstract.cfm?URI=QELS-2008-QFB3.

[107] *Applying acceleration and deceleration profiles to bipolar stepper motors*. By Jose I. Quinones. Texas Instruments Incorporated. URL: https://www.ti.com/lit/an/slyt482/slyt482.pdf.